# NUMERICAL STUDIES OF BLACK HOLE INITIAL DATA

BY

MICHAEL KOPPITZ

THESIS

Submitted in partial fullfilment of the requirements
for the degree of Doctor of Philosophy in Astrophysics
in the Graduate College of the
University of Potsdam, 2004

Albert Einstein Institute in Golm

NUMERICAL STUDIES OF BLACK HOLE INITIAL DATA

Michael Koppitz, Ph.D.
Department of Astrophysics
University of Potsdam, 2004
Dr. H. Edward Seidel

This thesis presents new approaches to evolutions of binary black hole systems in numerical relativity. We analyze and compare evolutions from various physically motivated initial data sets, in particular presenting the first evolutions of Thin Sandwich data generated by the Meudon group.

For the first time two different quasi-circular orbit initial data sequences are compared through fully 3d numerical evolutions: (Brandt-Brügmann) Puncture data, which are currently the most commonly used binary black hole initial data, and Thin Sandwich data (TSD) based on a helical killing vector ansatz, that are thought to be very close to Post-Newtonian results. The two different sets are compared in terms of the physical quantities that can be measured from the numerical data, and in terms of their evolutionary behavior.

The evolutions demonstrate that for the latter, "Meudon", datasets, the black holes do in fact orbit for a longer amount of time before they merge, in comparison with Puncture data from the same separation. This indicates they are potentially better estimates of quasi-circular orbit parameters. The merger times resulting from the numerical simulations are consistent with independent Post-Newtonian estimates that the final plunge phase of a black hole inspiral should take 60% of an orbit. Accuracy in individual horizon masses could typically be kept to within 2% over the course of an evolution.

Stable evolutions demanded appropriate gauges on the initial data surface. Numerical tests of several options demonstrate that for these systems a gauge involving the Meudon lapse and shift outside of the horizons was optimal, though modifications were required within the horizon. The initial Meudon gauges were found to induce a

dynamical transient phase in the early evolution when coupled to our usual "1+log" and "Γ-driver" gauge conditions. After this phase, however, the system settles down and continues with fewer dynamics in the evolution variables. These simulations were supported by new techniques developed and used successfully during the long-term evolutions. A co-rotating coordinate system, implemented via gauge conditions, helped to keep evolutions more stable. A newly developed distance measurement along space-like geodesics was used to analyze the data, indicating a better preserved circularity for the Thin Sandwich data.

Additionally a new type of Kerr-Schild-based initial data (non-conformal data) is introduced and implemented. In contrast to the previously mentioned methods, it does not rely on a conformal flatness ansatz or nontrivial multiple-sheet topology, thus potentially being astrophysically more realistic.

# Acknowledgments

First I would like to thank my supervisor Ed Seidel who introduced me into numerical relativity, into the AEI and the group. He always gave advice and new perspectives and last but not least he made all the necessary organizational commitments to make this work possible.

Thanks to Denis Pollney for guiding me through the hardest part of this thesis. He helped planning it, suggested numerical and physical tests, proof-read it, and kept up the motivation.

This work is a group work. Without the many discussions about physics, numerics, programming and computer problems with Miguel Alcubierre, Florian Beyer, Bernd Brügmann, Peter Diener, Nils Dorband, Francisco Guzman, Ian Hawke, Frank Herrmann, Frank Löffler, Thomas Radke, Erik Schnetter, and Jonathan Thornburg it would not exist. Thanks to all of them.

I would also like to thank Eric Gourgoulhon who helped me getting started with the Meudon data and always answered questions concerning them and Phillippe Grandclément for giving the additional Meudon data sets to me.

Nigel Bishop kept pushing me towards finishing the work on the nonconformal data, often came up with new ideas and plans, and helped solving problems. Thank you for that.

I thank Bernard Schutz, the managing director of the AEI, for all the organization and guidance.

Thank you Kathrin, Tom, Lina, and Max for loving me through all that!.

This work was supported by the Max-Planck-Institute for Gravitational Physics, Albert Einstein Institute.

Calculations were performed using *CACTUS* code [18, 17, 14, 16, 15], at the Albert Einstein Institute (AEI) Origin 2000, the AEI Linux cluster Peyote, the UNM IBM Netfinity 4500R Linux Cluster Los Lobos, the National Center for Supercomputer Application (NCSA) Origin 2000, the Pittsburgh Supercomputing Center (PSC) TCS1, the RZG IBM pSeries 690 cluster Regatta, the LSU Capital Center Intel P4 Xeon cluster Supermike, the PSC Compaq Alphaserver ES45 cluster Lemieux, and the NCSA IA-32 Linux Cluster Platinum.

to Max, Lina,
Tom, and Kathrin

# Contents

**1 Introduction and Motivation . . . . . 1**

1.1 Notation and Units . . . . . 6

**2 The 3+1 split . . . . . 8**

2.1 Introduction . . . . . 8

2.2 The 3+1 Split . . . . . 9

2.3 Formulations . . . . . 12

2.3.1 ADM . . . . . 12

2.3.2 The BSSN Formulation . . . . . 13

2.4 Coordinate Conditions . . . . . 17

2.4.1 The Lapse Function . . . . . 20

2.4.2 Shift conditions . . . . . 22

2.4.3 Co-rotation . . . . . 24

**3 The Initial Data Problem . . . . . 27**

3.1 Introduction . . . . . 27

3.2 Solving the Constraints (I):

The York Procedure . . . . . 29

3.2.1 Binary black holes . . . . . 31

3.2.2 Treating the Extrinsic Curvature . . . . . 35

3.2.3 Puncture Data . . . . . 38

3.2.4 Problems with These Data . . . 39
3.3 Solving the Constraints (II): Thin Sandwich . . . 41
3.4 Other construction methods . . . 43
3.4.1 Superposed Kerr Schild data . . . 43
3.4.2 Post-Newtonian based data . . . 45
3.5 Nonconformal Data . . . 45
3.6 Summary . . . 52

**4 Methodology . . . 55**
4.1 Finite Differencing . . . 55
4.2 Numerical Error Estimates . . . 56
4.2.1 Convergence . . . 56
4.2.2 Constraints . . . 58
4.3 Elliptic Solvers . . . 59
4.4 Boundary Conditions . . . 60
4.4.1 Outer Boundary Condition . . . 60
4.4.2 Inner Boundary Condition . . . 61
4.5 Measurement of Physical Quantities . . . 62
4.5.1 Masses and Momenta . . . 63
4.5.2 Horizons . . . 66
4.5.3 Horizon Distances . . . 69
4.6 Summary . . . 73

**5 Evolutions of Puncture data . . . 74**
5.1 Introduction . . . 74
5.2 The Cook Sequence . . . 74
5.3 Merger Times . . . 76

**6 Evolutions of**

**"Thin Sandwich" Data . . . . . 81**

6.1 Introduction . . . . . 81

6.2 Meudon Data Construction . . . . . 81

6.2.1 The Field Equations . . . . . 81

6.2.2 Boundary Conditions . . . . . 84

6.2.3 Circular Orbits . . . . . 88

6.3 Interpolation of Initial Data . . . . . 90

6.4 Results . . . . . 94

6.4.1 Initial Data . . . . . 94

6.4.2 Evolution . . . . . 102

6.4.3 Gauge Experiments . . . . . 105

6.4.4 Long Term Evolutions of M12 . . . . . 108

6.4.5 Comparison of Different Meudon data sets . . . . . 118

6.4.6 Comparison of Meudon Data and Puncture data . . . . . 121

6.5 Summary . . . . . 127

**7 Conclusions . . . . . 130**

7.1 Summary . . . . . 130

7.2 Outlook . . . . . 132

7.2.1 Mesh Refinement . . . . . 133

7.2.2 Gauge Parameters . . . . . 134

7.2.3 Drift-correction . . . . . 135

7.2.4 Formulations . . . . . 137

7.2.5 Excision . . . . . 138

7.2.6 Boundaries . . . . . 139

**A Cauchy Split . . . . . 140**

**B Bianchi Identities** ..... **142**

**C Lie Derivatives** ..... **144**

**Bibliography** ..... **146**

# Chapter 1

# Introduction and Motivation

Einstein's Theory of General Relativity still is the one theory that describes gravity best. It solved many problems physics had, suggested new questions which it solved as well, and it proposed new effects many of which were experimentally confirmed. It completely changed the way nature is perceived.

However, some problems are still unsolved, among them the two body problem. There are several approximations that work to high accuracy in many cases. Most of the standard experiments to verify General Relativity Theory for instance are compared with the test particle approximation. In this approximation the mass ratio of the two bodies is taken to be extreme. So the influence of one of the bodies at the other one can be neglected. However, the real solution, a four dimensional metric that solves Einstein's equations, is not known in general.

A very successful approximation method is the "close limit" (CL) approach [100], which is used when the two bodies have merged or are about to merge, so that they are located in the same gravitational well, and can be treated as one deformed object. Perturbation theory is a very powerful tool in this situation. The background space-time is chosen as an analytically known solution (as for example the Schwarzschild or the Kerr solution, representing a single black hole), that has an additional small distortion. The equations can be expanded as a series that can be cut off at some order because of the smallness of the distortion. Many results have been achieved

using this approximation. Price and Pullin applied this method to two black holes that are already surrounded by a common horizon and computed the emitted gravitational waves[100]. An especially successful ansatz was used by the *Lazarus Project* [28, 30, 31, 27]. Here numerical results are taken when the fully relativistic code breaks down (or shortly before) and translated into the language of the close limit approximation, where it can be evolved further using the appropriate equations and the relevant physical quantities (especially waveforms) can be extracted.

Another ansatz uses the so-called Post Newtonian approximation (PN) [39, 38, 62], a method that expands Einstein's equations into a series of $1/c^2$ which equals Newton's theory at zero order and the full General Relativity Theory in the infinite limit[1]. A number of successes has been achieved using this approximation, for instance the slow and adiabatic inspiral of two bodies well separated from each other could be modeled quite accurately. However, when the black holes get closer and the mutual influence grows, the Post-Newtonian ansatz breaks down.

Together Post-Newtonian methods [39, 38, 62] and the close limit approximation in form of the *Lazarus Project* [28, 30] can deal with a great part of a two body system. The inspiral part that starts at great distances is covered by the Post-Newtonian method, and the final distorted Kerr-black hole can be treated with the close limit methods. Only the part in between, where the most violent, most dynamic changes of the metric and all other variables take place, must be treated fully relativistically. During this phase the objects are still well separated and cannot be treated as one but they are so close that the errors made even with a high order Post-Newtonian ansatz is very large.

Especially in the advent of gravitational wave astronomy it becomes more important also from a practical point of view to get a solution of the two body problem. Massive objects orbiting about each other are expected to emit gravitational waves - another

[1]this latter statement is actually not proven yet and by many believed to be not true

prediction of General Relativity Theory that is not proven yet. These waves can be measured on earth using modern detectors that have just finished their first data collection runs.

Gravitational waves will be emitted from all massive accelerated bodies, not only from those that send electromagnetic radiation as well. These waves cannot be shielded from us by any matter in the line of sight. This could allow the exploration of regions of the universe which are obscured to conventional telescopes, such as centers of galaxies. So there is reason to expect the detection of sources not seen until now, as for instance dark matter, small (earthlike) planets and black holes. But since the gravitational radiation reaching earth will be extremely weak (amplitudes of only $10^{-21}$ are expected even for the strongest events), it will be quite difficult to detect them. Of extreme importance here is the knowledge of the expected waveforms. When the main features of the waves such as amplitude, frequency, falloff, etc. are known, the technique of matched filtering can be used to find the signal in the vast noise, greatly improving the possibility of detecting it.

The strongest gravitationally radiating systems are collisions of black holes. A number of recent astronomical observations give strong evidence for black holes in the centers of galaxies (see for example [75] and references therein). However these observations are all only indirect- the detected radiation always stems from matter falling into the object or orbiting it. Gravitational wave detection would for the first time directly see black holes. Numerical simulations of globular clusters [126, 127] suggest that binary black hole mergers could happen that often that they might be detected via gravitational waves at estimated rates of $1.6 \times 10^{-7}\ \mathrm{yr}^{-1}\,\mathrm{Mpc}^{-3}$, which results in about one detected event every two years for the Laser Interferometer Gravitational Wave Observatory (LIGO)[116] and in one event per day for the already planned and improved device Advanced LIGO[113]. More recent estimates based on the latest observations and numerical experiments have more or less confirmed this

optimistic result some even estimate event-rates of app. 850 $\mathrm{yr}^{-1}$ for Advanced LIGO and approximately 0.25 $\mathrm{yr}^{-1}$ for LIGO [116].

Once gravitational wave astronomy is established, a large number of physical details can be expected. Apart from detecting new sources or directly detecting expected ones, there is for example the possibility of direct determination of the physical parameters of some objects. As Schutz pointed out [103] it is possible from the frequency and the fall-off of the periodic part of the wave (stemming from the inspiral phase) to detect the distance to the object quite accurately. This could be used as standard candles, much more precise than the ones used today. Another quite important feature of gravitational waves is that the early universe was transparent for them from the first $10^{-43}$ seconds on (the Planck time). All other radiation stems from a much later time. This permits a look into the very early universe.

So it is of crucial importance, for both theoretical and practical purposes, to find a solution, to the two body problem of General Relativity Theory.

However, Einstein's equations are extremely complicated, highly nonlinear coupled differential equations. Solving them analytically is a task that has been successfully completed only for some special systems. A general solution of the two body problem has eluded mathematicians. Numerical simulations, however, provide another possibility for solving Einstein's equations. As will be explained in detail the usual method is to treat them as an initial boundary values problem, splitting the equations into a set of equations describing the initial data (thereby setting up all physical properties of the system) and into a set of equations that evolves these data through time. The question of how to choose physically realistic solutions to the initial data equations is still an active subject of research.

This thesis will deal with that problem, the construction, testing, and comparing of initial data aiming at more realistic data.

It will start with a short introduction into the so-called 3+1 split, an essential part

of the numerical treatment of General Relativity Theory. Four-dimensional spacetime is split into a set of 3 dimensional subspaces and time. This separates Einstein's equations into a set of equations prescribing initial data and a set of evolution equations. The introduction will include two formulations of the evolution equations, the original one and the one used for the evolutions in this thesis, it will show possible choices for the gauges especially emphasizing the new drift-correct method that helps to keep black hole horizons in place and thus to stabilize numerical evolutions.

Chapter 3 will deal with various methods to solve the initial value problem especially touching on the binary black holes. The description will start with the most commonly used split of the initial data equations into parts that are freely specifiable and parts that have to be solved for, the York decomposition. It will include initial data describing black holes about to collide head-on (Misner data) and more general data that include (or at least can include) linear or angular momentum (Puncture data and Thin Sandwich data). Both of these types of initial data will be used later in evolutions. The chapter will describe the problems all these data sets have and introduce some ways to solve them.

Additionally, put in a separate section because it is original work, this chapter will present a new way of constructing initial data. This new construction does not rely on the York decomposition and is therefore completely different from usually used initial data.

As a short interlude, Chapter 4 will introduce the main numerical and technical methods used for this paper. It will touch on methods to solve elliptic equations and describe excision. Additionally it will introduce the physical quantities used in later chapters.

Chapter 5 will introduce an evolutionary sequence of puncture initial data due to Cook [57]. It will show new results evolving these data and especially deal with the time it takes to reach a merged black hole.

In chapter 6 a version of Thin Sandwich data is introduced that uses the so-called "helical killing vector" approach (Meudon data). For the first time evolutions of this kind of Thin Sandwich data that could be lead to a black hole merger will be presented. These data represent a physical system far more realistic than earlier initial data sets. Their construction gives some inside into the physics used and their physical properties are very close to Post-Newtonian approximations and therefore more physically tangible than other data sets. The evolutions of these data also show that they behave more realistic. This chapter presents the properties of this initial data, results of evolutions starting with them, differences between several data sets, and differences between Meudon data and Puncture data.

Finally, in chapter 7 the results of the thesis are summarized and improvements suggested. An outlook is given on what could and should be done next to step further in the way of solving the binary black hole problem.

All longer mathematical reasoning is collected in the appendices, which part into one describing the 3+1 split in more mathematical detail, one that deals with the Bianchi identities and a last one that explains the Lie derivative, which is used throughout the paper.

## 1.1 Notation and Units

It is very common in the numerical community to set the speed of light as well as the gravitational constant equal to unity. This makes units like length and time being of unit Mass. When dealing with black holes it is also useful to normalize these units to the mass of the black hole (or the total mass of the system if several black holes are involved). So when dealing with a regular black hole of approximately 20 solar masses a unit of 1M will be a length of about 30 km or a time of app. 100 $\mu$s.

Since the work is dealing solely with black holes all matter terms will be neglected thereby simplifying the equations significantly.

The entire paper is using the notation of MTW [91]. That is: Latin indices will denote purely spatial objects and will run from one to three while Greek indices will run from zero to three and thus denote full four-dimensional objects, the metric has signature $(-+++)$, the curvature tensor is defined as:

$$R^{\alpha}{}_{\beta\gamma\delta} \equiv \Gamma^{\alpha}{}_{\beta\delta} - \Gamma^{\alpha}{}_{\beta\gamma} + \Gamma^{\alpha}{}_{\lambda\gamma}\Gamma^{\lambda}{}_{\beta\delta} - \Gamma^{\alpha}{}_{\lambda\delta}\Gamma^{\lambda}{}_{\beta\gamma}, \tag{1.1}$$

the Ricci tensor and Ricci scalar are defined as:

$$R_{\mu\nu} = R^{\alpha}{}_{\mu\alpha\nu}, \tag{1.2}$$

$$R = g^{\mu\nu}R_{\mu\nu}, \tag{1.3}$$

respectively, and the Einstein tensor as:

$$G_{\mu\nu} \equiv R_{\mu\nu} - \frac{1}{2}g_{\mu\nu}R. \tag{1.4}$$

# Chapter 2

# The 3+1 split

## 2.1 Introduction

General Relativity Theory deals with spacetime as a whole. An analytic solution of Einstein's equations is a four dimensional hypersurface described by a metric, a tensor encoding the infinitesimal distance between two points. Unfortunately the equations are complicated enough that no such analytic solution of the two body problem has been found and it is unlikely that a general solution will be found by analytical means. Wheeler suggested the concept of geometrodynamics [120, 90]: through a split of the full four dimensional metric into a three dimensional space, plus time, the dynamics of the three dimensional geometry could be introduced. This split was prescribed for the first time by Arnowitt, Deser, and Misner (ADM) [25] attempting to quantize gravity. Though stemming from a different motivation, this formulation of Einstein's equations as an initial value problem suggested compelling methods for solving the equations. With the advent of computers in the 1960's and 70's, the idea of solving Einstein's equations numerically shaped. There have been many modifications to the formulations commonly used since then, but the main ideas of ADM still form the basis of standard approaches to numerical relativity. Alternatives such as null or 2+2 splits have also been studied, but in far less detail than the physically intuitive 3+1 split.

The Cauchy ansatz has limitations. Only spacetimes that are globally hyperbolic are constructible using a Cauchy development. That means in particular that nothing hidden behind a Cauchy horizon can be found with this technique. However, the "strong cosmic censorship conjecture" [96] suggests that all generic spacetimes are globally hyperbolic, i.e. do not posses Cauchy horizons. Therefore, assuming this conjecture to be true, all physically realistic solutions of Einstein's equations can be found using the Cauchy ansatz.

This chapter describes this ansatz. The following section introduces the actual split of the four dimensional spacetime into a set of three dimensional spaces and time. The succeeding section then will describe the equations that emerge when this split is used on Einstein's equations and a modification (called "BSSN") that improves their usability in numerical simulations. Additionally the idea of life gauges is introduced. These have proven essential for long term evolutions. Another section in this chapter will introduce the idea of drift-correction, a new method to keep apparent horizons in place and therefore evolutions more stable.

## 2.2 The 3+1 Split

There are several ways to decompose the geometry of spacetime. Up to now the most commonly used one is the so-called Cauchy approach, which sees spacetime as a sequence of three dimensional spaces ("instants of time"), which are evolved forward in time. It will be described in the this section.

This split is explained very detailed and mathematically thoroughly in York's treatise [125] (see also Cook's review [59] and references therein) so this will only be a brief introduction.

The four dimensional spacetime $(M, g_{\mu\nu})$ is foliated by 3-dimensional space-like hyperspaces $\Sigma$ labeled by a number $t$. On these hyperspaces a normal vector $n^\mu$ is introduced (usually chosen to be future pointing). This construction allows the

definition of a projection tensor $h_{\mu\nu}$ that has the expected properties:

$$\begin{aligned} h_{\mu\nu} &:= g_{\mu\nu} - n_\mu n_\nu \\ h_{\mu\nu} &= h_{\nu\mu} \\ h_{\mu\nu} n^\mu &= 0 \\ h_{\mu 0} &= 0. \end{aligned} \tag{2.1}$$

The last two relations indicate that $h_{\mu\nu}$ is purely spatial and projects all other geometrical objects down to the spacial hypersurface. With the help of this projection tensor it is very easy to go on with the split. The metric $g_{\mu\nu}$ will induce a metric $\gamma_{ab}$ on $\Sigma$ via:

$$\gamma_{ab} = h_a{}^\mu h_b{}^\nu g_{\mu\nu}. \tag{2.2}$$

This metric can be used to lower 3d indices of three dimensional objects in the usual way and its contravariant version $\gamma^{ab}$, defined through $\gamma^{ab}\gamma_{ac} = \delta^a_c$, is used to raise 3d indices. The time direction, $t^\mu = \frac{\partial}{\partial t}$, of the coordinate system can be split into a part laying in the surface and a part orthogonal to it:

$$\beta^\nu = h^\nu{}_\mu t^\mu, \tag{2.3}$$

$$\alpha = n_\mu t^\mu, \tag{2.4}$$

so that

$$t^\mu = \alpha n^\mu + \beta^\mu, \tag{2.5}$$

where $\alpha$ is called the lapse function (encoding the proper distance of the slices at that point as measured by an observer moving perpendicular to the slice) and $\beta^a$ the shift vector that is moving the points within a slice (compare Fig. (2.1)). The whole four dimensional line element can then be written as:

$$ds^2 = -(\alpha dx^0)^2 + \gamma_{ab}(dx^a + \beta^a dx^0)(dx^b + \beta^b dx^0). \tag{2.6}$$

Applying the projection tensor on the covariant derivative of the normal vector $n^\mu{}_{;\nu}$ is

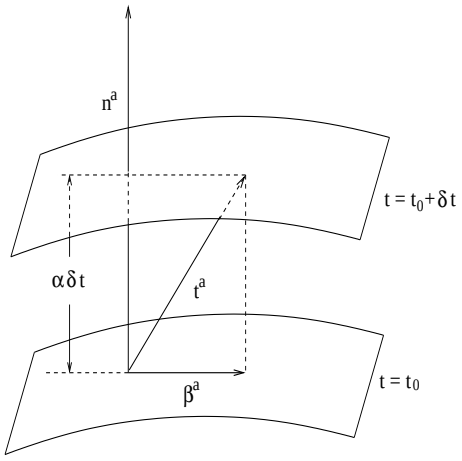


Figure 2.1: The 3+1 split. The points on the time slice at $t = t_0$ are mapped onto the succeeding timeslice $t = t_0 + \delta t$. The lapse function $\alpha$ gives the separation along the normal vector $n^a$ and the shift vector $\beta^a$ is used to move the points within the slice. The time coordinate is $t^a = \alpha n^a + \beta^a$.

introducing another important tensor: the extrinsic curvature (or second fundamental form):

$$K_{ab} := h^{\alpha}{}_{a} h^{\beta}{}_{b} n_{\alpha;\beta}. \tag{2.7}$$

By its construction $K_{ab}$ is a three dimensional object (it is projected down to the slice). It represents how the three dimensional manifold is embedded in the four dimensional one. This tensor has the important property:

$$K_{ab} = -\frac{1}{2}\mathcal{L}_n \gamma_{ab}, \tag{2.8}$$

where $K = \gamma^{ab} K_{ab}$ is the trace of $K_{ab}$. Eq. (2.8) is often taken as the actual definition of $K_{ab}$. $\mathcal{L}_n$ denotes the Lie-derivative with respect to the normal vector $n^a$ (see appendix C for the definition and some properties of the Lie-Derivative). It indicates that $K_{ab}$ can be seen as a generalization of the time derivative of the metric.

The original ADM split used another quantity, the canonic conjugate of the metric $\pi$ defined through

$$K^{ab} = K\gamma^{ab} - \gamma^{-\frac{1}{2}}\pi^{ab}. \tag{2.9}$$

This shows that $K_{ab}$ with its easily understood geometrical meaning is very close to the canonic variable. Therefore York in his rewriting of the ADM formalism used the extrinsic curvature instead of the canonical conjugate of the metric, a method that will be adapted here.

## 2.3 Formulations

### 2.3.1 ADM

Introducing the metric and the extrinsic curvature to the vacuum Einstein's equations leads (as shown in appendix A) to the so called ADM equations [25]. They still have this name even though they differ slightly from the original due to changes York proposed [125][1]:

$$R + K^2 - K^{ij}K_{ij} = 0, \tag{2.10}$$

$$D_j(K^{ij} - \gamma^{ij}\mathrm{tr}K) = 0. \tag{2.11}$$

$$\frac{d}{dt}\gamma_{ij} = -2\alpha K_{ij}, \tag{2.12}$$

$$\frac{d}{dt}K_{ij} = -D_iD_j\alpha + \alpha(R_{ij} + KK_{ij} - 2K_{ik}K^k_j), \tag{2.13}$$

where

$$\frac{d}{dt} = \frac{\partial}{\partial t} - \mathcal{L}_\beta. \tag{2.14}$$

Here $\mathcal{L}_\beta$ denotes the Lie derivative with respect to the shift vector $\beta^i$, $R$ the 3D scalar curvature constructed with the 3-metric $\gamma_{ab}$ of the 3-space, and $D_a$ the covariant derivative associated with $\gamma_{ab}$.

The first two equations (Eq. (2.10) and Eq. (2.11)) contain only spatial derivatives of the 3D scalar curvature (which has no time derivatives of the metric) and the extrinsic curvature. Therefore these equations do not contain second time derivatives of the metric. They are not evolution equations, but instead impose constraints on

[1] as mentioned above the original ADM paper used $\pi_{ab}$ instead of $K_{ab}$

the system. They are called Hamiltonian- (or Scalar-) and Momentum- (or Vector-) constraint, respectively. In spacetimes with matter the right hand sides of these equations include the energy density or the momentum density of this matter. This is where the names of the constraints come from.

The latter two equations (Eq. (2.12) and Eq. (2.13)) are the evolution equations for the geometrical quantities $\gamma_{ab}$ and $K_{ab}$. From the dynamical point of view (of geometrodynamics) they represent the actual second order (in space and time) differential equations for the three metric. To be able to solve them one has to give an initial metric $\gamma_{ab}$ and its time derivative $K_{ab}$. However, these cannot be given freely but are subject to the constraint Eqs. (2.10) and (2.11).

As shown in Appendix B the Bianchi identities guarantee that a solution of the constraint equations is also a solution of the evolution equations.

### 2.3.2 The BSSN Formulation

Until recently, the ADM formulation was the standard method of writing the equations for numerical relativity. Since in numerical evolutions the ADM system turned out to be unstable, several studies have been made to improve it [68, 69, 70, 71, 72, 63, 7, 24, 73]. All evolutions for this work are made with an alternative formulation whose success is largely induced by empirical experience. It separates out the conformal and traceless part of the ADM evolution equations, as proposed already in 1995 by Shibata and Nakamura [105]. However, the numerical relativity community did not take notice until Baumgarte and Shapiro [34] showed its remarkable stability properties by comparing the standard ADM formulation against the modified Shibata-Nakamura formulation. The group at AEI developed an implementation of this scheme: the "BSSN" (Baumgarte, Shapiro, Shibata, and Nakamura) formulation. This chapter explains the details of this formulation.

This system reformulates the ADM (Eqs. (2.12) and (2.13)) by introducing new

evolution variables. The metric is rewritten as:

$$\tilde{\gamma}_{ij} = e^{-4\phi}\gamma_{ij}. \tag{2.15}$$

The conformal factor $\phi$ is constraint by

$$e^{-4\phi} = \gamma^{1/3} \equiv \det(\gamma_{ij})^{1/3}, \tag{2.16}$$

which fixes the determinant of $\tilde{\gamma}$ to unity. Instead of the extrinsic curvature $K_{ij}$ here its trace free part $A_{ij}$ is used. It is defined by

$$A_{ij} := K_{ij} - \frac{1}{3}\gamma_{ij}K, \tag{2.17}$$

where $K = \gamma^{ij}K_{ij}$ is the trace of the extrinsic curvature. It is also conformally decomposed:

$$\tilde{A}_{ij} = e^{-4\phi}A_{ij}. \tag{2.18}$$

One can split Eq. (2.12) as

$$\frac{d}{dt}\tilde{\gamma}_{ij} = -2\alpha\tilde{A}_{ij}, \tag{2.19}$$

$$\frac{d}{dt}\phi = -\frac{1}{6}\alpha K. \tag{2.20}$$

Using the Hamiltonian constraint (Eq. (2.10)), the evolution equation for trace of the extrinsic curvature $K$ becomes

$$\frac{d}{dt}K = -\gamma^{ij}D_iD_j\alpha + \alpha(\tilde{A}_{ij}\tilde{A}^{ij} + \frac{1}{3}K^2). \tag{2.21}$$

The evolution equation for the trace free extrinsic curvature is

$$\frac{d}{dt}\tilde{A}_{ij} = e^{-4\phi}[-D_iD_j\alpha + \alpha(R_{ij} - S_{ij})]^{TF} + \alpha(K\tilde{A}_{ij} - 2\tilde{A}_{il}\tilde{A}^l_j).$$

The Ricci tensor can be written

$$R_{ij} = \tilde{R}_{ij} + R^{\phi}_{ij}, \tag{2.22}$$

where the conformal factor part $R^{\phi}$ is calculated by computation of derivatives of $\phi$:

$$R^{\phi}_{ij} = -2\tilde{D}_i\tilde{D}_j\phi - 2\tilde{\gamma}_{ij}\tilde{D}^l\tilde{D}_l\phi + 4\tilde{D}_i\phi\tilde{D}_j\phi - 4\tilde{\gamma}_{ij}\tilde{D}^l\phi\tilde{D}_l\phi.$$

The conformal part $\tilde{R}_{ij}$ can be computed from the conformal three metric $\tilde{\gamma}_{ij}$.[34] used an auxiliary variable which is called the "conformal connection function"

$$\tilde{\Gamma}^i = \tilde{\gamma}^{jk}\tilde{\Gamma}^i{}_{jk} = -\tilde{\gamma}^{ij}{}_{,j}, \tag{2.23}$$

where the second equality holds if the determinant of the conformal three metric $\tilde{\gamma}$ is actually unity. (This is analytically true, but it may turn out to be not so numerically.)

Using the conformal reconnection function, the Ricci tensor can be written as

$$\begin{aligned}\tilde{R}_{ij} &= -\frac{1}{2}\tilde{\gamma}^{lm}\tilde{\gamma}_{ij,lm} + \tilde{\gamma}_{k(i}\partial_{j)}\tilde{\Gamma}^k + \tilde{\Gamma}^k + \tilde{\Gamma}\tilde{\Gamma}_{(ij)k} \\ &\quad +\tilde{\gamma}^{lm}(2\tilde{\Gamma}^k{}_{l(i}\tilde{\Gamma}_{j)km} + \tilde{\Gamma}^k{}_{im}\tilde{\Gamma}_{klj}).\end{aligned} \tag{2.24}$$

One has a number of choices in how the terms involving the conformal connection function $\tilde{\Gamma}^i$ are computed. However, to guarantee the Ricci tensor retains its elliptic character, the $\tilde{\Gamma}^i$ should be promoted to independent variables.

The evolution equations for the $\tilde{\Gamma}^i$ are

$$\frac{\partial}{\partial t}\tilde{\Gamma}^i = -\frac{\partial}{\partial x^j}(2\alpha\tilde{A}^{ij} + 2\tilde{\gamma}^{(j}\beta^{i)}{}_{,m} - \frac{2}{3}\tilde{\gamma}^{ij}\beta^l{}_{,l} - \beta^l\tilde{\gamma}^{ij}{}_{,l}).$$

Empirical tests have shown that using the momentum constraints and eliminating the divergence of $\tilde{A}_{ij}$ results in the greatest improvements in numerical stability []. This turns Eq. (2.25) into

$$\begin{aligned}\frac{\partial}{\partial t}\tilde{\Gamma}^i &= -2\tilde{A}^{ij}\alpha_{,j} + 2\alpha(\tilde{\Gamma}^i{}_{jk}\tilde{A}^{kj} - \frac{2}{3}\tilde{\gamma}^{ij}K_{,j} - \tilde{\gamma}^{ij}S_j + 6\tilde{A}^{ij}\phi_{,j}) \\ &\quad +\frac{\partial}{\partial x^j}(\beta^l\tilde{\gamma}^{ij}{}_{,l} - 2\tilde{\gamma}^{m(i}\beta^{j)}{}_{,m} + \frac{2}{3}\tilde{\gamma}^{ij}\beta^l{}_{,l}).\end{aligned} \tag{2.25}$$

Now, there are seventeen evolution equations: six for the conformal three metric $\tilde{\gamma}_{ij}$ (Eq. (2.19)), six for the conformal traceless extrinsic curvature variables $\tilde{A}_{ij}$ (Eq. (2.22)), another one for the conformal factor (Eq. (2.20)), one for the trace of the extrinsic curvature $K$ (Eq. (2.21)), and three for the conformal connection functions (Eq. (2.25)).

For the work for this paper the BSSN scheme is implemented the following way:

- The $\Gamma^i$ are promoted to independent variables.
- The momentum constraint is used to transform the evolution equation for $\Gamma^i$.
- $tr\tilde{A} = 0$ is enforced at each time step.
- When maximal slicing is used, $trK = 0$ is enforced at each time-step.
- The constraints are not enforced.

Ideally one would like to know if the different systems are well-posed. However, the system of equations are mixed first-second order systems and as such they can not be classified in terms of their hyperbolicity. This makes a study of their well-posedness particularly difficult. The presence of constraints further complicates matters. Because of this fact, usually only linear perturbations of a flat background have been studied using a Fourier analysis.

Alcubierre Ref. [3] has given a mathematical understanding of the stability properties of the ADM and BSSN equations in the linear regime: The numerical errors, introduced through roundoff and machine precision are treated differently in the different systems. In the ADM system there are modes which do not propagate during the evolution, they stay in place and can grow undisturbed and eventually kill the run. The same modes, even though they may grow faster, are carried away in the BSSN system until the leave the grid. This comes to help the stability of the BSSN system on a finite domain.

## 2.4 Coordinate Conditions

A very important problem doing numerical evolutions of Einstein's equations is the choice of the gauge. One is allowed to choose the lapse and the shift function freely, corresponding to a choice of slicing and of coordinates within each slice. This does not change the physical properties of the metric. However, doing so can have large influence on the numerical evolutions.

The immediate idea would be to use so-called geodesic slicing: evolve with a lapse of 1 and a shift of 0 and let the grid-points float along geodesics. However, as can be shown analytically for the Schwarzschild solution, with such a slicing condition one would hit the singularity after a short time ($\pi$ M in the Schwarzschild case), causing any numerical code to crash. Therefore one has to use a more elaborate slicing.

The first results for colliding black holes were obtained for head-on collisions using the ADM decomposition of the Einstein equations with the lapse determined by the "maximal slicing" condition and the shift vector set to zero [108, 109, 23]. Maximal slices are slices that obey the condition

$$trK_{ab} \equiv K = 0, \tag{2.26}$$

with $trK_{ab}$ being the trace of the extrinsic curvature (also named mean curvature). Noting that $K = -\nabla_a n^a$, this states that the Eulerian world-lines are like those of an incompressible "test fluid". The name "maximal" comes from the fact that the volume of a bounded region $\Omega$ will be an extremum (with the metric's signature at hand it will be maximal, a Euclidian signature would give a minimum):

$$vol(\Omega) = \int_\Omega (det\gamma)^{\frac{1}{2}} d^3x. \tag{2.27}$$

Looking at the variation of the volume under small deformations of the slice along a vector $\lambda^a = ln^a + \sigma^a$, with $n_a\sigma^a = 0$, and $l = \sigma^a = 0$ on the boundary $\delta\Omega$:

$$\delta vol(\Omega) = \int_\Omega d^3x (det\gamma)^{\frac{1}{2}} \left[-lK\right], \tag{2.28}$$

one sees that since $l$ is arbitrary, one has to have $K = 0$ to get the variation vanish.

Maximal slices are those which maximize the volume. Those slices "avoid" regions with a large value of the three metric especially singularities. Therefore maximal slices are known to be singularity avoiding, that is, starting from black hole initial data where the physical singularity is to the future of the initial hypersurface, the lapse approaches the Minkowski value of unity in the asymptotically flat regions, but approaches zero near the physical singularity[2]. In this way one can in principle foliate a black hole spacetime without including singularities. However, since time marches on in the far regions while being frozen in the interior, the slices become more and more distorted (compare Fig. (2.2)). This stretching introduces a difficult problem for numerical simulations since the metric develops large gradients that continue to grow until the finite differencing can no longer handle them and fails. Advanced numerical methods can help in spherical symmetry, see e.g. [40], but to date have not proved successful in three dimensional (3D) evolutions [118].

Nonetheless, such singularity avoiding slicings with vanishing shift do allow black hole space-times to be evolved for long enough that useful physical information can be obtained, as first demonstrated in 1995 for the case of a single Schwarzschild black hole [20]. In [49] the first fully 3D simulation of the grazing collision of two nearby black holes (as measured by their apparent horizon separation) was performed with singularity avoiding slicing and vanishing shift, lasting for about $7M$. With improved techniques the grazing collision has recently been pushed to about $35M$, which for the first time allowed the extraction of gravitational waveforms from a 3D numerical merger [4]. And even though singularity avoiding slicings with vanishing shift have so far been limited to a finite time interval before slice stretching becomes a fatal

[2]Eardley and Smarr [66] have shown that this is not proven to be always the case. Counter-examples indicate that just requiring $trK$ to vanish is far too weak a condition to guarantee singularity avoidance. However, they conjectured that this requirement is strong enough in vacuum space-times.

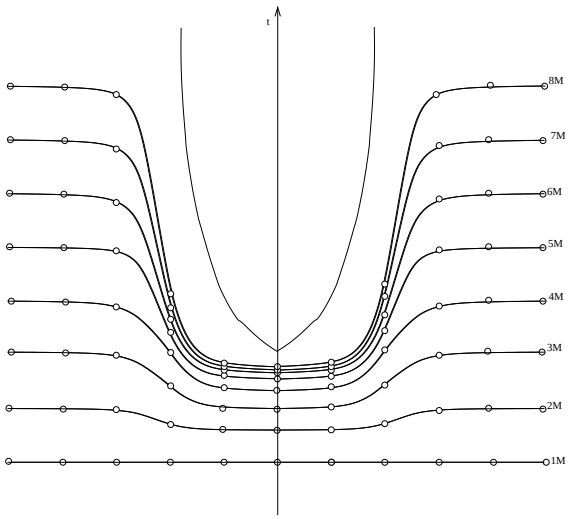


Figure 2.2: Singularity avoiding slicing. Starting from initial data where the physical singularity is to the future of the initial hypersurface, a singularity avoiding lapse keeps the Minkowski value of unity in the asymptotically flat regions, but approaches zero near the physical singularity. The slices get bent more and more in the intermediate region. The distance between points grows, which eventually leads to problems.

problem, this interval can be moved into the truly non-linear regime of a plunge starting from an approximate innermost stable circular orbit (ISCO) of two black holes, since the remainder of the merger and ring-down can be computed using the before mentioned close limit approximation [30]. Following such an approach, the first waveforms for the plunge from an approximate ISCO have been obtained [27].

So far the most important strategy to avoid slice stretching has been black hole excision explained in detail in chapter 4.4. One of the key differences between black hole excision and the use of singularity avoiding slicings with vanishing shift is that with excision single static black holes can be stably evolved for essentially unlimited amounts of time, as shown by the AEI group in [6].

However, using newly developed gauge conditions the AEI group could show that it is even possible to drive a distorted black hole system toward an essentially static state, avoiding the chronic growth in metric functions typical of slice stretching[3].

[3]Slice stretching is not completely eliminated [36]

Hence, in principle they should allow for indefinitely long evolutions. Moreover, since unbounded growth in metric functions is halted, they allow much more accurate results to be obtained for extremely long times, and at lower resolution than before. The group obtained results for colliding black holes showing at low resolution only 10% error in the horizon mass after more than $5000M$ of evolution.

One fundamental observation for this choice of shift vector is that the "Gamma freezing" shift introduced in [12] has a useful property when the black holes are not excised but are represented as punctures: Initially the shift is zero, but as the slice stretching develops, the shift reacts by pulling out points from the inner asymptotically flat region near the punctures. The lapse and shift conditions taken together are then able to virtually stop the evolution of one or even two black holes, essentially mimicking the behavior of the lapse and shift known from stable evolutions of a black hole in Kerr-Schild coordinates. This is a key result that will be detailed below.

### 2.4.1 The Lapse Function

The starting point for the slicing conditions is the "$K$-freezing" condition $\partial_t K{=}0$, which in the particular case when $K{=}0$ reduces to the well known "maximal slicing" condition. The $K$-freezing condition leads to the following elliptic equation for the lapse:

$$\Delta\alpha = \beta^i \partial_i K + \alpha K_{ij} K^{ij} \,, \tag{2.29}$$

with $\Delta$ the Laplacian operator for the spatial metric $\gamma_{ij}$. In the BSSN formulation, once the elliptic equation for the lapse is solved, the $K$-freezing condition can be imposed at the analytic level by simply not evolving $K$.

One can construct parabolic or hyperbolic slicing conditions by making either $\partial_t \alpha$ or $\partial_t^2 \alpha$ proportional to $\partial_t K$. Following [32] such conditions are called "K-driver". The hyperbolic K-driver condition has the form [40, 12]:

$$\partial_t \alpha \;\; = \;\; -\alpha^2 f(\alpha)(K - K_0), \tag{2.30}$$

where $f(\alpha)$ is an arbitrary positive function of $\alpha$ and $K_0 = K(t=0)$. A choice used for most successful black hole evolutions is

$$f(\alpha) = \frac{2}{\alpha}, \tag{2.31}$$

which is referred to as 1+log slicing and has excellent singularity avoiding properties. The hyperbolic K-driver condition is in fact only a slight generalization of the Bona-Masso family of slicing conditions [40]: $\partial_t \alpha = -\alpha^2 f(\alpha) K$.

By taking an extra time derivative of the slicing condition above, and using the evolution equation for $K$, one can see that the lapse obeys a generalized wave equation,

$$\begin{aligned} \partial_t^2 \alpha &= -\partial_t(\alpha^2 f)(K - K_0) - \alpha^2 f \partial_t K \\ &= \alpha^2 f(\Delta\alpha - \alpha K_{ij} K^{ij} - \beta^i D_i K + 2\alpha f + \alpha^2 f'). \end{aligned} \tag{2.32}$$

In black hole evolutions where the lapse collapses to zero, condition (2.30) guarantees that the lapse will stop evolving. In practice the condition Eq. (2.30) leads to more stable black hole evolutions.

The wave speed is $v_\alpha = \alpha\sqrt{f(\alpha)}$, which explains the need for $f(\alpha)$ to be positive. Depending on the value of $f(\alpha)$, this wave speed can be larger or smaller than the physical speed of light. This represents no problem, as it only indicates the speed of propagation of the coordinate system, i.e. it is only a "gauge speed". In particular, for the 1+log slicing introduced above with $f = 2/\alpha$, the gauge speed in the asymptotic regions (where $\alpha \simeq 1$) becomes $v_\alpha = \sqrt{2} > 1$. One could then argue that choosing $f = 1/\alpha$ should be a better alternative, as the asymptotic gauge speed would then be equal to the physical speed of light. However, experience has shown that such a choice is not nearly as robust and seems to lead easily to gauge pathologies as those studied in [2, 8].

### 2.4.2 Shift conditions

In the BSSN formulation, an elliptic shift condition is easily obtained by imposing the "Gamma-freezing" condition $\partial_t \tilde{\Gamma}^k$=0, or using Eq. (2.25),

$$\begin{aligned}\tilde{\gamma}^{jk}\partial_j\partial_k\beta^i + \frac{1}{3}\tilde{\gamma}^{ij}\partial_j\partial_k\beta^k - \tilde{\Gamma}^j\partial_j\beta^i + \frac{2}{3}\tilde{\Gamma}^i\partial_j\beta^j + \beta^j\partial_j\tilde{\Gamma}^i \\ -2\tilde{A}^{ij}\partial_j\alpha - 2\alpha\left(\frac{2}{3}\tilde{\gamma}^{ij}\partial_j K - 6\tilde{A}^{ij}\partial_j\phi - \tilde{\Gamma}^i_{jk}\tilde{A}^{jk}\right) = 0.\end{aligned} \tag{2.33}$$

Just as with the $K$-freezing condition for the lapse, once the previous elliptic equations for the shift is solved, the Gamma-freezing condition can be enforced at an analytic level by simply not evolving the $\tilde{\Gamma}^k$.

The Gamma-freezing condition is related to the well known minimal distortion shift condition [110]:

$$\nabla_j \Sigma^{ij} = 0\,, \tag{2.34}$$

where $\Sigma_{ij}$ is the so-called "distortion tensor" defined as

$$\Sigma_{ij} := \frac{1}{2}\gamma^{1/3}\partial_t\tilde{\gamma}_{ij}\,, \tag{2.35}$$

with $\tilde{\gamma}_{ij}$ the same as before. The evolution equation for the conformal connection functions (2.25) can be written in terms of $\Sigma_{ij}$ as

$$\partial_t\tilde{\Gamma}^i = 2\partial_j\left(\gamma^{1/3}\Sigma^{ij}\right)\,. \tag{2.36}$$

More explicitly

$$\partial_t\tilde{\Gamma}^i = 2e^{4\phi}\left[\nabla_j\Sigma^{ij} - \tilde{\Gamma}^i_{jk}\Sigma^{jk} - 6\Sigma^{ij}\partial_j\phi\right]\,. \tag{2.37}$$

This shows that the minimal distortion condition $\nabla^j\Sigma_{ij} = 0$, and the Gamma-freezing condition $\partial_t\tilde{\Gamma}^i = 0$ are equivalent up to terms involving first spatial derivatives of the spatial metric multiplied with the distortion tensor itself. In particular, all terms involving second derivatives of the shift are identical in both cases (but not so terms with first derivatives of the shift which appear in the distortion tensor $\Sigma_{ij}$).

That the difference between both conditions involves Christoffel symbols should not be surprising since the minimal distortion condition is covariant while the Gamma-freezing condition is not.

Just as it is the case with the lapse, one can obtain parabolic and hyperbolic shift prescriptions by making either $\partial_t \beta^i$ or $\partial_t^2 \beta^i$ proportional to $\partial_t \tilde{\Gamma}^i$ and call such conditions "Gamma-driver" conditions. The parabolic Gamma driver condition has the form

$$\partial_t \beta^i = F_p \, \partial_t \tilde{\Gamma}^i \,, \tag{2.38}$$

where $F_p$ is a positive function of space and time. As a hyperbolic Gamma driver condition

$$\partial_t^2 \beta^i = F \, \partial_t \tilde{\Gamma}^i - \eta \, \partial_t \beta^i, \tag{2.39}$$

was taken, where $F$ and $\eta$ are positive functions of space and time. For the hyperbolic Gamma-driver conditions it turned out to be crucial to add a dissipation term with coefficient $\eta$ to avoid strong oscillations in the shift. Experience has shown that by tuning the value of this dissipation coefficient one can manage to almost freeze the evolution of the system at late times.

An important point that needs to be considered when using the hyperbolic Gamma-driver condition is that of the gauge speeds. Just as it happened with the lapse, the use of a hyperbolic equation for the shift introduces new "gauge speeds" associated with the propagation of the shift. Consider the shift condition (2.39) for small perturbations of flat space (and taking $\eta$=0). From the form of $\partial_t \tilde{\Gamma}^i$ given by (2.19) one can see that in such a limit the principal part of the evolution equation for the shift reduces to

$$\partial_t^2 \beta^i = F \left( \delta^{jk} \partial_j \partial_k \beta^i + \frac{1}{3} \, \delta^{ij} \partial_j \partial_k \beta^k \right) . \tag{2.40}$$

Considering only derivatives in $x$ direction one finds

$$\partial_t^2 \beta^i = F \left( \partial_x^2 \beta^i + \frac{1}{3} \, \delta^{ix} \partial_x \partial_x \beta^x \right) , \tag{2.41}$$

which implies

$$\partial_t^2 \beta^x = \frac{4}{3} F \partial_x^2 \beta^x \,, \tag{2.42}$$

$$\partial_t^2 \beta^q = F \partial_x^2 \beta^q \qquad q \neq x \,. \tag{2.43}$$

This shows that in regions where the spacetime is almost flat, the longitudinal part of the shift propagates with speed $v_{\rm long} = 2\sqrt{F/3}$ while the transverse part propagates with speed $v_{\rm trans} = \sqrt{F}$. Therefore the choice

$$F(\alpha) = \frac{3}{4}\,\alpha, \tag{2.44}$$

will make the longitudinal part of the shift propagate with the speed of light. The transverse part will propagate at a different speed, but its contribution far away is typically very small.

Using these lapse and shift conditions combined it was possible to bring the dynamics in binary black hole evolutions basically to a halt at late times and with that to extend the lifetime of such evolutions dramatically.

### 2.4.3 Co-rotation

Astrophysically realistic binary systems will of course generally be in orbit about each other. From a computational point of view, this would mean that the objects must be propagated around each other across the computational grid. This can introduce many complications in the numerical treatment, chief among them that (*i*) orbital motion could lead to a tangling of coordinate systems in numerical relativity, (*ii*) propagating objects such as black holes or neutron stars across a numerical grid leads to dissipation which in turn leads to artificial loss of a number of quantities like angular or linear momentum, and (*iii*) moving black holes across a numerical grid with excision techniques (see section 4.4) is extremely complex computationally, and has still some time to mature before it can be used in such calculations.

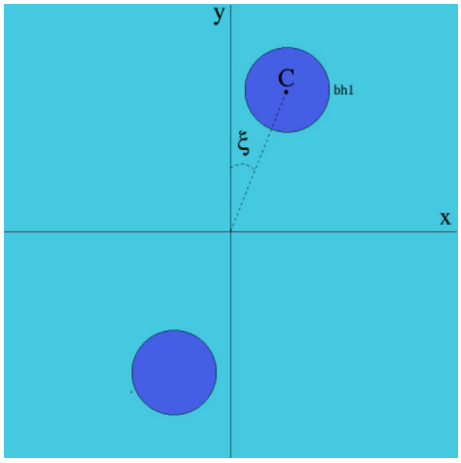


Figure 2.3: The drift-correct method. The centroid $C$ of one of the black holes is tracked, the angle $\xi$ measured, the effective angular velocity of the centroid $\Omega_c$ is computed, and the shift vector is changed according to Eq. (2.46).

If a suitable co-rotating frame could be developed for binary systems, so that in the frame of the calculations the objects do not orbit each other, but rather simply fall together, the problem simplifies dramatically, as orbital dynamics are effectively eliminated from the calculation. In this case, the problem becomes similar to a head-on collision, which is clearly much simpler, and which, as described above, has already been performed very robustly and accurately in simpler systems.

The new method, developed within the work of this thesis [13], consists of tracking the centroids of the black hole horizons and adjusting the shift to counteract this motion, or "drift". This is why it is called "drift correction". The centroid $C$ of the horizon $H_1$ of one of the black holes is calculated by taking the arithmetic mean of the points on the horizon. Then the angle $\xi$ between some fiducial line, such as the y-axis, and the line connecting the centroid with the the origin of our coordinate system is calculated. By measuring $\xi$ at regular intervals of coordinate time in the simulation, a measure of the "angular velocity" of the centroid is gained, which is then counteracted by applying a corresponding rotation $\Omega_c$ in the opposite direction.

If the angle $\xi$ changes by an amount $\Delta\xi$ in a time $\Delta t$, the "angular velocity" $\Omega_c$ is given by

$$\Omega_c = -k\Delta\xi/\Delta t, \tag{2.45}$$

where $k$ is some adjustable parameter of order unity, and the minus sign indicates a correction in a direction opposite to the drift. Choosing $k$ slightly greater than 1, e.g. $k = 1.3$, to over-correct by a small amount, turns out to be best in practice because the drift correction might only be applied at intervals ($\Delta t$) of several time-steps. This $\Omega_c$ is then added to the angular component of the shift at all points $(x, y, z)$ in the simulation domain:

$$\begin{aligned} \beta^x{}_{dc} &:= \beta_x - y\,\Omega_c\,f \\ \beta^y{}_{dc} &:= \beta_y - x\,\Omega_c\,f, \end{aligned} \tag{2.46}$$

where $f(x, y, z)$ is some adjustment function of the spacetime curvature and the index $dc$ stands for drift-correction.

The function $f(x, y, z)$ used with black hole puncture data (see section 3.2.3) ensures that the shift goes to zero at the punctures. For example one can use $f = 1/\psi^\alpha$, where $\psi$ is the conformal factor which goes to infinity at the punctures, and $\alpha$ is some positive power.

An additional radial drift-correction can be introduced to calm the motion of the coordinates even more:

$$\beta^i{}_{dc} = \beta^i g(r, \dot{r}), \tag{2.47}$$

where $i = 1, 2$ and $g$ is some function of the radius $r$ and its time derivative $\dot{r}$.

First successful tests have been done using this improved gauge condition showing improved results (see chapter 6).

Note that also other grid-functions can be tracked to adjust the shift. For instance the lapse function. Experience has shown that with maximal slicing of single black hole evolutions when the lapse function drops below 0.3 an apparent horizon will

appear. So a code could use iso-surfaces of $\alpha = 0.3$ instead of an apparent horizon finder to estimate the black hole location.

# Chapter 3

# The Initial Data Problem

## 3.1 Introduction

As described in chapter 2 a numerical solution of Einstein's equations starts with initial data which solve the constraint equations (Eq. (2.10) and Eq. (2.11)). This chapter will describe methods to solve them. It will explain the usually used sets of initial data, introduce recently published new ways of solving the equations and come in the last section to a new construction method that was developed in the course of this thesis.

A solution of the constraint equations sets the physical properties of the system. While it is a difficult problem to write the evolution equations in a suitable way, to solve them accurately enough, and to get them to converge to a solution, in principle they deterministically evolve a system with the physical (and numerical) properties set by the initial data. No new information is needed nor gained. It is therefore of extreme importance how the initial data constraints are solved and what the properties are, that where given to the system.

The problem of solving the constraints is threefold:

- decomposing the variables into a set of freely specifiable variables and the variables that are determined by the constraint equations
- choosing values for the free variables corresponding to a desired physical system

- solving the constraint equations

The first task becomes clear, when counting equations and variables: there are 4 (3+1) equations for the 12 (2 x 6) variables $\gamma_{ab}$ and $K_{ab}$. The system is heavily underdetermined. This is not a flaw of the theory but a virtue: it allows for the principle of general covariance.

However, there is nothing to say which variables are to be chosen freely and which are not. So even before anything can be set to be physical (or not) a choice has to be made on how to decompose the variables into freely specifiable ones and in components that are fixed by the equations. The resulting equations will vary in mathematical as well as in numerical terms. So the choice of the decomposition is very important in determining the solution of the initial value problem.

The second task than is easily understood: the variables that are chosen to be freely set and are not determined through the equations now have to be set. While in principle this choice is free, to set them to anything meaningful or physically reasonable is in fact quite difficult. As will be seen later these variables not always have a direct physical meaning, yet they influence the physical properties of the system. And they can complicate the equations mathematically. So up to very recently the choice was made rather for mathematical simplicity or convenience than for physical relevance.

The last task can be mathematically very involved, depending on the choice of decomposition the character of the equations changes. In full generality, they become a system of strongly coupled, non-linear, and elliptic or semi-elliptic second order differential equations. There is only a very limited number of analytic solutions known to some special cases. As soon as the simplifying symmetries or additional assumptions are left out, very sophisticated numerical methods are needed to treat them. Since the solution is global on the slice a suitable choice of boundary conditions has to be made - preferably based on physical grounds, which will determine which

solution is found. Once that is done, the equations have to be solved. Regular methods usually slow down very rapidly when the number of grid points increases. More sophisticated methods as for instance a multi-grid solver have to be used to speed the solution procedure.

This chapter will describe the most commonly used decomposition of the constraints, the one proposed by York and Lichnerowicz [125] and deal with some solutions to the binary black hole problem. This subject is explained in great detail in [59]. Additionally a newly suggested decomposition, not relying on Yorks procedure, will be explained.

## 3.2 Solving the Constraints (I): The York Procedure

The constraint equations pose a set of four differential equations on the 12 functions $\gamma_{ab}$ and $K_{ab}$. Taking general covariance into account which gives the freedom to chose four coordinate functions freely, one is left with eight degrees of freedom. The problem at hand is which of the 12 variables should be regarded as freely specifiable.

Already in 1944 Lichnerowicz proposed to decompose the 3-metric via a conformal transformation [85]:

$$\gamma_{ab} = \Psi^4 \tilde{\gamma}_{ab}, \tag{3.1}$$

where $\Psi$ is the conformal factor and $\tilde{\gamma}_{ab}$ the conformal or background metric. Having the conformal metric freely specifiable, this equation will fix 5 of the 8 free degrees. The Hamiltonian constraint becomes an equation for the conformal factor:

$$\tilde{\nabla}^2\Psi = \frac{1}{8}\Psi\tilde{R} - \frac{1}{8}\Psi^5 K^2 + \frac{1}{8}\psi^5 K_{ab}K^{ab} = -2\pi G\Psi^5\rho, \tag{3.2}$$

where $\tilde{\nabla}^2 = \tilde{\nabla}_a\tilde{\nabla}^a$ and $\tilde{\nabla}^a$ and $\tilde{R}$ are the covariant derivative and the Ricci Scalar constructed with the conformal metric $\tilde{\gamma}_{ab}$ (all variables marked with a tilde will refer

to objects in the conformal space). The right hand side comes from the energy-momentum tensor, which is zero in vacuum (black hole) spacetimes.

A treatment of the extrinsic curvature, and with that the full decomposition, was described by York. It follows a similar path. First the extrinsic curvature is split into a trace free part and the trace:

$$K_{ab} = A_{ab} + \frac{1}{3} K \gamma_{ab}. \tag{3.3}$$

Second, a general property of trace-free symmetric tensors is used. They can be decomposed as follows [123]:

$$S^{ab} = (LX)^{ab} + T^{ab}, \tag{3.4}$$

where $T^{ab}$ is a symmetric transverse-traceless tensor (i.e. $\nabla_b T^{ab} = 0$ and $T^a_a = 0$) and the vector operator $(LX)^{ab}$ is (in three dimensions) defined by

$$(LX)^{ab} = \nabla^a X^b + \nabla^b X^a - \frac{2}{3} \gamma^{ab} \nabla_c X^c \tag{3.5}$$

Now there are two ways to proceed. Either this property is used directly on the trace-free part of the extrinsic curvature, $A_{ab}$, and the result is split into a conformal part and a factor; or the order is reversed. The two procedures conformal splitting and transverse splitting do not commute. Depending on the order of operations, the decomposition is called "conformal" or "physical" transverse-traceless decomposition respectively. The free variables as well as the resulting equations are different, so it is no surprise that the resulting solutions are different (see for a comparison [99]). Using the conformal transverse traceless decomposition one ends up with the following equations:

$$A^{ab} = \Psi^{-10} \tilde{A}^{ab} \tag{3.6}$$

$$\tilde{A}^{ab} = (LV)^{ab} + \tilde{M}^{ab} \tag{3.7}$$

$$\tilde{\nabla}_b (LX)^{ab} = \frac{2}{3} \Psi^6 \nabla^a K + 8\pi G \Psi^6 j^a. \tag{3.8}$$

The choice of the exponent in Eq. (3.6) for the conformal split of the extrinsic curvature is made because of the resulting useful property of every symmetric trace free tensor:

$$\Psi^{10}\tilde{\nabla}_b S^{ab} = \tilde{\nabla}_b(\Psi^{10} S^{ab}) \tag{3.9}$$

Again the terms including the energy flow $j^a$ stem from the energy momentum tensor and will be omitted in the following.

In contrast, the physical transverse traceless decomposition leads to:

$$\begin{aligned}
A^{ab} &= (LV)^{ab} + M^{ab} && (3.10)\\
\tilde{A}^{ab} &= (LV)^{ab} + \tilde{M}^{ab} && (3.11)\\
(LV)^{ab} &= \Psi^{-4}((\tilde{L}V)^{ab}) && (3.12)\\
M^{ab} &= \Psi^{10}(\tilde{M}^{ab}) && (3.13)\\
\tilde{\nabla}_b(LV)^{ab} + 6(\tilde{L}V)^{ab}\tilde{\nabla}_b ln\Psi &= \frac{2}{3}\tilde{\nabla}^a K - \Psi^6 \nabla_b M^{ab} + 8\pi G \Psi^4 j^a && (3.14)
\end{aligned}$$

As mentioned above these systems are different and will in general lead to different solutions. Comparing the two systems one notices that they are both coupled, but that the conformal transverse traceless decomposition leads to decoupled equations if $K = \gamma_{ab}K^{ab}$ is set to zero. Since this simplifies the solution procedure crucially, this is the method usually used (also for this paper) when dealing with the York-Lichnerowicz procedure.

### 3.2.1 Binary black holes

Once the decomposition has been chosen, the free variables must be fixed. The simplest choice would be a flat conformal metric $\gamma_{ab} = \delta_{ab}$, and vanishing extrinsic curvature, $K_{ab} = 0$. This simplifies the constraint equations dramatically. The momentum constraint is solved identically and the Hamiltonian constraint becomes:

$$\tilde{\nabla}^2 \Psi = 0, \tag{3.15}$$

where $\tilde{\nabla}^2$ is the Laplace operator built with the conformal metric, so in case it is the regular flat Laplace operator. The simplest solution of these equations certainly is $\Psi = 1$, which will result in a flat (Minkowski) metric. A solution found just as easily is $\Psi = 1 + c/r$, which is (with the right choice of the lapse and $c = M/2$) the well known Schwarzschild solution in isotropic coordinates, that led to the famous picture of the Einstein-Rosen bridge:

$$ds^2 = -(\frac{1 - \frac{M}{2r}}{1 + \frac{M}{2r}})^2 dt^2 + (1 + \frac{M}{2r})^4 (dr^2 + r^2 d\theta^2 + r^2 \sin^2\theta d\phi^2), \tag{3.16}$$

The metric is not changed (isometric) under reflections at the event horizon (located at $r = M/2$), mapping the exterior region to an "upper sheet" and the interior to a "lower" sheet. This can be pictured as shown in Fig. (3.1).

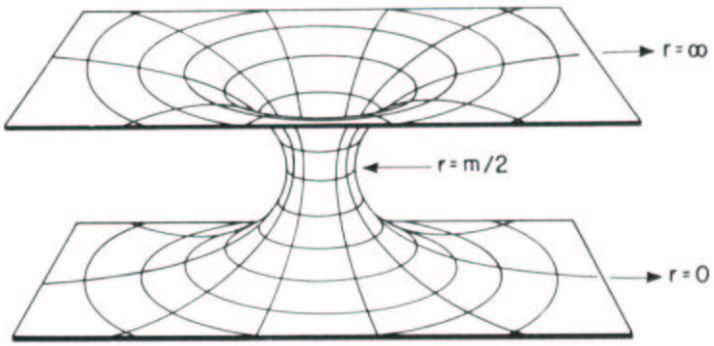


Figure 3.1: Visualization of an Einstein-Rosen Bridge. The interior of a black hole is mapped onto a manifold with the same metric as the exterior part. The singularity is only a coordinate singularity, a compactified spatial infinity.

As can be seen easily here, in these coordinates the point $r = 0$ is not a physical singularity but simply a coordinate artefact. The physical singularity lies in to future of this picture.

Now a nice property of Eq. (3.15) comes into play: it is linear. Therefore two solutions can be added to become a third one:

$$\Psi = 1 + \frac{m_1}{2r_1} + \frac{m_2}{2r_2} \tag{3.17}$$

or, more generally, $N$ black holes can be added.

$$\Psi = 1 + \sum_{i}^{N} \frac{m_{(i)}}{2|\vec{r} - \vec{r}_{(i)}|} \tag{3.18}$$

is a solution to the constraint equations encoding $N$ black holes, the so-called Brill-Linquist solution [47]. The black holes are momentarily at rest and will via the evolution equations collide "head on" meaning with no angular momentum involved. Topologically they resemble a three-sheeted topology shown in Fig. (3.2).

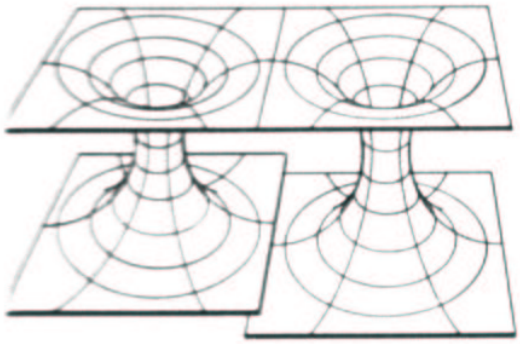

Figure 3.2: Visualization of a three sheeted topology, the lower parts are not connected. Each black hole's interior is mapped to a different manifold. These lower manifolds do not have the same metric as the "upper", exterior ones.

Misner [89] found an isotropic solution, for which there are two identical sheets. He used the so-called "bispherical coordinates":

$$\coth\mu = \frac{x^2 + y^2 + z^2 + a^2}{2az} \tag{3.19}$$

$$\cot\eta = \frac{x^2 + y^2 + z^2 - a^2}{2a\sqrt{x^2 + y^2}} \tag{3.20}$$

$$\cot\phi = \frac{x}{y}, \tag{3.21}$$

with $a$ a scale parameter with dimension length. One can check that $\mu$=const. is a sphere. So choosing $\mu = \pm\mu_0$ and demanding $\mu$ to be periodic (that is identifying the points $(\mu, \eta\phi)$ and $(\mu + 2n\mu_0, \eta, \phi)$) one can create a manifold with topology shown in

Fig. (3.4) (the original wormhole). Misner used York's conformal split of the metric (see section 3.2) and the following metric as conformal metric:

$$d\bar{s}^2 = d\mu^2 + d\eta^2 \sin^2\eta d\phi^2. \tag{3.22}$$

Choosing boundary conditions of asymptotic flatness, periodicity of the coordinates, mirror symmetry in the z=0 plane (the two spheres (and so their masses) are identical), and rotational symmetry about the z-axis, the unique solution of the Hamiltonian constraint is:

$$\Psi = a^{\frac{1}{2}} \sum_{n=-\infty}^{\infty} \left[\cosh(\mu + 2n\mu_0) - \cos\eta\right]^{-\frac{1}{2}}. \tag{3.23}$$

The parameters $\mu_o$ and $a$ can be related to the total mass M of the system and to the length $L_0$ of the minimal closed 3-geodesic connecting the two mouths through the formulas:

$$\mathrm{M} = 4a \sum_{n=1}^{\infty} \mathrm{csch\ n\ } \mu_0 \tag{3.24}$$

$$\mathrm{L_0} = 2a \left[1 + 2\mu_0 \sum_{n=1}^{\infty} \mathrm{n\ csch\ n\ } \mu_0\right]. \tag{3.25}$$

This solution also encodes two black holes momentarily at rest and about to collide head on. The difference to the Brill-Linquist data is their topology. Misner's data represent a two-sheeted topology. As can be seen in Fig. (3.4) Misner data contain an infinite number of singular points for each black hole, each representing an image of one of two asymptotic infinities (each hole is "seen" infinitely many times though the other black hole's throat). In Eq. (3.23) this is taken into account in the infinite summation.

Note that even though the Brill-Lindquist and the Misner data differ in their topology, solutions where the black holes are chosen to have the same size and separation are locally very similar [1].

Both the Misner and the Brill-Linquist data encode head-on collisions, a situation unlikely to be found in reality.

The Misner data have been a well studied test case for numerical relativity. Brill-Linquist data is becoming more popular now due to generalizations to orbiting data., which will be subject of the following section.

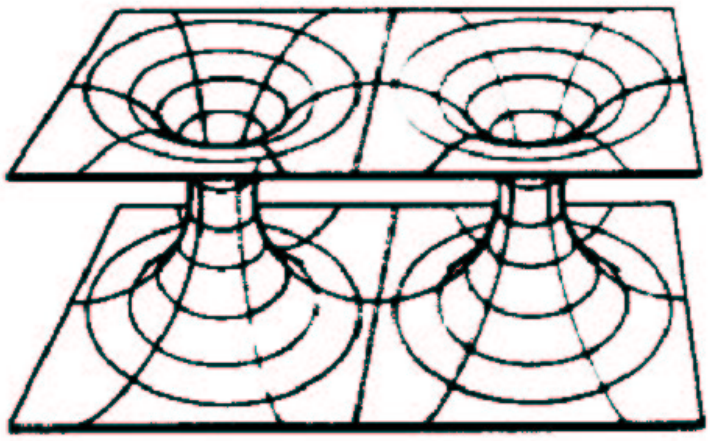

Figure 3.3: Visualization of a two sheeted topology, all throats end in the same (lower) manifold. This manifold has the same metric as the upper one.

### 3.2.2 Treating the Extrinsic Curvature

Bowen and York [44, 45] found a solution for the momentum constraint, corresponding to multiple black holes with angular or linear momentum, generalizing Misner's solution. They assume a conformally flat metric and vanishing trace of the extrinsic curvature ($K = 0$, maximal slicing), but chose the trace free part of the extrinsic curvature to be non vanishing.

They use the above mentioned conformal transverse traceless decomposition, starting with the split

$$\tilde{A}^{ij} = \tilde{A}^{ij}_{*} + (\tilde{L}W)^{ij}, \tag{3.26}$$

where $(\tilde{L}W)^{ij} = \tilde{D}^i W^j + \tilde{D}^j W^i - 2/3\gamma^{ij}\tilde{D}_k W^k$, and chose the transverse part to

vanish: $\tilde{A}^{ij}_* = 0$ Then the momentum constraints become:

$$\tilde{D}_j(\tilde{L}W)^{ij} = 0, \tag{3.27}$$

which has the the solution

$$W^i = -\frac{1}{4r}(7P^i + n^i n_j P^j) + \frac{1}{r^2}\epsilon^{ijk} n_j S_k, \tag{3.28}$$

with $P^i$ and $S^i$ being vector parameters, $r$ a coordinate radius, $n^i$ radial vectors normal to the $i$th black hole, and $\epsilon^{ijk}$ denoting the 3 dimensional Levi-Civita tensor. This solution of the momentum constraints yields the trace free part of the extrinsic

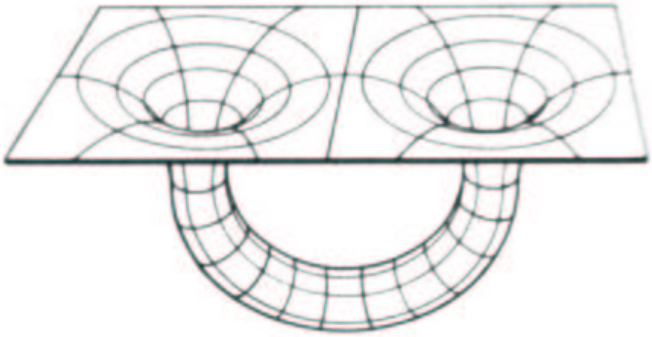

Figure 3.4: Two black holes in the classic wormhole picture as a topology of flat space with a handle.

curvature

$$\tilde{A}_{ij} = \frac{3}{2r^2}(P_i n_j + P_j n_i - (f_{ij} - n_i n_j)P^k n_k) + \frac{3}{r^3}(\epsilon_{ijk} S^l n^k n_j + \epsilon_{kil} S^l n^k n_i). \tag{3.29}$$

Again, due to the linearity of the momentum constraint, an arbitrary number of black holes can be constructed by adding different extrinsic curvatures as given in Eq. (3.29), with different positions, linear and angular momenta. Using this extrinsic curvature together with the metric reconstructed from the conformal factor (which is a solution of the Hamiltonian constraint) and the flat conformal metric, one can create initial data representing $N$ black holes, each with arbitrary linear and angular

momentum. However, the parameters $P^a$ and $S^a$ that denote in a single black hole solution the linear and angular momenta cannot be taken as such to encode literally the individual momenta of the different black holes. These quantities are only defined in the limit of infinite separation of the holes. But one very useful property of these data is, that unlike in other constructions, here the total linear momentum computed as expected agrees with the ADM value, defined later:

$$P_{tot} = P_1 + P_2. \tag{3.30}$$

For the angular momentum,

$$S_{tot} = S_1 + S_2 + (C_1 - O) \times P_1 + (C_2 - O) \times P_2. \tag{3.31}$$

In both equations (Eq. (3.30) and Eq. (3.31)), $P_i$ is taken to be the vector of the specified parameter values for the linear momenta, $S_i$ for the angular momenta and $C_i$ for the positions of the individual black holes.

From the ADM split it is known that the total momentum for the linear and angular momentum of initial data can be calculated in an asymptotically flat initial data hypersurface from the integral

$$\Pi^i \xi^i_{(k)} = \frac{1}{8\pi} \oint_\infty (K^j_i - \delta^j_i K) \xi^i_{(k)} d^2 S_j. \tag{3.32}$$

where $\xi^i_{(k)}$ is a killing vector of the 3 metric $\gamma_{ij}$. If $\xi^i_{(k)}$ is the translational killing vector, Eq. (3.32) represents the linear momentum in the direction of that killing vector, and if it is a rotational killing vector, Eq. (3.32) represents the angular momentum. Even though there are usually no real killing vectors involved, it is enough to use the asymptotic translational and rotational killing vectors of the flat conformal metric to show that $P^i$ is the physical linear momentum and $S^i$ the physical angular momentum of the (one black hole) system. And, since the momentum constraint here is linear, one can add several solutions of the form of Eq. (3.29) and get the total linear momentum of the system just as a vector sum of the several $P^i$. As shown in [122],

the total angular momentum is not as easily computed but it is possible to compute it without solving the Hamiltonian constraint.

Bowen- York data are not inversion symmetric. The problem can be pictured looking at 3.3: As with the Misner data in the inversion symmetric topology a black hole "sees" through the other black hole itself and again through the other itself again and so on. This is taken into account by the conformal imaging procedure proposed by Misner. It changes the extrinsic curvature by taking a sum over infinitely many images a black hole "sees" from itself and the others[1].

Cook used this conformal imaging procedure to create fully general 3d inversion symmetric data [58]. As will be explained in more detail later, he used these data to construct an evolutionary sequence of initial data sets in quasi circular orbits, later called the Cook sequence. The construction of these data is complicated and expensive. Therefore a simplification was needed to make numerical evolutions more practical.

### 3.2.3 Puncture Data

Puncture (or Brand-Brügmann) data are a modification of the Brill-Linquist data [46] to simplify the solution procedure. The construction starts with the same assumptions as the Bowen and York data described last section (conformal flatness $\gamma_{ab} = \delta_{ab}$, maximal slicing $K = 0$). Thus the momentum constraint is solved analytically by the same Bowen-York extrinsic curvature. However, the Hamiltonian constraint is rewritten. Based on the Brill-Linquist solution, it is a reasonable assumption to set the conformal factor to be:

$$\Psi = \frac{1}{\mu} + u, \tag{3.33}$$

[1]The actual sum and all its constituent terms are quite complicate, and not treated here because Misner data were not used in this thesis. All details can be found in [56].

where

$$\frac{1}{\mu} = \sum_{\lambda=1}^{N} \frac{m_\lambda}{2|\vec{r} - \vec{r}_\lambda|}. \tag{3.34}$$

Substituting Eq. (3.33) into the Hamiltonian constraint yields:

$$\tilde{\nabla}^2 u = \nu(1 + \mu u)^{-7} = 0, \tag{3.35}$$

with

$$\nu = \frac{1}{8}\mu^7 \tilde{A}_{ab}\tilde{A}^{ab}. \tag{3.36}$$

The point here is that the $\frac{1}{\mu}$ part is a solution of $\nabla^2\Psi = 0$ and therefore drops out of the equation. One only has to solve for the regular part.

Eq. (3.29) shows that close to the singularities the term $\tilde{A}_{ab}\tilde{A}^{ab}$ diverges no worse than $|\vec{r}-\vec{r}_\lambda|^{-6}$ and $\mu$ as $|\vec{r}-\vec{r}_\lambda|$. Therefore, $\nu$ vanishes like $|\vec{r}-\vec{r}_\lambda|$ at the singularities. As long as the divergence of $u$ is not worse than $1+O(r^{-1})$, the problem is well posed, and a unique solution exists [46].

This setting simplifies the equation dramatically because the singularity is removed and the solution is therefore regular ($C^2$) and because it can be solved on $R^3 \ \{O\}$ with no inner boundary needed.

### 3.2.4 Problems with These Data

It may seem that with the Bowen- York data, or the puncture data, at hand the initial data problem for two black holes is solved. They both are methods for generating general configurations with arbitrary linear and angular momenta, arbitrary sizes of the black holes etc. However, both solution methods rely on strong assumptions. They both set $K = 0$ and $M_{ab} = 0$, and they both use a flat conformal metric. At least this last assumption is expected to be false in physically realistic data sets. There is no conformally flat slicing of the Kerr spacetime that is axisymmetric and has a smooth limit if the Schwarzschild metric as the spin parameter goes to zero [74]. This means that these methods cannot even generate a single Kerr black hole - the initial

data set will always contain some radiation in addition to the spinning black hole. For a single black hole, this radiation content can be visualized by subtracting the analytic solution from numerical results. As shown for instance in [61], the radiation content is different for different conformally flat data, and dependent on the rotation parameter, but does not drop below 3.8% for Bowen-York data (and 3.5% for the initial data set introduced in [61]). However, for two black holes there is no analytic solution. And this spurious radiation content may completely disturb the form and amount of physical gravitational radiation computed.

It should be noted here that it seems that the choice of the extrinsic curvature is much more important than the choice of the conformal metric. Lousto and Price for instance, could show that in the particle limit of the head-on collision of two black holes (one black hole is seen as a perturbation of the other one), the error due to the choice of conformal flatness is much smaller than the error due to the choice of the extrinsic curvature [86]. This is also supported by Brügmann-Tichy's recent puncture data sequence [114].

The different decompositions mentioned in section 3.2 allow in principle for completely general solutions of the initial data problem. As mentioned before most of the choices are made for mathematical convenience. But quantities as for instance the tensor $M_{ab}$ of the transverse traceless decompositions are difficult to interprete geometrically. Setting them to zero (or anything else) cannot be done on physical grounds, but only for mathematical reasons. This makes it extremely complicate to find astrophysically meaningful data.

Another facet of this problem is that it is quite difficult to compare different initial data sets. In all approaches one can create systems of two black holes orbiting in some path about each other. However, the form of the constraint equations differ, the coordinates differ, the slicings differ etc. So there is no surprise that the solutions differ. The problem arises when trying to rank the differences, or when trying to

quantify them. With no correct solution at hand one cannot quantify the errors and the content of spurious radiation can only be estimated roughly based on asymptotic definitions of masses and momenta. There is no way to account for local differences in the data sets.

## 3.3 Solving the Constraints (II): Thin Sandwich

As described in section 3.2.4, one of the problems of finding astrophysically realistic initial data lies in the lack of geometrical interpretation of the variables used. They are set mainly based on mathematical reasoning rather than physical requirements. One way around this problem is to change the formalism in such a way that the used quantities have physical or geometrical meaning. Such an approach is detailed in this chapter.

Wheeler proposed a "Thin Sandwich" conjecture supposing that two consecutive time slices can be used to determine the full 4 metric [91, 119][2]. York modified the ansatz to work for the conformal decomposition [124].

The idea is to take not only the data on one hypersurface into account but also the transition to the next one. This leads to a fifth equation, stemming from the evolution equation for the metric, as well as requiring the use of the gauge functions (lapse and shift) as the unknowns of the equations.

The approach starts as before with the conformal split of the 3-metric:

$$\gamma_{ab} = \Psi^4 \tilde{\gamma}_{ab}. \tag{3.37}$$

Now one can define

$$u_{ab} \equiv \gamma^{\frac{1}{3}} \partial_t (\gamma^{-\frac{1}{3}} \gamma_{ab}) \tag{3.38}$$

$$\tilde{u}_{ab} \equiv \partial_t \tilde{\gamma}_{ab}. \tag{3.39}$$

[2]There have been counter examples for that [121]

$u_{ab}$ represents the traceless part of the time evolution of the conformal metric. Inserting this into the evolution equation for the three metric (Eq. (2.12)) gives

$$u^{ab} = -2\alpha A^{ab} + (\tilde{L}\beta)^{ab}, \tag{3.40}$$

where $A^{ab}$ is again the traceless part of the extrinsic curvature defined in Eq. (3.3) and $(L\beta)^{ab}$ is the York vector potential (Eq. (3.5)) with now the shift as the vector potential

$$(L\beta)^{ab} = \nabla^a \beta^b + \nabla^b \beta^a - \frac{2}{3}\gamma^{ab}\nabla_c \beta^c \tag{3.41}$$

One of the important features of this treatment is the introduction of a conformally rescaled lapse:

$$\tilde{\alpha} = \Psi^6 \alpha \tag{3.42}$$

Using this and solving Eq. (3.40) for $\tilde{A}^{ab}$ gives

$$\tilde{A}^{ab} = \frac{1}{2\tilde{\alpha}}\left((\tilde{L}\beta)^{ab} - \tilde{u}^{ab}\right), \tag{3.43}$$

the momentum constraint becomes

$$\nabla_b \left[\frac{1}{2\tilde{\alpha}}(L\beta)^{ab}\right] = \nabla_b \left[\frac{1}{2\tilde{\alpha}}u^{ab}\right] + \frac{2}{3}\Psi^6 \nabla^a K, \tag{3.44}$$

and the Hamiltonian constraint

$$8\nabla^c \nabla_c \Psi - R\Psi + A_{ab}A^{ab}\Psi^{-7} - \frac{2}{3}K\Psi^5 = 0. \tag{3.45}$$

To summarize the results: This procedure starts with free data $\gamma_{ab}, u_{ab}, \alpha$, and $K$ and solves Eqs. (3.43), (3.44), and (3.45) for $\Psi, \beta^a$, and $A_{ab}$.

This decomposition is a purely geometrical analysis, and all used terms have meanings that can be interpreted geometrically. Unlike in the former decompositions, where heavy use of mathematical properties was made, and the reductions of the tensors cannot easily be interpreted, here all that is used beside the metric and extrinsic curvature is the shift vector, the (rescaled) lapse function, and the time derivative of the conformal metric.

York, who proposed this decomposition, compared this ansatz with a Lagrangian method in contrast to the transverse traceless decompositions which are closer to a Hamiltonian approach for their use of the canonical variable $K_{ab}$ (which is closely related to the real canonical conjugate of the metric defined in Eq. (2.9).

In a recent paper [98] York and Pfeiffer outlined the connection between this Thin Sandwich decomposition and the transverse traceless decompositions by introducing an arbitrary weight into the latter, and showing that if this weight is taken to be the densitized lapse and the shift of the Thin Sandwich method is taken, the two decomposition agree. Nevertheless, it is only in the Thin Sandwich approach all the ingredients are geometrically motivated.

The Thin Sandwich approach forms the basis of the "quasi-killing-vector" data, outlined in chapter 6.

## 3.4 Other construction methods

None of these decompositions is restricted to use a flat conformal metric. But since the equations simplify so much when using $\gamma_{ab} = \Psi^4 \delta_{ab}$, it is the most widely used choice, even though there is no conformal slicing of the Kerr metric [74].

Alternatives to the conformal flatness assumptions have been proposed. The following sections will report on some of them.

### 3.4.1 Superposed Kerr Schild data

Matzner et al. [87] suggested the following choice of a conformal metric:

$$\gamma_{ab} = \delta_{ab} + 2H^1 l^1_a l^1_b + 2H^2 l^2_a l^2_b \tag{3.46}$$

The idea stems from the Kerr-Schild metric for a single black hole, which has the form $g_{\mu\nu} = \eta_{\mu\nu} + 2Hl_\mu l_\nu$,where $\eta_{\mu\nu}$ denotes the Minkowski metric, H a scalar function of the coordinates, and $l_\mu$ a null vector. It is, depending on $H$ and $l_\mu$, the solution

of a rotating or non rotating black hole. The form of the metric remains unchanged under Lorenz boosts. So it is very easy to construct a very general black hole using this metric.

Based on this form of the single black hole, Matzner et al. constructed a binary black hole system with the spatial part of Eq. (3.46) as the metric. But since it is not a solution of the constraints, one has to go through the York solution procedure, take this metric as a conformal one and solve for the conformal factor.

The Kerr-Schild ansatz could cure the problem of the conformal flatness condition, however, it is not known yet whether it will create less artificial radiation, and it comes at a very high cost: all differential operators now include, via the metric, the singularities of the system. That makes it a mathematically ill conditioned procedure. Neither existence nor uniqueness has been shown.

For the extrinsic curvature, Matzner et al. used a similar ansatz:

$$K_{ab} = K^1_{ab} + K^2_{ab}, \tag{3.47}$$

where the $K^i_{ab}$ are the extrinsic curvatures of the single black holes. The four dimensional metric for one black hole is used to compute the extrinsic curvature for that black hole, and the total extrinsic curvature is the sum of the individual extrinsic curvatures. Diener [65] has taken another approach and used the extrinsic curvature of the 4D metric

$$\gamma_{\mu\nu} = \eta_{\mu\nu} + 2H^1 l^1_\mu l^1_\nu + 2H^2 l^2_\mu l^2_\nu. \tag{3.48}$$

to construct the data. He was able to find a solution using a multi-grid elliptic solver on a two dimensional (cell-centered) grid. As mentioned above, Matzner et al. found a solution using excision. This rid them of the singularities in the operators, but they had to use an additional refinement to make it work. To solve the constraints, they used an "attenuation" function that blended out the other black hole near the first one (and vice versa). So the scalar function $H^1$ is multiplied by a smooth enough

function that is one near the first black hole and zero near the other. $H^2$ is treated analogously around the second black hole. This way they ended up with the following conformal metric:

$$\gamma_{ab} = \delta_{ab} + B^1 H^1 l^1{}_a l^1{}_b + B^2 H^2 l^2{}_a l^2{}_b \tag{3.49}$$

and found a solution for the conformal factor using the Hamiltonian constraint. but as was shown later this solution depends on the size of the excision region, resulting from the ad-hoc choice of the boundary condition [97].

### 3.4.2 Post-Newtonian based data

Another approach is taken by Tichy et al.[115]. They use a metric and extrinsic curvature given by the Post-Newtonian approximation (mentioned in the introduction as an approximate method to solve Einstein's equations) as the conformal objects. (Data of the 2nd Post-Newtonian order were used.) This is a very promising ansatz since the Post-Newtonian approximation is believed to be very accurate (at least for well separated black holes) and physical interpretation of this data is clear.

However, the Post-Newtonian approximation is not solving Einstein's equations. The PN metric was only used as a conformal metric. Still the constraint equations had to be solved. The solution is not Post-Newtonian anymore. Actually the conformal factor (encoding the difference between the PN data and the solution to Einstein's equations) diverges at the singularities introducing large changes to the data. Therefore advantages like interpretability are lost.

A completely new way of constructing initial data, not relying on York's conformal decomposition, is described in the following section.

## 3.5 Nonconformal Data

Based on earlier work [37] that first introduced the nonconformal ansatz using the Kerr-Schild form and solved the equations for a particular perturbation of Schwarzschild,

a new set of initial data was solved within the work for this thesis in collaboration with N. Bishop and F. Beyer. The motivation was to find an ansatz for which a variety of solutions can be constructed as the number of possible solutions turn out to be limited for the ansatz used in [37]. The following ansatz satisfies this condition. It leads to an nonlinear elliptic equation for one unknown, which has been solved for a perturbed Schwarzschild black hole and will in the near future be solved for two black holes.

The idea is to use a modified Kerr-Schild ansatz for the three metric. To simplify the treatment, the first analysis was done with the additional requirements

$$K_{ab} = 0 \qquad \text{and} \qquad R^{(4)} = 0. \tag{3.50}$$

Setting the four dimensional curvature scalar to zero neglects solutions containing matter. Setting $K_{ab}$ to zero (as explained earlier) is done for mathematical convenience. Physically it leads to a time symmetric initial slice, which in turn means that the black holes are momentarily at rest. In a binary black hole case, this corresponds to a head-on collision, and to get astrophysically more realistic data this assumption needs to be relaxed.

The ansatz for the three-metric is:

$$\gamma_{ab} = \frac{\delta_{ab} + 2V k_a k_b}{1 - 2V}, \tag{3.51}$$

with $\delta_{ab}$ being the Euclidian three-metric, $V(r, \theta\phi)$ a scalar field and $k_a$ a vector that is represented in this treatment as the derivative of another scalar field $\phi$:

$$k_a = \frac{\phi_{,a}}{\sqrt{\delta^{ab}\phi_{,a}\phi_{,b}}}. \tag{3.52}$$

Using spherical coordinates and an axisymmetric setting ($x^i = (r, \theta, \varphi)$, $d_{ij} = \mathrm{diag}(1, r^2, r^2 \sin^2\theta)$, and with $V$ and $\Phi$ depending only on $r$ and $\theta$)) one ends up with the following form of the Hamiltonian constraint:

$$c_{20}V_{,rr} \quad + c_{11}V_{,r\theta} + c_{02}V_{,\theta\theta} + c_5 \left(V_{,r}\right)^2 + c_4 V_{,r}V_{,\theta}$$

$$+c_3\left(V_{,\theta}\right)^2 + c_2 V_{,\theta} + c_1 V_{,r} + c_0 V = 0. \tag{3.53}$$

The coefficients are functions of $r$, $\theta$, $V$, $\Phi$ and higher derivatives of $\Phi$. Some of the coefficients are very long expressions, and so here only the coefficients of the principal part are given.

$$c_{20} = -2\frac{(1-2\,V)\ {\Phi_{,\theta}}^2 + 2\,r^2\,{\Phi_{,r}}^2}{(1-2\,V)\ \left({\Phi_{,\theta}}^2 + r^2\,{\Phi_{,r}}^2\right)} \tag{3.54}$$

$$c_{11} = -4\frac{(1+2\,V)\ \Phi_{,\theta}\,\Phi_{,r}}{(1-2\,V)\ \left({\Phi_{,\theta}}^2 + r^2\,{\Phi_{,r}}^2\right)} \tag{3.55}$$

$$c_{02} = -2\frac{2\,{\Phi_{,\theta}}^2 + r^2\ (1-2\,V)\ {\Phi_{,r}}^2}{r^2\ (1-2\,V)\ \left({\Phi_{,\theta}}^2 + r^2\,{\Phi_{,r}}^2\right)} \tag{3.56}$$

The determinant of the principal part is

$$\Delta = c_{20}c_{02} - \frac{1}{4}c_{11}^2 = \frac{8}{r^2\ (1-2\,V(r,\theta))},$$

showing that the equation is elliptic provided $V < 1/2$.

**Analysis**

*Schwarzschild*

The first task was to find an explicit representation of the Schwarzschild geometry that satisfies the ansatz (Eq. (3.51)). This was used later for a number of purposes, including the setting of boundary data in more general situations, and as the zeroth order solution about which a perturbed Schwarzschild solution can be constructed.

Beginning with the Schwarzschild 3-metric in isotropic coordinates $(\bar{r}, \theta, \phi)$, the 3-metric is given by

$$ds^2 = \left(1 + \frac{m}{2\bar{r}}\right)^4 \left(d\bar{r}^2 + \bar{r}^2 d\theta^2 + \bar{r}^2 \sin^2\theta d\varphi^2\right) \tag{3.57}$$

with the extrinsic curvature of the space like initial slice $K_{ij} = 0$ one can obtain the form of Eq. (3.51) by requiring

$$\left(1 + \frac{m}{2\bar{r}}\right)^2 d\bar{r} = dr. \tag{3.58}$$

This is easily integrated to give the coordinate transformation

$$r = \bar{r} + m \ln \frac{2\bar{r}}{m} - \frac{m^2}{4\bar{r}} + \frac{m}{2}, \tag{3.59}$$

where the integration constant has been chosen so that the event horizon is at $r = \bar{r} = m/2$. Then, in $(r, \theta, \varphi)$ coordinates, the metric satisfies ansatz (3.51) with

$$\phi = \frac{1}{r}, \quad V(r) = V_S(r) \equiv \frac{1}{2}\left(1 - \left(1 + \frac{m}{2\bar{r}}\right)^{-4} \frac{r^2}{\bar{r}^2}\right). \tag{3.60}$$

On the event horizon at $r = m/2$ one has

$$V = \frac{15}{32}, \tag{3.61}$$

and one can make an asymptotic expansion to find

$$\lim_{r\to\infty} = \frac{m}{2r}\left(1 - 2\ln\frac{2r}{m}\right). \tag{3.62}$$

*Perturbed Schwarzschild*

The knowledge of the Schwarzschild solution can be used to find a solution of a perturbed Schwarzschild black hole. One can set $\Phi = 1/r$ and use a simple inner boundary condition

$$V\left(r = \frac{1}{2}, \theta\right) = \frac{15}{32} + \epsilon\, P_n(\cos\theta) \tag{3.63}$$

to perturb the black hole where $P_n$ is the $n$-th Legendre polynomial. In principle, the size of $\epsilon$ is only limited by the condition $V < 1/2$ to preserve ellipticity of Eq. (3.53), so

$$|\epsilon| < \frac{1}{32}.$$

As an outer boundary condition $V(r, \theta) \to V_S(r)$ as $r \to \infty$ was set even though it is the true value only at infinity.

Now one can proceed in two ways. The first is to linearize, that is ignore all terms of order $\epsilon^2$ in Eq. (3.53). Doing so, the solution can be written as an infinite sum of eigenfunctions. A second method to is to solve the elliptic problem Eq. (3.53)

numerically, and use the linearized solution as an analytic solution against which the numerical method can be validated. The reason for doing this is that in future work, a reliable numerical method will need to be applied to problems for which an approximate analytic solution cannot be found.

*Linearized Analysis*

If the perturbation introduced in Eq. (3.63) is small enough, i.e. $\epsilon \ll 1$, it is a good approximation to neglect terms of order $\epsilon^2$ and higher. Limits on $\epsilon$ will be given later.

The ansatz

$$\Phi = 1/r, \quad V(r,\theta) = V_S(r) + \epsilon w_n(r) P_n(\cos\theta) \tag{3.64}$$

separates the linearized Hamiltonian constraint, and one is left with an ordinary differential equation for $w_n(r)$

$$d_1 w_n''(r) + d_2 w_n'(r) + d_{3(n)} w_n(r) = 0 \tag{3.65}$$

with the coefficients

$$\begin{aligned}
d_1 &= r^2 \left(-1 + 2\,V_S(r)\right)^2 && (3.66)\\
d_2 &= -r\,\left(-1 + 2\,V_S(r)\right)\,\left(3 - 6\,V_S(r) + 7\,r\,V_S'(r)\right) && (3.67)\\
d_{3(n)} &= 1 - \frac{n(n+1)}{2} + \left(3n(n+1) - 8\right)\,V_S(r) && (3.68)\\
&\quad -2\,\left(3n(n+1) - 10\right)\,V_S(r)^2 && (3.69)\\
&\quad +4\,\left(n(n+1) - 4\right)\,V_S(r)^3 + 7\,r^2\,V_S'(r)^2. && (3.70)
\end{aligned}$$

The fact, that the Schwarzschild solution $V_S(r)$ (Eq. (3.60)) is itself a solution of the Hamiltonian constraint, has been used. Now one can define the functions $w_n(r)$ to be those solutions of Eq. (3.65) which satisfy the boundary conditions

$$w_n(r = \frac{1}{2}) = 1, \quad w_n(r \to \infty) = 0. \tag{3.71}$$

Of course, a general solution to the perturbed Schwarzschild problem can be constructed by summing the eigenfunctions, i.e.

$$V(r,\theta) = V_S(r) + \epsilon \sum_{n=1}^{\infty} a_n w_n(r) P_n(\cos\theta) \tag{3.72}$$

where the $a_n$ are arbitrary constants.

In order to show that the 3-metric defined by Eq. (3.64) is not conformally flat, one needs to prove that the Cotton-York tensor [95, 117]

$$Y_{ijk} = R_{ij;k} - R_{ik;j} + \frac{1}{4}(R_{,j} g_{ik} - R_{,k} g_{ij}), \tag{3.73}$$

does not vanish identically. If only the first eigenfunction is present (i.e., if $n = 1$) then the York tensor is zero to first order in $\epsilon$; but, for example,

$$Y_{112} = \epsilon \frac{2 - n(n+1)}{4\, r^2} w_n(r) P_n'(\cos\theta).$$

So it is proven that the eigenfunctions with $n > 1$ do not represent a conformally flat geometry.

*Numerical Method*

The second proposal was to solve Eq. (3.53), subject to the boundary condition defined by Eq. (3.63) and

$$V(r,\theta)|_{r=r_{OB}} = V_S(r)$$

using $V_S(r)$ given by Eq. (3.60), with a standard numerical elliptic solver.

Due to the symmetry of the problem, one can impose the additional boundary conditions

$$\left.\frac{\partial V}{\partial n}\right|_{\theta=0,\pi} = 0$$

where $n$ is a vector normal to the $\theta = 0, \pi$-surfaces. For simplicity these conditions were implemented at $\theta = 0+\eta, \pi-\eta$ with $\eta \ll 1$ and of the order of magnitude of the accuracy up to which Eq. (3.53) is to be solved. This is a common procedure to avoid

numerical problems at the singular points of the equation ($\theta = 0, \pi$) -for example, the same situation arises in the case of the Laplace equation in spherical coordinates.

To solve non-linear elliptic PDEs, the standard Jacobi method was used. For a successful solve, the choice of the initial guess for $V(r, \theta)$ is crucial. It turns out to be sufficient to use Eq. (3.60) plus a Legendre perturbation of a given order $n$ with linearly decreasing amplitude from the inner to the outer boundary consistent with the boundary conditions above. To compute $V_S(r)$ for the initial guess numerically, Eq. (3.59) was solved for $\bar{r}$ by a numerical integration of Eq. (3.58) which was then substituted into Eq. (3.60) - the problem being that Eq. (3.59) is explicit in the wrong direction.

The computations were done using the Cactus Computational Toolkit and the TAT-Jacobi elliptic solver [111], which uses the standard Jacobi solution method and the boundary conditions were implemented using second order finite differencing.

The convergence of the method is very slow, mainly due to non-linear terms in Eq. (3.53) which are dominant close to the horizon. So in a first run of the elliptic solver the residual was multiplied by $(1 - 2V)$, which is small near the horizon. This gives the solver the opportunity to get an accurate solution everywhere else before, in a second run, the original equation was solved. By means of this technique the convergence speed was significantly increased.

**Results**

As a start the simplest non conformally flat case was solved numerically: a perturbation with a $n = 2$ Legendre polynomial. The outer boundary was set to $r_{OB} = 10$ and the amplitude to $\epsilon = 0.005$. The code was shown to exhibit second order convergence (compare table (3.1)). However, it was also shown that the solution of the linearized equation is not the limit of the convergence sequence for infinite resolution. To understand why this is the case the higher terms of the expansion were investigated. It

| height | $N_r$ | $N_\theta$ | $\Delta_r$ | $\Delta_\theta$ | final resid. of Eq.(3.53) |
|---|---|---|---|---|---|
| low | 97 | 33 | 0.098 | 0.095 | $4.0 \cdot 10^{-7}$ |
| medium | 193 | 65 | 0.049 | 0.048 | $1.0 \cdot 10^{-7}$ |
| high | 385 | 129 | 0.025 | 0.024 | $2.5 \cdot 10^{-8}$ |

Table 3.1: Results of convergence test of nonconformal data.

turned out that close to the horizon they become large. The solution of the linearized Hamiltonian constraint Eq. (3.65) was substituted into the full constraint Eq. (3.53) and plotted in Fig. (3.5). Additionally, the plot shows the residual for the case that $\epsilon$ is smaller by a factor of 10 ($\epsilon = 0.0005$). Although the linearized solution is not accurate close to the boundaries for $\epsilon = 0.005$, the residual shows the right quadratic scaling for decreasing $\epsilon$ due to second order terms. This gives us a measure of how small $\epsilon$ should be in order to obtain a desired accuracy. The same computations were repeated for different positions of the boundaries and different $n$ recovering convergence as before. Fig. (3.6) shows the linearized solutions – i.e. full solutions provided $\epsilon$ is small enough – for different $n$.

## 3.6 Summary

This chapter described the most important methods to solve the constraint equations. It introduced the York procedure, Bowen-York data, Misner data, and Puncture data. It explained some of the problems these data have (especially mentioning the problem of interpretation of the used variables), and introduced the Thin Sandwich data. The Thin Sandwich data are geometrically motivated and all used variables have a geometrical interpretation.

A new method presented in this section represents a completely new way of finding

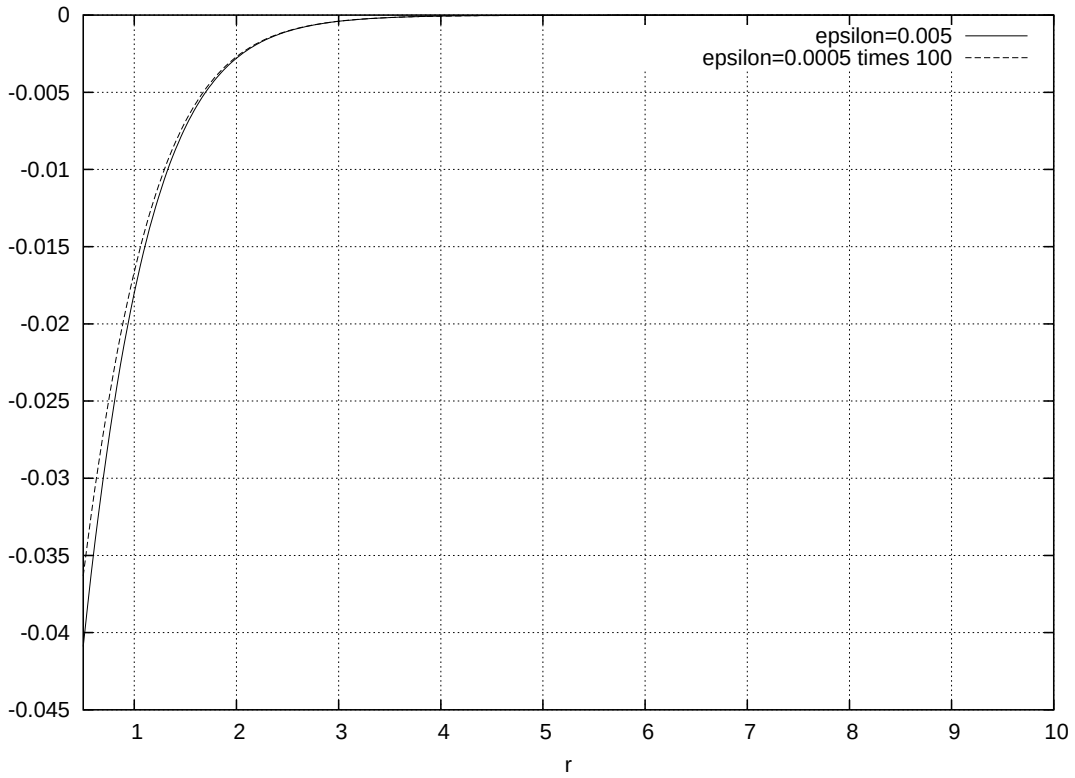


Figure 3.5: Residuum of Eq. (3.53) for the linearized solution. The rescaled fine resolution line matches almost perfectly. Even though the residuum becomes larger close to the boundary, the error converges away with second order.

initial data for Einstein's equations. Since it is not based on a conformal decomposition it is by construction different from everything build to date. This method provides data that are genuinely different (not conformally flat) from the previously described ones. It was shown that with this construction it is possible to construct a non-conformally flat perturbation of the Schwarzschild solution. This numerically found solution could be compared with a linearized solution and it was shown to agree to a high degree.

The idea how to construct binary black holes with this method was explained as well. Preliminary tests have shown that this method works. But to make use of this new ansatz a lot of work remains to be done. The boundary condition at the

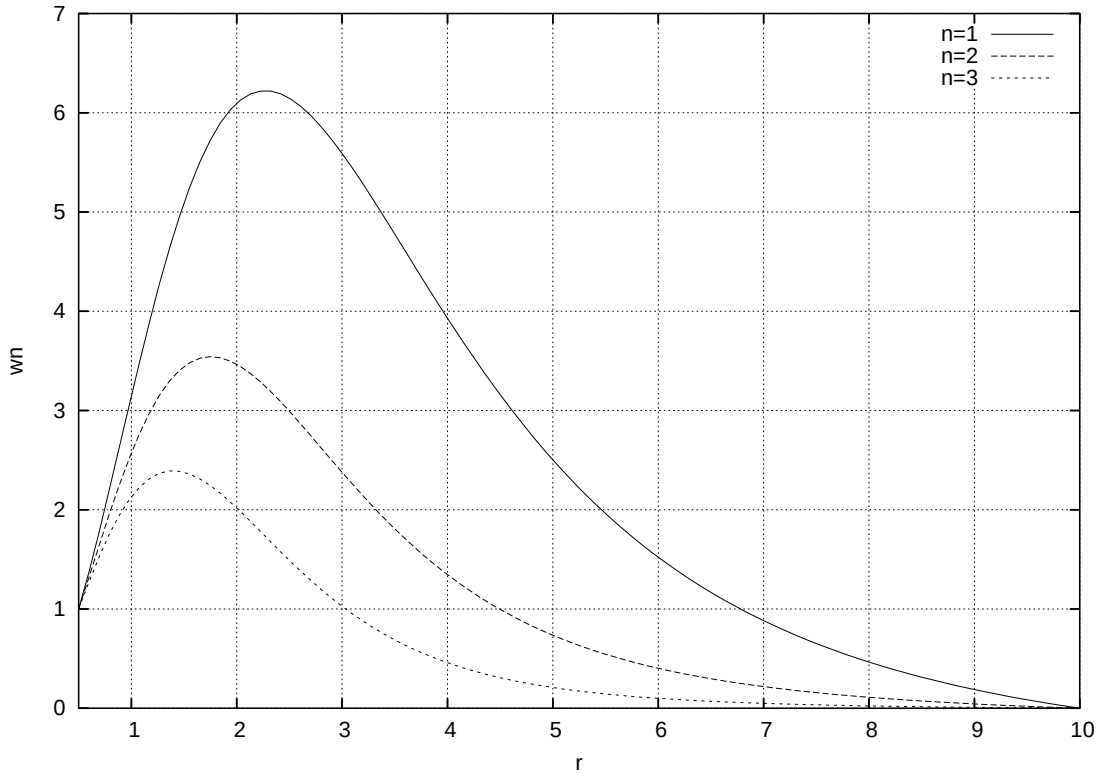


Figure 3.6: Linearized solutions for different $n$

symmetry plane between the two holes is very complicate to implement. Especially since it includes a point where the scalar field $V$ vanishes. This creates a coordinate singularity that has to be dealt with. As a major aim there stands, of course, methods for the creation of initial data for the binary black hole problem.

The remainder of this thesis concentrates on Puncture and Thin Sandwich data.

# Chapter 4

# Methodology

Before coming to physical problems, this chapter as an interlude explains briefly some details of the numerical treatment of the initial data problem. There are many complications, pitfalls and possible errors when using numerical methods, but as mentioned above Einstein's equations are by far too complicate to be solved in general analytically. Additionally the physical quantities are explained that will be needed in the following chapters including a geodesic distance measurement developed and implemented for this thesis.

## 4.1 Finite Differencing

The basic method to solve the various differential equations appearing when solving Einstein's equations numerically is called finite differencing. Here a differentiation is approximated by a finite difference. This can be seen best looking at the Taylor expansion of a function at a point that is only a small distance ($h$) away from the point x:

$$u(x+h) = u(x) + \frac{1}{1!}hu'(x) + \frac{1}{2!}h^2u''(x) + \frac{1}{3!}h^3u'''(x) + \dots \tag{4.1}$$

Cutting this series at the first order and solving for $u'(x)$ one gets

$$u'(x) = \frac{u(x+h) - u(x)}{h} + O(h). \tag{4.2}$$

To get a higher order approximation one can write down the Taylor series for a point

"left" of x

$$u(x-h) = u(x) - \frac{1}{1!}hu'(x) + \frac{1}{2!}h^2u''(x) - \frac{1}{3!}h^3u'''(x) + \ldots, \tag{4.3}$$

subtract it from Eq. (4.2), and cut the series at third order. One gets

$$u'(x) = \frac{1}{2h}\left(u(x+h) - u(x-h)\right) + \emptyset(h^2). \tag{4.4}$$

To get the second derivative one can add Eqs. (4.3) and (4.4), omit terms of order $h^4$ or higher and get

$$u''(x) = \frac{1}{h^2}\left(u(x+h) - 2u(x) + u(x-h)\right) + \emptyset(h^2). \tag{4.5}$$

Another way to solve differential equations uses the so-called spectral methods. Here the solution (say $u$) is expanded into a series of known functions $f_k$ (modern versions usually use Chebychev polynomials):

$$u = \sum_{k=0}^{\infty} a_k f_k. \tag{4.6}$$

Inserting this into the differential equation $L(u) = 0$ will turn it into an equation for the $a_k$:

$$L(u) = 0 \tag{4.7}$$

$$L(\sum_{k=0}^{\infty} a_k f_k) = 0 \tag{4.8}$$

$$a_k \sum_{k=0}^{\infty} L(f_k) = 0. \tag{4.9}$$

With these $a_k$ the original equations is solved at the so-called collocation points. It can be shown that the error between these points will decrease with the number of points exponentially if $u$ is $C^\infty$.

## 4.2 Numerical Error Estimates

### 4.2.1 Convergence

The previous section shows the immediate problem numerical methods always have: they are approximations. The results of the numerical treatment of the equations, $u$

will in general differ from the analytic solutions $\bar{u}$ (which are unknown). The error, $e$, will depend on the resolution of the numerical treatment. To ensure that numerics does the right thing it is necessary that the error will converge to zero when the resolution $n$ (interpreted as number of points per interval) will become infinite. In the work for this paper all codes (especially the Cactus code) are made to converge at least to second order in $n$. This means that a function $\bar{u}$ being a solution to a differential equation is approximated by a function $u_n$, which is a solution of the finite differenced version of the same differential equation. The error $e(n)$ is assumed to depend on the resolution such that one can write:

$$\begin{aligned} \bar{u} &= u_n + e(n) \\ \bar{u} &= u_{2n} + \frac{1}{4}e(n) \\ \bar{u} &= u_{4n} + \frac{1}{16}e(n) \\ &\dots \\ \bar{u} &= u_{kn} + \frac{1}{k^2}e(n). \end{aligned} \tag{4.10}$$

A "convergence test" can be carried out by testing only three of these equations. One can, for instance, compute the convergence factor $\eta$ defined by:

$$\eta = ln\left(\frac{u_{coarse} - u_{medium}}{u_{medium} - u_{fine}} - \chi\right). \tag{4.11}$$

This gives the value of the convergence exponent (which was assumed to be two in Eq. (4.10)). Let $u_{fine}$ be a numerical solution to a finite difference equation with the resolution $fine$, $u_{medium}$ the solution of the same equation taken with a resolution of $medium = \chi \times fine$,and finally $u_{coarse}$ the solution of the equation with the resolution $coarse = \chi \times medium$. Then $\eta$ as defined by Eq. (4.11) will give the rate of convergence of the solution scheme and/or the implementation. It provides a very good check for the quality and validity of an implementation.

### 4.2.2 Constraints

Even if the numerical errors will converge away, they can ignite other errors that can grow and eventually make the code crash. One important example is the constraint equations. As said above, analytically the Bianchi identities ensure that a solution of the constraints is a solution of the evolution equations. However, a small error will not necessarily remain small after some evolution. In general it will grow. Even strongly hyperbolic systems allow exponential growth of errors.

Intensive research is underway on how eliminate such growth. One possibility is to try to change the equations in order to make the constraint surface (the surface in super-space of all possible 3d-metrics and extrinsic curvatures on which the constraints are solved) an attractor. Of course Einstein's equations can only be changed by terms that are zero analytically, otherwise one would change the theory. One can for instance add multiples of the constraints to the evolution equations. These change the principle part, which can influence growing modes. There has been a detailed investigation [106, 107] on what term would have what behavior on the equations. However, these investigations have been done using the linearized version of Einstein's equations. To make this useful for real numerical relativity, many tests are necessary. Many such tests are undertaken now in the community and at a meeting in Mexico a minimal set of tests was proposed [9].

All evolutions done for this thesis are "free evolutions". The constraints are not enforced. This makes them a good measure of the accuracy of solutions- if the constraints are significantly non-zero then the simulations are no longer solutions of Einstein's equations.

## 4.3 Elliptic Solvers

Another issue that often arises when doing numerical relativity is the solution of elliptic solvers. Not only are the constraint equations elliptic but as described above, gauges can also lead to elliptic equations, eg. the maximal slicing or the Γ-freezing shift.

Whereas hyperbolic equations are solutions to initial boundary value problems, involving propagation of data with finite velocities, elliptic equations must be solved instantaneously over an entire slice so that boundary conditions become crucial. Solving all elliptic equations requires expensive iterative relaxation methods. One starts from an initial guess that will be changed in direction of the analytic solution. This method will - depending on the actual implementation - converge sooner or later to a value that with increasing resolution converges to the analytic value. But practical methods tend to slow down dramatically with an increasing number of grid points.

To speed up the process, a multi-grid method has been introduced. It was noticed before that high frequency parts of solutions settled very quickly to a solution whereas lower frequencies modes did so very slowly. Coarsening the grid will effectively raise the frequency of the modes speeding up the convergence of the low frequency modes. This, by interpolating back to the finer grid, gives a much faster convergence to the solution, especially when the number of grid points is very high.

The elliptic solver used for the work for this paper (except for the non conformal data that will be introduced later) is a multi-grid solver called BAM ("Bifunctional Adaptive Mesh" [48]), written by Bernd Brügmann. It uses regular iterative methods (like Gauss-Seidel or the like) to solve the equations on each grid.

## 4.4 Boundary Conditions

### 4.4.1 Outer Boundary Condition

A problem of the treatment of Einstein's equations with finite differences is that the domain one can compute on is finite. This introduces a boundary at the edge of the grid. Looking at Eq. (4.5) for instance one sees that if $x$ is a boundary point the point $x + h$ does not exist. One has to use some value instead. The question what value to use is under constant research because firstly it is far too complicate to be solved rigorously but secondly it is very important because any error introduced at the boundary will travel inwards and disturb the evolution.

One possibility to find a boundary condition is to idealize the system and assume that the boundary is put very far out, where the spacetime can be approximated very well with flat space carrying spherical waves. These waves should then travel freely and leave the grid unreflected. Assuming a fall-off of $1/r$ and not allowing waves to enter the grid one can impose the following outgoing radiation (Sommerfeld) boundary condition:

$$f = f_0 + u(r - vt)/r, \tag{4.12}$$

where $f_0$ is the asymptotic value of a given dynamical variable (typically 1 for the lapse and diagonal metric components, and zero for everything else), and $v$ is a wave speed. This speed can be safely assumed to be the speed of light, $v = 1$, for all the dynamical variables. However, the gauge variables can easily propagate with a different speed implying a different value of $v$.

In the evolutions done for this thesis, the boundary condition Eq. (4.12) was not use as it stands, but rather in its differential form:

$$\partial_t f + v\partial_r f + v\,(f - f_0)/r = 0, \tag{4.13}$$

which is than finite differenced to second order in both space and time and applied to

all dynamic variables (with possible different values of $f_0$ and $v$) at all outer boundaries. Although this equation is for scalars it is applied to all functions regardless of some being tensor components. Also this boundary condition is violating the constraints which leads to first order errors that eventually contaminate the grid. To reduce the problem the boundaries are moved as far into the linear regime as possible.

### 4.4.2 Inner Boundary Condition

One of the great problems when dealing with black holes numerically is the presence of singularities. As mentioned above one way to avoid them is to use singularity avoiding slices, such as the maximal slices (with vanishing mean curvature). Another is by excision. It is conjectured that every singularity is surrounded by an event horizon inside which spacetime is causally disconnected from the exterior [96]. So in principle it would have no influence on the evolutions if the interior was just cut away. This means in practice to place a boundary somewhere inside the horizon, which in turn creates the problem of choosing a correct boundary condition. One could naively think that the boundary does not matter because it is inside the event horizon and therefore causally disconnected. This is true, however, not every boundary condition will lead to a numerically stable evolution. Some problems produce gauge modes, which can travel faster than light. It should be noted that though the physical light cone may be causally disconnected from the exterior, the numerical light cone may still escape the horizon.

Following an idea by Unruh Thornburg was the first to implement such a method in 1 dimension and Seidel et al. [104] made use of this scheme in numerical evolutions.

In all the evolutions done for this thesis a simple excision method was used [6]. That is:

- Safely inside the horizon a “Lego sphere” is excised, a sphere approximated

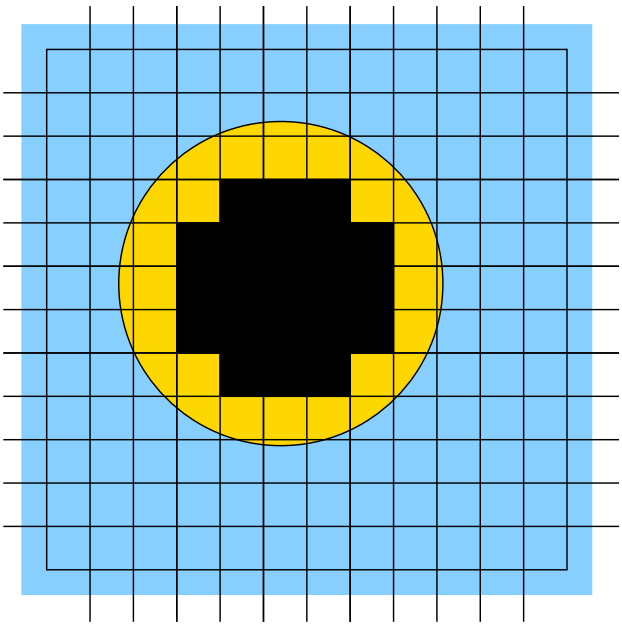

Figure 4.1: Lego sphere. The horizon surface is approximated by a sphere along the grid lines.

along grid lines. This actually generalizes [6], where a cube was excised.

- A simple boundary condition is used at the sides of the cube: time derivatives are copied from their value one grid-point out along the normal direction.

- Centered finite differencing is used (ignoring the causal structure).

This simple technique worked extremely well in all studied cases.

## 4.5 Measurement of Physical Quantities

This section describes the quantities that are to be extracted during initial data computations as well as during the long evolution runs. The following list is by far not complete, it merely explains the quantities used in this paper. Other things may also be interesting, as for instance waves, but could not be accurately extracted for the given runs and thus are not mentioned here.

### 4.5.1 Masses and Momenta

The first quantity to measure is certainly the mass of the system. This is important not only by itself (what mass has the system that is described?) but also as a significant measure of how accurate the evolutions are and how much energy has left the computational grid through radiation. However, in General Relativity there is no local definition of mass. One can only define a global quantity, as was done already in the original ADM paper [25]:

$$M_{ADM} = \frac{1}{16\pi} \lim_{r\to\infty} \oint g^{ij} g^{mn} (g_{in,j} - g_{ij,n}) \sqrt{g} dS_m. \tag{4.14}$$

However, the mass defined that way is given at spatial infinity. But due to computational limits and the methods used here, it has to be calculated at a finite radius and the calculation by the above definition of the ADM mass converges very slowly with increasing $r$. Note that technically $M_{ADM}$ should not change with time.

Ó Murchadha and York in [94] modified this expression using the variables in York's conformal decomposition method. For a conformal metric which falls off fast enough with a radius, their expression for the ADM mass is

$$M_Y = -\frac{1}{2\pi} \oint_\infty D_i \psi dS^i, \tag{4.15}$$

with $\Psi$ being the conformal factor. Eqs. (4.14) and (4.15) are equivalent in the limit of infinite radius. But it turns out that for a Schwarzschild black hole in isotropic coordinates, Eq. (4.15) gives the correct mass already at a finite radius.

Another way of calculating the mass is the so-called Schwarzschild mass. To define it one assumes that beyond some radius the spacetime approximates the Schwarzschild solution. This mass is obtained by first finding the physical (Schwarzschild) radius $R$ of a coordinate sphere, and then finding the correspondent metric component $g_{rr}$ which is the average over the coordinate sphere. The mass is then defined by:

$$M_S = \frac{r}{2}(1 - \frac{1}{g_{rr}}), \tag{4.16}$$

which converges very rapidly with increasing $r$.

Yet another way of defining the mass was defined by Komar [83]. Trying to assign a senseful conserved quantity to every infinitesimal coordinate transformation $\xi^i$ and requiring this quantity to be generally covariant he defined an energy flux vector

$$P^i(\xi) = 2(\xi^{i;l} - \xi^{l;i})_{;l}. \tag{4.17}$$

This vector satisfies the covariant conservation law

$$P^m_{\ ;m} = 0 \tag{4.18}$$

and thereby assures the conservation of the total energy

$$P(\xi) = \frac{1}{2\kappa} \int P^m ds_m. \tag{4.19}$$

For a system that is asymptotically Schwarzschild at spatial infinity it turns out that the energy measured at infinity is

$$M_K \equiv P(\delta^i_4) = Mc^2. \tag{4.20}$$

A useful property of this mass is that it agrees with the ADM mass if and only if the spacetime is stationary and asymptotically flat and the killing vector is orthogonal to the slice [35], which gives a principle to find (quasi) circular orbits as will be discussed in section 6.2.3.

For this paper the ADM mass was calculated according to Eq. (4.14) because the other mass definitions are not always applicable. However, due to the slow convergence a special treatment was used: The ADM mass as defined by Eq. (4.14) was computed at several finite radii. A polynomial was fit and this polynomial was used to extrapolate the value at infinity. This was done using a second order polynomial in the case of the ADM mass, and a third order polynomial in the case of the ADM angular momentum. This procedure is very accurate as was shown in [93] and results can be seen in Fig. (4.2). Plotted are 2nd and 3rd order polynomial fits for the ADM

mass of a Kerr black hole and 3rd and 4th order polynomial fits of the ADM angular momentum. These plots demonstrate that in the mass case a second order polynomial fits the numerical values just as good as a third order one. In the case of the angular momentum the difference between second and third order extrapolations is about 1% but a 4th order polynomial did not change the results significantly. Therefore for the extraction of the ADM mass a second order polynomial (Eq. (4.21)) was used and a third order polynomial (Eq. (4.22)) was used for the ADM angular momentum.

$$A_0 + A_1 \frac{1}{r^2} + A_2 \frac{1}{r^2} = 0 \tag{4.21}$$

$$A_0 + A_1 \frac{1}{r^2} + A_2 \frac{1}{r^2} + A_3 \frac{1}{r^3} = 0. \tag{4.22}$$

For systems of rotating or binary black holes it is natural to ask for the angular momentum. Using the spirit of the ADM mass definition one can create a definition of a momentum depending on a killing vector:

$$\Pi^i \xi^i_{(k)} = \frac{1}{8\pi} \oint_\infty (K^j_i - \delta^j_i K) \xi^i_{(k)} d^2 S_j. \tag{4.23}$$

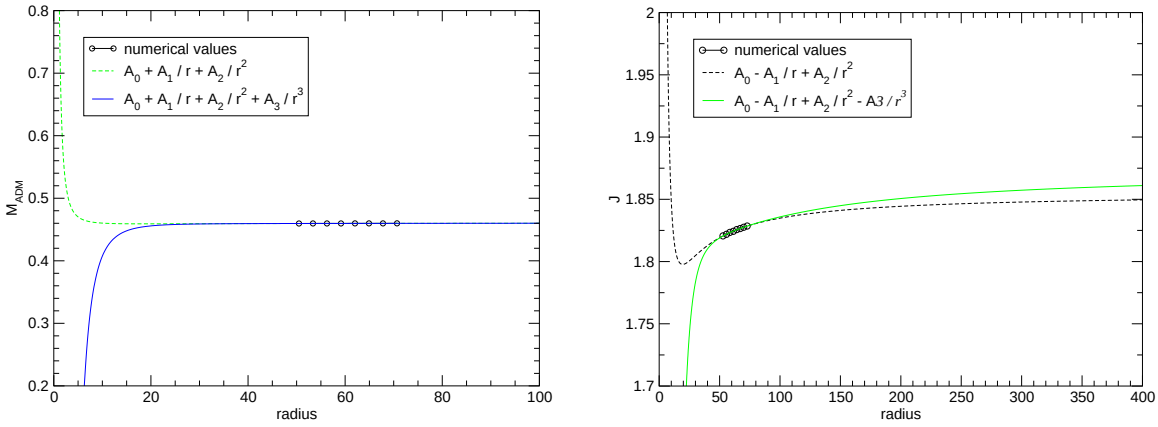


Figure 4.2: Approximations of ADM Mass (left) and angular momentum (right) by second order and third order polynomials, respectively. The values are measured at several radii and extrapolated using the listed polynomials.

If the vector $\xi$ is a translational killing vector the momentum is the linear momentum of the system. In case $\xi$ is rotational, this defines the angular momentum.

Again, since the ADM momenta are defined at infinity, the method of fitting a polynomial was applied. As mentioned above due to the faster falloff of the extrinsic curvature used to compute the momenta a third order polynomial had to be used (compare again Fig. (4.2)).

### 4.5.2 Horizons

The presence of a horizon defines the location of a black hole. There are two different notions of horizons one has to acknowledge. There is of course the event horizon, the closed surface surrounding a singularity (assuming cosmic censorship holds) from within which no light ray will escape to infinity nor will it hit the singularity. However, this idea is a global one. Only at null infinity can one tell whether light has arrived. On a numerical grid (and without the use of conformal rescaling methods) there is no way to reach infinity (neither temporal nor spatial). Additionally one would have to know the entire future solution of the spacetime to tell whether a given light ray will reach infinity. Therefore the finding of event horizons can only be done approximately and only after the entire numerical evolution has finished. Several approaches have been made to find an event horizon numerically. But the approach of [19] turned out to be the most efficient. The idea was to use the full numerical evolution and evolve outgoing null geodesics backwards in time (turning them to ingoing geodesics). For these null geodesics the event horizon is an attractor such that they converge exponentially and track the event horizon very accurately. Very recently Diener [64] implemented a procedure generalizing this idea to 3d. Using the apparent horizon as initial guess he could produce very accurate results already.

Another idea is to use a local quantity, one that can be computed at every timeslice while the simulation is going on. This is quite important for numerical purposes since

a number of tools rely on the location of the horizon, as for instance the excision technique. Given a timeslice, one can define a "marginally trapped surface", a two-surface whose outward pointing normal vectors $n^b$ have zero expansion. Using the usual 3+1 quantities given at the slice the expansion $\Theta$ can be computed as:

$$\Theta := \nabla_b n^b + K_{ab} n^a n^b - K. \tag{4.24}$$

An "apparent horizon" (AH) now is defined as the outermost marginally trapped surface. The surface at which all light cones point inwards. There can be several different trapped surfaces nested inside each other. It is proven [80] that an apparent horizon is always contained inside an event horizon and that they agree if and only if the spacetime is stationary. Thus it is safe to excise inside an apparent horizon, as one is always excising inside an event horizon which is causally disconnected from the outside.

Eq. (4.24) is an elliptic equation. Until very recently the *Cactus* toolkit had two 3D AH finder algorithms, one being a minimization algorithm [84, 21, 52, 5] and other one a curvature flow algorithm [5, 92, 82, 79]. Both of these start from a big sphere floating inwards to settle at a solution of Eq. (4.24). This usually takes very long, that long actually that it was not practical to use at every time step. Within the preparation of this paper, a new horizon finder was implemented [112]. This is using a method directly solving the elliptic equation. Starting with a good initial guess this method is very much faster, allowing for a use at every time step. This was crucial for example for the use in the Meudon data evolutions that heavily depend on tracking the horizon surfaces closely.

Quite a number of physically interesting quantities can be extracted from apparent horizons. First there is the irreducible mass. The area of a Schwarzschild black hole's event horizon $A_{EH}$ is a monotonic function of its mass. The irreducible mass can be

defined as a function of the area [53, 54]:

$$M_{irr} = \sqrt{\frac{A_{EH}}{16\pi}}. \tag{4.25}$$

By analogy one usually defines an apparent horizon mass:

$$M_{AH} = \sqrt{\frac{A_{AH}}{16\pi}} \tag{4.26}$$

and to include rotation this is generalized to:

$$M_{AH}^2 = \frac{A_{AH}}{16\pi} + \frac{4\pi J^2}{A_{AH}}, \tag{4.27}$$

where $J$ is the total angular momentum. This latter expression is sometimes referred to as the Christodoulou mass [53].

With Hawking's area theorem (the area of a black hole cannot decrease), also called second law of black hole thermodynamics, it is understood that this mass is the minimum that will not decrease with time. It is therefore possible to define a maximum radiation content ($MRC$) of a spacetime. This is the difference of the total energy a spacetime contains (as measured by the ADM mass) and the irreducible mass, normalized to the ADM mass:

$$MRC = \frac{M_{ADM} - M_{irr}}{M_{ADM}}. \tag{4.28}$$

The total energy radiated away during an evolution cannot be larger than this number.

Another number that is important and can be extracted from the apparent horizon is the ratio of two different circumferences. For a rotating system it is possible to define an equatorial circumference $c_e$ of a black hole and a polar circumference $c_p$ (One can actually compute two polar circumferences, one with $\phi = 0$ and another one with $\phi = \pi/2$. This way one can also compare the distortion of the holes along due to other influences as for instance a second black hole.). To do so one introduces coordinates $\bar{x}^i = (\theta, \phi)$ on the apparent horizon surface and defines an induced two dimensional metric $g_{ij}$ via

$$g_{ij} = \gamma_{ab} \frac{\partial x^a}{\partial \bar{x}^i} \frac{\partial x^b}{\partial \bar{x}^j} \tag{4.29}$$

Using this metric one can than define the area of the horizon by setting

$$A_{AH} = \int \sqrt{g} d\bar{x}^i d\bar{x}^j \tag{4.30}$$

and the circumferences by

$$c_{p1} = \int_{\phi=0} \sqrt{g_{ij}\bar{x}^i\bar{x}^j} \tag{4.31}$$

$$c_{p2} = \int_{\phi=\pi/2} \sqrt{g_{ij}\bar{x}^i\bar{x}^j} \tag{4.32}$$

$$c_e = \int_{\theta=\pi/2} \sqrt{g_{ij}\bar{x}^i\bar{x}^j}. \tag{4.33}$$

The area definition can be used to compute the masses mentioned in Eqs. (4.26) and (4.27).

In the non-rotating (Schwarzschild) case these agree and for growing rotation they separate increasingly. From their (normalized) ratio one can estimate the degree of rotation. Moreover, as was seen in many cases and is assumed to be always true, for distorted black holes this ratio oscillates with the quasi-normal frequency of the black hole obviously giving insight into real physical processes [19].

### 4.5.3 Horizon Distances

Many papers on initial data rely on one or another notion of distances of the black holes. For evolutionary sequences it is necessary to talk of some distance that becomes smaller as the data evolve. However, as is well known an unambiguous notion of a distance does not exist. Usually what is taken as the physical distance between two black holes is the separation of the horizons along a straight line connecting the two singularities. Such a line need not to be a geodesic. So it could well be too long a line.

A distance measurement which measures along a geodesic was implemented that shoots a particle from the center of symmetry into one of the holes and computes the length of this geodesic from beginning until it hits the horizon (the metric is taken to

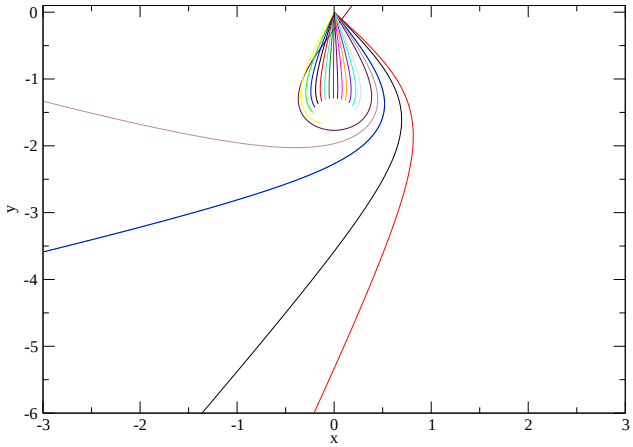


Figure 4.3: Distance measurement. From the center of symmetry (in this case the origin) geodesics are shot into the black hole. The plot shows only the geodesics shot at one black hole. When they hit the computation is stopped. Due to symmetry there is another black hole above the picture. Some geodesics hit the black hole, others miss it and leave the grid. The length of the shortest geodesic hitting the black hole is taken as (half) the separation of the black holes.

be constant in time, such that in effect a geodesic of the 3 metric is found). This is repeated in different directions and the length of the shortest one is used. (To spare some time in practice a shot is stopped if the particle would take longer than the minimum already found.) Fig. (4.4) shows such a measurement. The zoom on the right side shows that the actual minimum is very close to the angle $\pi$ which in this configuration (head on collision) is a shot straight into the hole.

However, using an initial data set that has angular momentum one gets a different picture. Fig. (4.5) shows a similar measurement for a puncture data set with the momentum parameter set to $P = 0.5$. As can be seen clearly the minimum is at 3.19 not at $\pi$.

This shows that the distance measurement can be made much more accurate by using this method. It also indicates that earlier attempts to construct evolutionary sequences by creating several circular orbits with varying distances also include errors. The Cook sequences, for instance, finds the momentum of the black holes based on

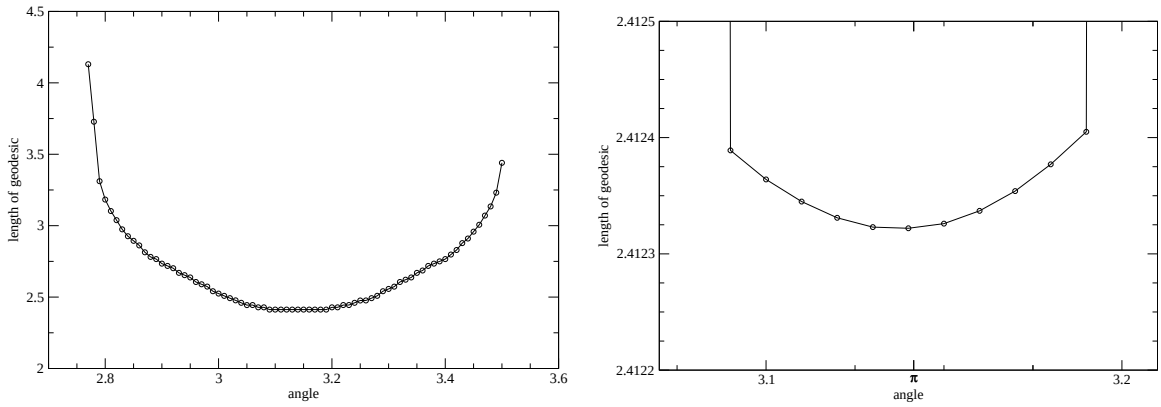


Figure 4.4: Distance measurement of Puncture data in head-on collision: the lengths of geodesics hitting the black hole vs. the angle they were shot at. The lengths are measured and the shortest one is taken as the distance. In this configuration the shortest geodesic was shot at angle $\pi$, which is straight into the black hole.

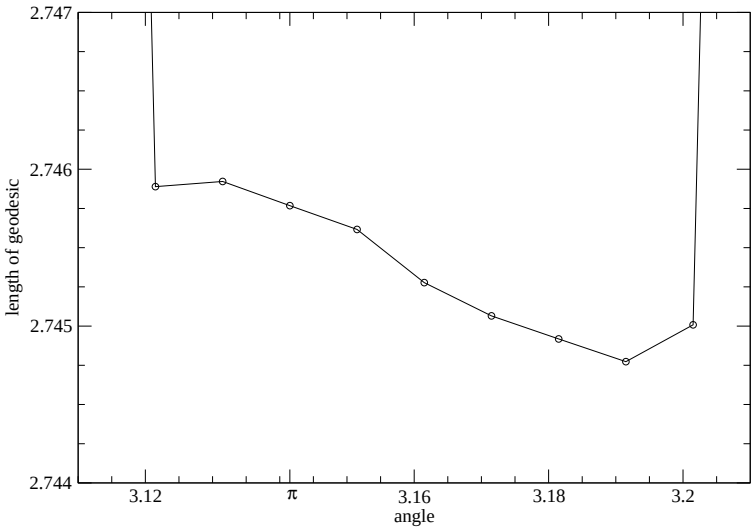


Figure 4.5: Distance measurement of puncture data with $P = 0.5$. The minimum is not at $\pi$. Here a straight line measurement would have an error.

their separation. If the separation is too large the used momentum will be too small leading to an initial data set that is not in circular orbit but rather on its way to plunge. This behavior will decrease with growing separation because the momentum will decrease and the straight line measurement gives the same results as the geodesics measure. This is in agreement with a recently published result [50].

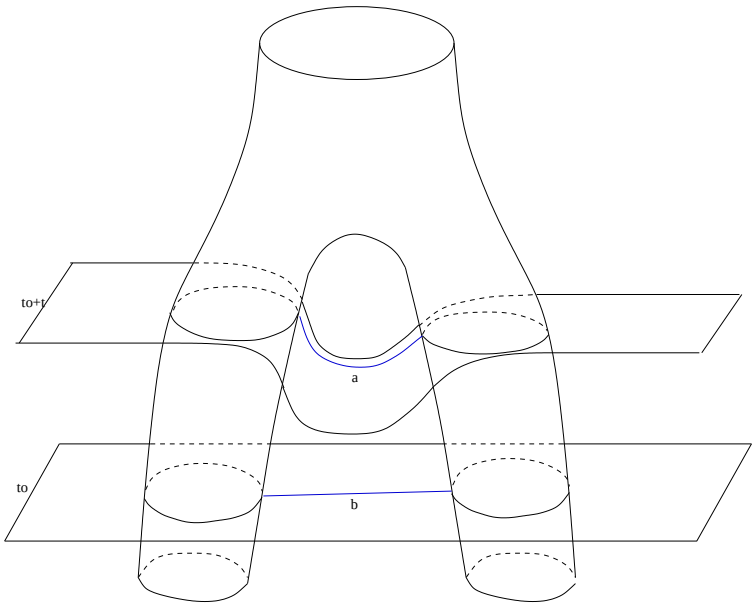


Figure 4.6: Distance measurement. Black holes in slice "b" have a smaller measured distance than in slice a even though slice "a" is taken at a later time and the black holes are farther apart.

Using this geodesic measurement one obtains a somewhat better notion of distance. However, as shown in Fig. (4.6), one can easily imagine a situation where even such a measure leads to a completely wrong interpretation: slicing the same spacetime of two orbiting black holes in different places with different slices can lead to a case where the smaller separation is measured at an "earlier" slice. (In Fig. (4.6) the black holes in slice b have a smaller distance than in slice a but connects the black holes where they are known to be farther apart.) This is of course quite a problem for any interpretation of initial data and especially for evolutionary sequences. However,

since there is no proper notion of a distance available one has to (and so is done in this paper) use something, knowing about the difficulties.

## 4.6 Summary

This chapter explained the method of finite differencing, methods to solve elliptic equations, and error estimates. It mentioned the inner and outer boundary conditions used in the evolutions and introduced the physical quantities that will be used in the following chapters.

Finally it introduced a new kind of distance measurement which follows a geodesic line instead of measurement used until now that follows a straight line. This geodesic distance measurement is similar to the straight line measurement in head-on collisions but shows considerable differences for rotating binaries.

# Chapter 5

# Evolutions of Puncture data

## 5.1 Introduction

This chapter deals with evolutions of Puncture data, which were discussed in section 3.2.3. The following section introduces the so-called "Cook sequence", a sequence of binary black hole initial data trying to mimic an evolution. Some of the elements of this sequence were evolved as part of this thesis. The results of these evolutions are presented in the following section and will be published separately [10]. Special attention is paid to the amount of time these evolutions take to reach a merger, the state of a binary black hole system where a common apparent horizon (see section 4.5.2) has appeared. These times seem to indicate that the initial data sets are not actually in quasi-circular orbits, but that they are in fact nearly plunging together. Some of the studied dynamical quantities will be reported on.

## 5.2 The Cook Sequence

The Brill-Linquist data, as well as the puncture data, provide means to construct an initial data set for orbiting black holes by choosing parameters corresponding to asymptotic mass and momenta. However, this choice poses a problem, because it is by far not clear what parameters represent physically realistic orbital parameters.

Cook [57] proposed to use two equal mass black holes with no spin and equal but

opposite linear momentum in quasi-circular orbit. Of course it is well known that orbits in relativity will not be exactly circular, as they radiate angular momentum and energy, and so the radius will decrease over time. But the timescale in which this happens is thought to be much larger than the orbital period. Additionally the radiation will also cary away ellipticity and thus circularize the orbit. The approximation gets better with increasing separation and in the limit of infinite separation essentially Newtonian physics will govern the dynamics. Since circularity is just an approximation, the term "quasi- circular" was used.

To construct a quasi-circular orbit, an effective binding energy $E_b$ can be defined via

$$E_b = E_{ADM} - 2M, \tag{5.1}$$

with $E_{ADM}$ being the total ADM mass of the spacetime. $M$ denotes the apparent horizon mass of one of the black holes

$$M_{irr} = \sqrt{\frac{A}{16\pi}}, \tag{5.2}$$

where $A$ is the area of the apparent horizon (as introduced in section 4.5.2. Stable quasi-circular orbits are identified by finding a minimum in the binding energy as a function of the proper separation $l$,

$$\frac{\partial E_b}{\partial l} = 0. \tag{5.3}$$

One can calculate the angular velocity $\Omega$ as seen by an observer at infinity from the binding energy via [81]

$$\Omega = \frac{\partial E_{ADM}}{\partial J}. \tag{5.4}$$

Cook used isometric Bowen-York data to actually find a sequence of circular orbits using this technique. Baumgarte adapted it to use it on the ISCO of Puncture data and Lousto et al. [29] extended this to the entire sequence. This extended Puncture data version of Cook's sequence is what is used in this thesis. The data are given

| Name | $L/M$ | $\pm X/M$ | $\pm P/M$ | $J/M^2$ | $M\Omega$ | $m/M$ |
|---|---|---|---|---|---|---|
| QCB [33] | 4.90 | 1.158 | 0.334 | 0.773 | 0.176 | 0.450 |
| QC0 [57] | 4.99 | 1.169 | 0.333 | 0.779 | 0.168 | 0.453 |
| QC1 | 5.49 | 1.364 | 0.286 | 0.781 | 0.142 | 0.463 |
| QC2 | 5.86 | 1.516 | 0.258 | 0.784 | 0.127 | 0.470 |
| QC3 | 6.67 | 1.849 | 0.2148 | 0.794 | 0.1019 | 0.477 |
| QC4 | 7.84 | 2.343 | 0.1743 | 0.817 | 0.0760 | 0.483 |
| QC5 | 8.84 | 2.772 | 0.1514 | 0.8397 | 0.0612 | 0.487 |

Table 5.1: Sequence of quasi-circular orbits as suggested by Cook and adapted to Puncture data by Baumgarte and extended by Lousto et al. [29]

.

in table 5.1. It contains a name of the data set, the position $X$ in coordinate space leading to the proper separation of the black holes $L$, the linear momentum $P$, the resulting angular momentum $J$, the angular frequency $\Omega$ and the irreducible mass $m$. All the values are rescaled with the ADM mass M.

Using this same effective potential method a puncture data sequence was constructed [33] that later was generalized to incorporate spin [99].

## 5.3 Merger Times

The data sets of the Cook sequence were evolved using the BSSN formulation, the 1+log slicing, and the hyperbolic Γ-driver with parameters $\eta = 4$, $p = 1$, and $n = 4$ for the shift (see chapter 2 or [10]). Other parameter choices were tested, though significant deviation from these values would not permit a stable evolution to merger. The data sets up to a proper separation of 7.84M could be led to merger.

For each model, runs were performed with grid resolutions of $0.08M$ and $0.06M$ on grids of $384 \times 384 \times 192$ and $512 \times 512 \times 256$ points respectively. A "transition fish-eye transformation" with parameters $a$=4, $s$=0.8, $r_0$=5.5 in the notation of [11] was performed on the initial data, transforming the coordinate boundaries at $15.48M$ to a

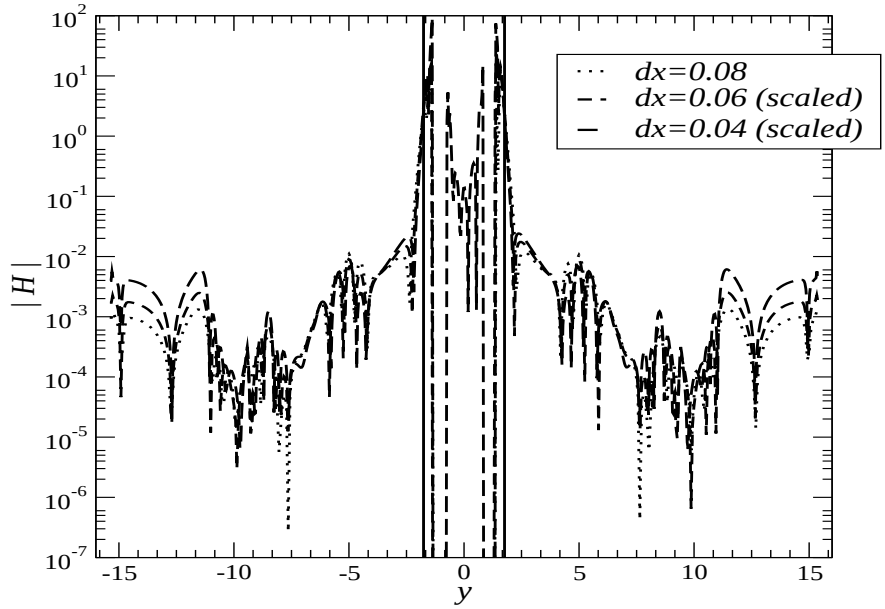


Figure 5.1: Log-plot of convergence in Hamiltonian constraint for one element of the Cook sequence shown at the time of formation of the common AH as determined from the low resolution run ($t = 17.76\,M$). The data with finer resolution is scaled down

physical distance of $45.42M$ from the origin. This causally disconnects the boundary from the merger.

To show that the code is converging in fig. 5.3 a cross section of the Hamiltonian constraint is plotted for one element of the sequence at the time of merger ($t = 15.8$) along a grid line in the $y$ direction, $(dx, y, dz)$, adjacent to the location of the punctures (the punctures are staggered between grid points). A higher resolution run ($dx = 0.04$) with boundaries in the same location on a grid of size $768 \times 768 \times 384$ was also carried out and confirmed the convergence results.

As can be seen in the plot the region disconnected from the outer boundary shows excellent 2nd order convergence, including points in the immediate neighborhood of the excision region. Significantly, convergence is maintained in the region of the common horizon formation.

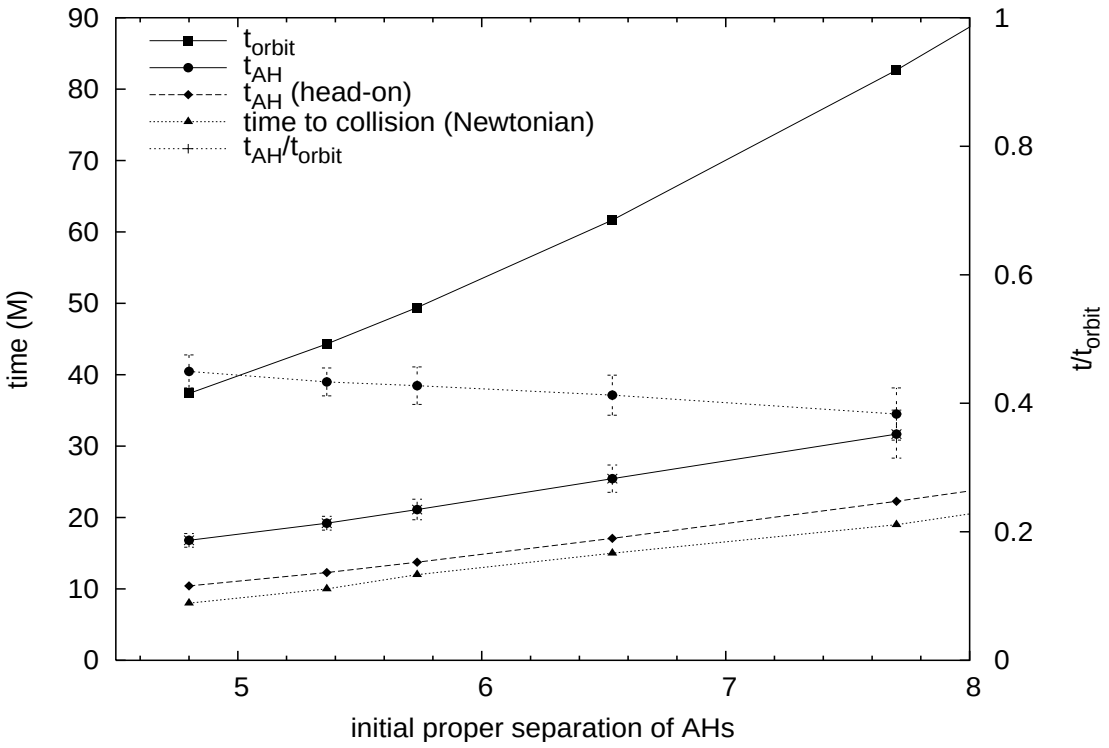


Figure 5.2: Different merger time measures as a function of proper distance between the two black hole throats. The actual merger time lines are not as steep as the expected orbital period line. They are rather parallel to the relativistic head-on and Newtonian free fall collisions. The righthand y-scale shows the ratio of time vs. the orbital time. The fraction of the orbital period each data sets evolves before it merges is going down with increasing separation. Therefore, according to this result, there will never be an orbit with these data. As indicated by the error bars, different gauge choices change the numbers only a little, not changing the overall trend.

The result of the evolutions is surprising: For each of the models studied, a common apparent horizon appeared in less than half the expected orbital period (see Fig. (5.2)). This is true even of the further separated cases where assumptions placed on the initial data might be expected to be more reasonable. The values can be compared to the merger times from a head-on collision, with each puncture starting with zero linear momentum, or even to the Newtonian free fall time for the same separation. The results of such simulations are plotted as well. They are found to run almost parallel to the inspiral curve.

One has to be very careful interpreting these numbers because as mentioned above the separation as well as the time used here are not well defined concepts. They depend on the chosen slicing. Experiments with varying gauge parameters have been done and indeed, small variations in the merger times were found (and plotted as error bars in Fig. (5.2)). Even the apparent horizon itself is a slicing dependent quantity. There are slicings where it does not even exist.

However, finding a common apparent horizon shows the existence of an event horizon (a gauge independent quantity) and the appearance of a common apparent horizon occurs only at some point after the actual event horizon merger. Thus the merger actually occurs even before the times reported here.

The main argument is the unexpected tendency of the times. The line connecting the merger times should be steeper than the free fall times. The plot shows the fraction of an orbit that the data evolve before they merge with respect to the right vertical axis. This curve clearly shows a decrease with separation. This is contrary to intuition.

Much hope was put into Thin Sandwich data. Since they are by construction close to Post-Newtonian data and rely on a helical killing vector, there is reason to believe that these data will merge at larger and larger fractions of an orbit leading eventually to an evolution for a full orbit. The following chapter will introduce the Meudon

data, a kind of Thin Sandwich data.

# Chapter 6

# Evolutions of "Thin Sandwich" Data

## 6.1 Introduction

This chapter describes the results obtained by evolving thin sandwich type initial data using a quasi killing vector ansatz, as proposed by the group in Meudon, France [77, 78]. The data are in very good agreement with Post-Newtonian approximations and are therefore believed to be much closer to astrophysically realistic data than the effective potential methods.

The chapter will start with an introduction into the construction of the data and the circular orbits, and will then deal with results evolving them. This represents the first successful attempt to evolve these data.

## 6.2 Meudon Data Construction

### 6.2.1 The Field Equations

The Thin Sandwich data construction, as described in section 3.3, starts with the free data $\gamma_{ab}, u_{ab}, \alpha$, and $K$ and solves eqs. (3.43), (3.44), and (3.45) for $\Psi, \beta^a$, and $A_{ab}$.

The Meudon data are conformal Thin Sandwich data equipped with some special choices that fix the free data. The derivation is somewhat different from York's original prescription. The construction starts with the full set of Einstein's equations

and makes some additional restrictions:

1. There is assumed to be an approximate helical killing vector[1]

$$l = \frac{\partial}{\partial t_0} + \Omega \frac{\partial}{\partial \phi_0}, \tag{6.1}$$

   where $t_0$ and $\phi_0$ are the time and angular coordinates at initial time, respectively.

2. The data are assumed to be conformally flat ($\gamma_{ab} = \Psi^4 \delta_{ab}$), with $\Psi$ being a conformal factor and $\delta_{ab}$ denoting the identity matrix

3. The data are maximally sliced ($trK = 0$).

The assumption of a helical killing vector is used because it sets the system in some rotational state. A stationary metric (one that is either static or rotating) has such a helical killing vector. Of course this assumption is an approximation since gravitational wave emission will decrease the radius of the orbit of the two black holes, and therefore break helical symmetry. (If the orbit was not decreasing the system would radiate for ever thereby increasing the total energy of spacetime infinitely.) But at least for large separations the timescale of wave emission should be much smaller than the orbital timescale, hence the quasi-killing-vector approximation should introduce only small errors. The question up to which distance the helical killing vector assumption is usable are usually based on Post Newtonian calculations. Miller [88] has done a detailed analysis on the validity of various Post-Newtonian approximations depending on the initial separations.

In contrast to Cook's sequence (compare section 5.2) - apart from the actual method to construct the circular orbit - here the circular orbit assumption is built into the construction of the data.

As explained earlier, there is no reason to believe a binary black hole to be representable by a conformally flat metric at any stage of its evolution. This approximation

[1]For a definition of a killing vector see appendix C

induces spurious radiation and though the magnitude of this error is not completely understood ([86] gives an estimate), it is hoped that it is radiated away early in the evolution and the system will quickly "settle" down to a more physically realistic state.

The maximal slicing condition is a commonly used slicing in numerical simulations of black holes. As explained in section 2.4 it is singularity avoiding, decouples the constraints, and simplifies the equations by removing $trK$. The fact that this requirement will lead to an elliptic equation for the lapse is not a obstacle. With the helical killing vector assumption there will very little evolution. So the expensive iterative process of solving the equation has to be done only once. With the use of spectral methods one can achieve very high accuracy for the lapse and the other elliptic constraint equations.

Using these assumptions five of the ten Einstein's equations are fulfilled identically. The remaining five are:

$$\Delta\alpha = \alpha\Psi^4\bar{A}_{ab}\bar{A}^{ab} - 2\partial_c\ ln\Psi\partial^c\alpha \tag{6.2}$$

$$\Delta\beta^a + \frac{1}{3}\partial^a\partial_b\beta^b = 2\bar{A}^{ab}\left(\partial_b\alpha - 6\alpha\partial_b\ ln\Psi\right), and \tag{6.3}$$

$$\Delta\Psi = -\frac{\Psi^5}{8}\bar{A}^{ab}\bar{A}_{ab}, \tag{6.4}$$

where $\partial_a$ is the regular partial derivative (since the associated metric is the flat one), $\Delta = \partial_a\partial^a$ is the ordinary Laplace operator, and $\bar{A}^{ab} = \Psi^4 K^{ab} - K\bar{\gamma}^{ab}$ is the conformal extrinsic curvature, here given by:

$$\bar{A}^{ab} = \frac{1}{2\alpha}\left(L\beta\right)^{ab}, \tag{6.5}$$

$(L\beta)^{ab}$ being the conformal killing operator applied to the shift vector:

$$(L\beta)^{ab} = \nabla^a\beta^b + \nabla^b\beta^a - \frac{2}{3}\nabla_c\beta^c\bar{\gamma}^{ab}. \tag{6.6}$$

These equations result from applying assumptions (a, b, and c) to Einstein's equations. However, they turn out to be the Eqs. (3.43), (3.44), and (3.45) of York's conformal Thin Sandwich decomposition.

### 6.2.2 Boundary Conditions

As explained in chapter 3, after a decomposition of variables is chosen (in this case the Thin Sandwich one), the free data and the boundary conditions have to be fixed. For this construction, a two-sheeted topology (Fig (3.3)) was chosen. This was done by making the throats of the two bridges boundaries of the computational domain and solve only for the "upper" sheet, the outside of the black holes. At this inner boundary all values where set to be according to the isometry condition of the Misner data: The interior four metric is mapped under a coordinate transformation $I$ with

$$I_i(t, r_i, \theta_i, \phi_i) = \left(t, \frac{a_i^2}{r_i}, \theta_i, \phi_i\right), \tag{6.7}$$

where $i$ numbers the black holes and $a$ is the radius of the horizon of black hole $i$. This leads to a topology equivalent to a pair of identical sheets (see Fig. (3.3)).

This property is immediately transferred to the following equations for the 3 metric $\gamma_{ab}$:

$$\gamma_{rr}[P] = \frac{a^4}{r^4}\gamma_{rr}[I(P)] \tag{6.8}$$

$$\gamma_{r\theta}[P] = \frac{a^2}{r^2}\gamma_{r\theta}[I(P)] \tag{6.9}$$

$$\gamma_{r\phi}[P] = \frac{a^2}{r^2}\gamma_{r\phi}[I(P)] \tag{6.10}$$

$$\gamma_{\theta\theta}[P] = \gamma_{\theta\theta}[I(P)] \tag{6.11}$$

$$\gamma_{\theta\phi}[P] = \gamma_{\theta\phi}[I(P)] \tag{6.12}$$

$$\gamma_{\phi\phi}[P] = \gamma_{\phi\phi}[I(P)] \tag{6.13}$$

Because of Eq. (2.8), the extrinsic curvature components have the same behavior as the metric, except for a possibly different sign. The sign is fixed by choosing the

direction of the normal vector $n^a$. The usual choice of a future pointing normal vector leads to a negative sign for the isometry transformation of the extrinsic curvature, which is used here.

For the shift, the isometry requires

$$\beta^r[P] = -\frac{a^2}{r^2}\beta^r[I(P)] \tag{6.14}$$

$$\beta^\theta[P] = \beta^\theta[I(P)] \tag{6.15}$$

$$\beta^\phi[P] = \beta^\phi[I(P)]. \tag{6.16}$$

The lapse enters the metric only quadratically ($g^{00} = -1/\alpha^2$). Therefore when imposing the isometry $I$ on the metric there is the open choice of the sign for the lapse:

$$I\alpha = \pm\alpha. \tag{6.17}$$

In the Schwarzschild metric the choice of the plus sign would not respect the stationarity of the metric (the killing vector $\partial_t$ of the metric would not carry one slice of the foliation into another). Contrary to that, a minus sign would do exactly that. According to [55] this also guarantees the boundary surface to be a trapped surface, which is a fact the entire procedure is based on. Therefore for this construction the minus sign was chosen ending up with a slicing that is best viewed in the Kruskal diagram Fig. (6.1)

Conditions (6.8) to (6.17) lead to requirements at the inner boundary. Eq. (6.15) requires the vanishing of $\beta^r$ since at the throat $r = a$ and $I(P) = P$, which gives $\beta^r(P) = -\beta^r(P)$. The isometry conditions give no restriction for the other components of the shift but for their derivatives:

$$\beta^r|_S = 0 \tag{6.18}$$

$$\frac{\partial\beta^r}{\partial\theta}|_S = 0 \tag{6.19}$$

$$\frac{\partial\beta^r}{\partial\phi}|_S = 0 \tag{6.20}$$

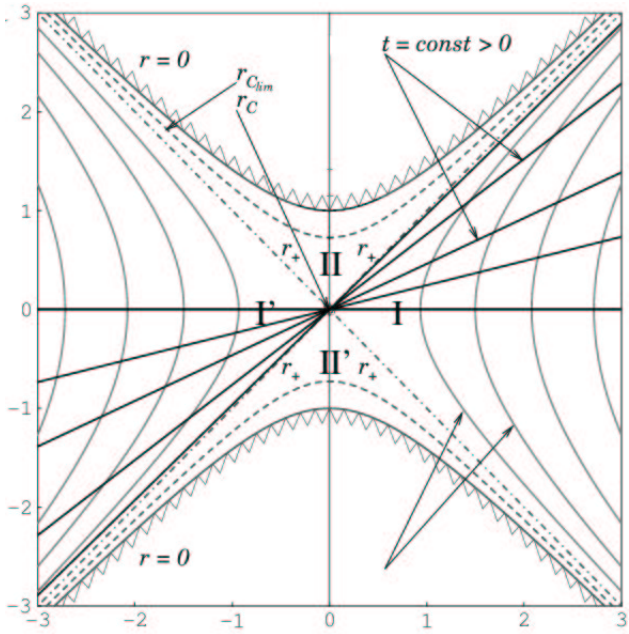


Figure 6.1: Kruskal diagram describing the chosen slicing condition for a single Schwarzschild black hole. $t$ =const. slices are straight line moving upward (future directed) in region $I$ and downward (past-directed) in $I$‘ (adapted from [101]).

$$\frac{\partial \beta^\theta}{\partial r}|_S = 0 \tag{6.21}$$

$$\frac{\partial \beta^\phi}{\partial r}|_S = 0, \tag{6.22}$$

where $S$ is the surface of the throat and is assumed to be a sphere.

For the metric a similar method using Eqs. (6.8) to (6.13) leads to:

$$\left(\frac{\partial \gamma_{rr}}{\partial r} + 2\frac{\gamma_{rr}}{r}\right)|_S = 0 \tag{6.23}$$

$$\gamma_{r\theta}|_S = 0 \tag{6.24}$$

$$\frac{\partial \gamma_{r\theta}}{\partial \theta}|_S = 0 \tag{6.25}$$

$$\frac{\partial \gamma_{r\theta}}{\partial \phi}|_S = 0 \tag{6.26}$$

$$\gamma_{r\phi}|_S = 0 \tag{6.27}$$

$$\frac{\partial \gamma_{r\phi}}{\partial \theta}|_S = 0 \tag{6.28}$$

$$\frac{\partial \gamma_{r\phi}}{\partial \phi}|_S = 0 \tag{6.29}$$

$$\frac{\partial \gamma_{\theta\theta}}{\partial r}|_S = 0 \tag{6.30}$$

$$\frac{\partial \gamma_{\theta\phi}}{\partial r}|_S = 0 \tag{6.31}$$

$$\frac{\partial \gamma_{\phi\phi}}{\partial r}|_S = 0. \tag{6.32}$$

Similar conditions are imposed on the extrinsic curvature.

The inner boundary condition for the lapse requires it to vanish at the throat. Looking at Eq. (6.5) one can notice that $A_{ab}$ will blow up, if the shift does not vanish there as well. (Vanishing of $(L\beta)^{ab}$ would suffice, but this would require the shift to be a killing vector which it is not.) Therefore an additional boundary condition for the shift is imposed:

$$\beta^a|_S = 0. \tag{6.33}$$

As mentioned in [77] and described in detail by Cook in [60], this choice is quite problematic. At first Eq. (6.33) is a change of the boundary condition for the shift, which in turn changes the boundary from being guaranteed a trapped surface and the reflection surface for an isometry transformation [55]. If the isometry cannot be applied at this surface, then this means that the boundary condition may not be appropriate. And even if they are, a problem using two boundary conditions - one being a Dirichlet and the other a von Neumann one - is not well posed. So it is not certain, that there is a solution to the equations at all. So the data are actually not a solution to Einstein's equations. However, as stated before the error could be shown to be very small compared to all other errors.

Therefore, for this thesis a pragmatic view was adopted, saying that the data - even though they are rigorously not correct and will not converge to a correct solution - have an error much smaller than numerical errors generated through finite differencing and are thus not unrealistic within the inaccuracies of the method. This is backed up by Cook who has fixed the boundary condition [60] and finds similar results. His method, though correct in principle, is very difficult to apply practically.

At the outer boundary, all values where set to those of an asymptotically flat metric, which should be a reasonable choice if the the boundary is far enough away from the dynamical system. However, it is not compliant with the assumption of the black holes to be in circular orbit, for if they were, the outgoing radiation would have to be compensated by incoming one. Since these data are only used as initial data, and do not radiate forever, this is not seen as a critical problem.

### 6.2.3 Circular Orbits

Up to now the rotational state of the black holes has not been specified. Since binary black holes are only determined by their mass, their angular momentum, and their separation (neglecting a possible charge), these are the only parameters to be set. Considered is here an equal mass system, and the angular frequencies of the black holes were set to agree with the orbital angular frequency resulting in a so-called synchronized (co-rotating) system. This means that the two bodies are always facing the same side of each other. Such a state is translated into a geometrical condition by demanding that the throats of the black holes should be killing horizons associated with the helical symmetry. Each null-geodesic generator of the horizon surfaces $S_q1$ and $S_2$ must be parallel to the helical killing vector $l$, which in turn means that $l$ is a null vector at the throats:

$$l * l|_{S1} = 0 \qquad and \qquad l * l|_{S2} = 0. \tag{6.34}$$

The data are set up at a stage were the evolution is assumed to be quasi-stationary. In this case the killing vector can be chosen to be:

$$l = \frac{\partial}{\partial t_0} + \Omega \frac{\partial}{\partial \psi_0}, \tag{6.35}$$

where $t_0$ and $\phi_0$ are the time and azimuthal coordinate of an asymptotically inertial observer. The time coordinate of the data is to obey this symmetry and agrees with

the killing vector:

$$l = \frac{\partial}{\partial t}. \tag{6.36}$$

Together with Eq. (2.5) this leads to

$$l^a = \alpha n^a + \Omega \beta^a. \tag{6.37}$$

As above all values are set to be conform with the asymptotic flatness assumption. At the outer boundary this means, in particular, that the conformal factor $\Psi$ and the lapse function $\alpha$ both go to unity at the outer boundary. Comparing Eqs. (6.37) and (6.35) one is led to the outer boundary condition for the shift:

$$\beta|_{OB} \to \Omega \frac{\partial}{\partial \phi_0}. \tag{6.38}$$

In fact, this is the only place in the system of equations were the orbital frequency $\Omega$ enters. But being a boundary condition it does not follow from an internal condition, it has to be set according to an external principle. If one chooses the outer boundary condition $\beta^a|_{OB} = 0$ for instance one would end up with a head on collision as in the Misner data. Whatever the choice is, the inner boundary condition ensures that the black holes will co-rotate with this choice. The problem is to find the correct choice of $\Omega$ to put the black holes in a quasi-circular orbit.

As explained in section 4.5.1 the Komar mass is defined through the presence of a killing vector. Using Eq. (6.37) as the killing vector, one ends up with the following expression for the Komar mass:

$$M_K = \frac{1}{4\pi} \oint_\infty (\nabla^i \alpha - K^{ij} \beta_j) dS_i. \tag{6.39}$$

With Eq. (6.38) inserted for the shift term this leads to

$$M_K = \frac{1}{4\pi} \oint_\infty \nabla^i \alpha dS_i - 2\Omega J_{ADM}. \tag{6.40}$$

Now [26] (lemma 2.3) states that if there is a helical killing vector (and no linear momentum) then the following holds:

$$M_K = M_{ADM} - 2\Omega J_{ADM}. \tag{6.41}$$

Reversing the argument one gets:

$$M_{ADM} = \frac{1}{4\pi} \oint_{\infty} \nabla^i \alpha dS_i \iff l^a \text{ is a killing vector.} \tag{6.42}$$

This is what is done here: fix all other parameters, and then vary $\Omega$ until Eq. (6.42) holds (in practice the procedure is stopped when they agree better than $10^{-5}$).

## 6.3 Interpolation of Initial Data

The quasi-killing vector data were computed by the Meudon group with the help of the *Lorene* (*L*angage *O*bjet pour la *RE*lativité *N*umériqu*E* [41, 42]) code, using the spectral methods mentioned in chapter 4. The AEI evolution codes use the *Cactus* computational toolkit which uses finite differences (see also chapter 4) to solve the evolution equations. To evolve the data, one therefore needs to translate them to a finite differencing grid by taking the coefficients of the expansion. The data are given in forms of binary files containing the spectral coefficients of the solution. Inserting these coefficients into the series of polynomials one gets an analytic function of the (numerical) solution. This function is used to get values for the grid-functions of the finite differencing code.

Once that was done, the machinery of *Cactus* could be used to evolve the data. Since one of the important features of the spacetime is the location and evolution of the horizons, it was hoped to find the horizons numerically in these data as well. Especially since their location was known, at least initially, to be at the throat. To find horizons one has to interpolate using grid points on both sides of the horizon surface. Therefore also points inside the horizon are needed. Fortunately the data are inversion symmetric. Using this property (Eq. (6.7)) the data inside the horizon could be filled. For every point inside the black hole (that can be pictured to belong to the lower sheet in Fig. (6.2)) an image point outside (in the upper sheet, where the data are given) could be identified (compare Fig. (6.2)).

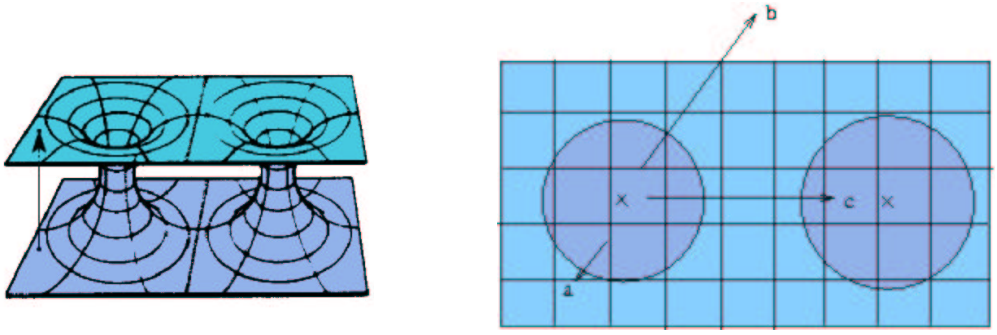


Figure 6.2: Use of isometry property of Meudon initial data to fill interior of the holes.

These points do not have to be grid-points, and had to be interpolated. This was done using hermitian polynomials of (in this case) second order to interpolate the functions as well as their derivatives at once leading to a very efficient and accurate result[2]. Another way of getting the data at the image points is using the spectral coefficients provided in the data file (both methods were implemented and compared).

With the interpolation method the points mapped outside the grid (b) needed special treatment. This was not the case when using the spectral coefficients to get the data at the image points since the Meudon data are computed on a compactified grid (that extends to infinity). Only the points (c) that got mapped into the other black hole needed special treatment.

Here the values first were approximated using quadratic extrapolation and second the interpolation procedure was repeated several times, hoping that by then, the data points inside the other black hole are filled. Using this procedure the interior of the black holes could be filled to high enough accuracy to converge with increasing resolution.

Using the interpolation method the points (b) were given the outer boundary value, leading to a small error. With higher resolution the number of points with images

[2]They are implemented in the Cactus interpolator by J. Thornburg [112]

| Name | coordinate distance | proper distance | $\omega$ | $M_{ADM}$ | $J_{ADM}$ |
|---|---|---|---|---|---|
| M12 | 12 | 4.95863 | 0.164512 | 5.22409 | 0.888448 |
| M13 | 13 | 5.30006 | 0.14712 | 5.0512 | 0.880134 |
| M14 | 14 | 5.63471 | 0.132657 | 4.91652 | 0.874838 |
| M15 | 15 | 5.96358 | 0.120329 | 4.81426 | 0.870729 |
| M16 | 16 | 6.28724 | 0.109958 | 4.73045 | 0.869769 |
| M18 | 18 | 6.9218 | 0.0930458 | 4.60392 | 0.869574 |

Table 6.1: Physical quantities of the used Meudon initial data sets.

outside the grid increased, leading higher errors close to the singularities. But these errors were cut away by the excision and did not influence the quality of the evolution. A similar problem occurred for smaller test runs: creating smaller grids led to many more points being mapped off the grid, including points that were clearly not close to flatness. So in smaller test runs these errors needed to be taken into account. In larger "production" runs this problem did not occur since only points that were radially far enough out got mapped off the grid, and the flat-metric treatment was a good approximation.

In all the evolutions done for this thesis the spectral coefficients were used to fill the interior of the black holes because this method was easier and had a better accuracy.

The data sets are publicly available through the EU network [76]. They consist of eight sets: a separation in coordinate space of 12, 14, 16, and 18, each with two numbers of co-location points, 21 or 33 (named by their coordinate separation). Additionally two sets (using 21 co-location points) with coordinate distances of 13 and 15 were kindly provided by Phillippe Grandclemént, one of the authors of the Meudon Data. The free parameters were set to get physical quantities of the system as shown in table (6.1). The coordinates used resulted in very strong requirements on the numerics. Since the ADM mass is approximately 5, all numerical settings have

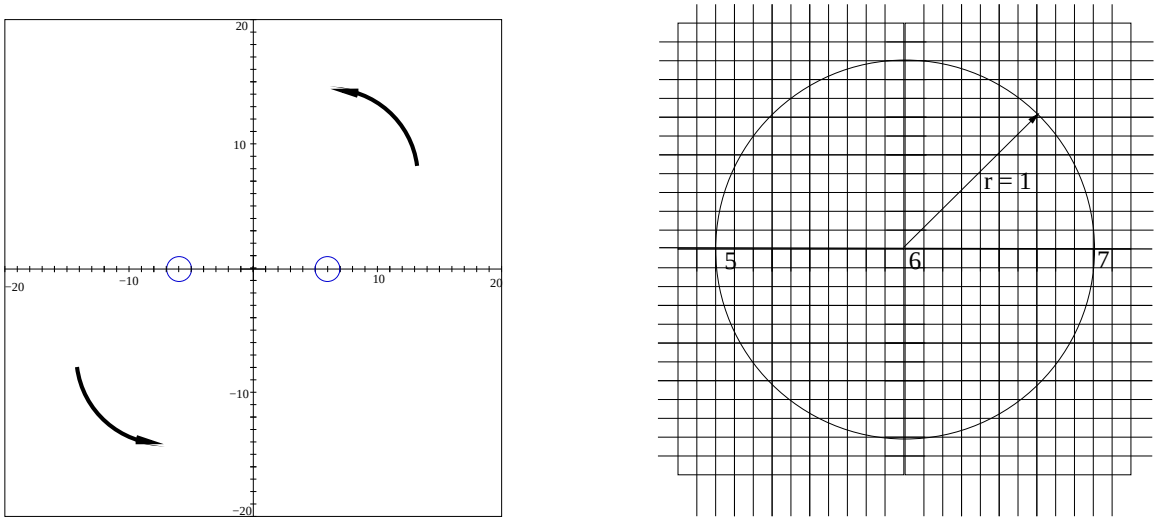


Figure 6.3: Setup of smallest Meudon Data set (M12): 400x400x200 grid-points with a resolution of 0.1. The black holes are located in coordinate space at ± 6 on the x-axis. The entire system is rotating counterclockwise. The other data sets have a similar setup. The right plot is a zoom into one of the black holes.

to be divided by 5 to get units of $M_{ADM}$ as they are usually used. For example, an evolution had to be kept running to approximately 100 to reach $20M_{ADM}$, resulting in 4000 iterations (with a spatial resolution of 0.1 and a courant factor of 0.25). In turn this led to a naturally very high resolution that improved the quality of the runs.

Note that this is a coordinate effect due to the construction procedure. A corresponding puncture data evolution requires approximately 1500 iterations.

Whenever in the following the unit M is used it is implied to be $M_{ADM}$.

The data were set up as shown in for the example of the smallest set in Fig. (6.3): The black holes are located on the x-axis at ±6 and rotate in the xy-plane counterclockwise.

For the first experiments, the boundary was put at 20. A minimal resolution of 0.1 had to be chosen. With the horizon radii being 1 and the safety buffer 4 points, this leads to 12 grid-points being excised along an axis. A coarser resolution would lead to fewer grid-points inside the horizon (and buffer), too few for excision to work.

Due to the reflection symmetry across the z=0 plane only the $z > 0$ part of the grid had to be used sparing half the size. This minimal setting already leads to a grid size of 400 x 400 x 200 points. When evolving 120 grid-functions (a quite typical number for black hole evolutions) and using double precision one easily ends up using approximately 30 Gbyte of memory. It brings not only the need for a high number of processors but also requires fast and efficient I/O methods, because the amount of data written to files is very high.

## 6.4 Results

These initial data sets were evolved, with the main goal being to lead them to merger, defined by the appearance of a common horizon, and extract as much information about the physical properties as possible to compare them with similar information obtained evolving Puncture data.

### 6.4.1 Initial Data

The Meudon initial data consist of a metric, an extrinsic curvature, as well as a lapse and shift that preserve the killing symmetry.

The conformal factor $\Psi$ has the form shown in Fig. (6.4). The metric is conformally flat, so it is completely described by $\Psi$. The interior part populated via the isometry transformation is plotted in a blue dotted line in the 1d plot. The metric shows steep gradients close to the singularities.

As in the Schwarzschild solution in isotropic coordinates (Eq. (3.16)), these singularities are just coordinate singularities. The physical singularity is to the future of the slice. Nevertheless those coordinate singularities would lead to a crash of the code as well, thus the reason for excision. Higher resolution is also required, and would help to resolve the gradients better, but it would also lead to points even closer to the singularity, producing even higher gradients. Therefore it would not necessarily

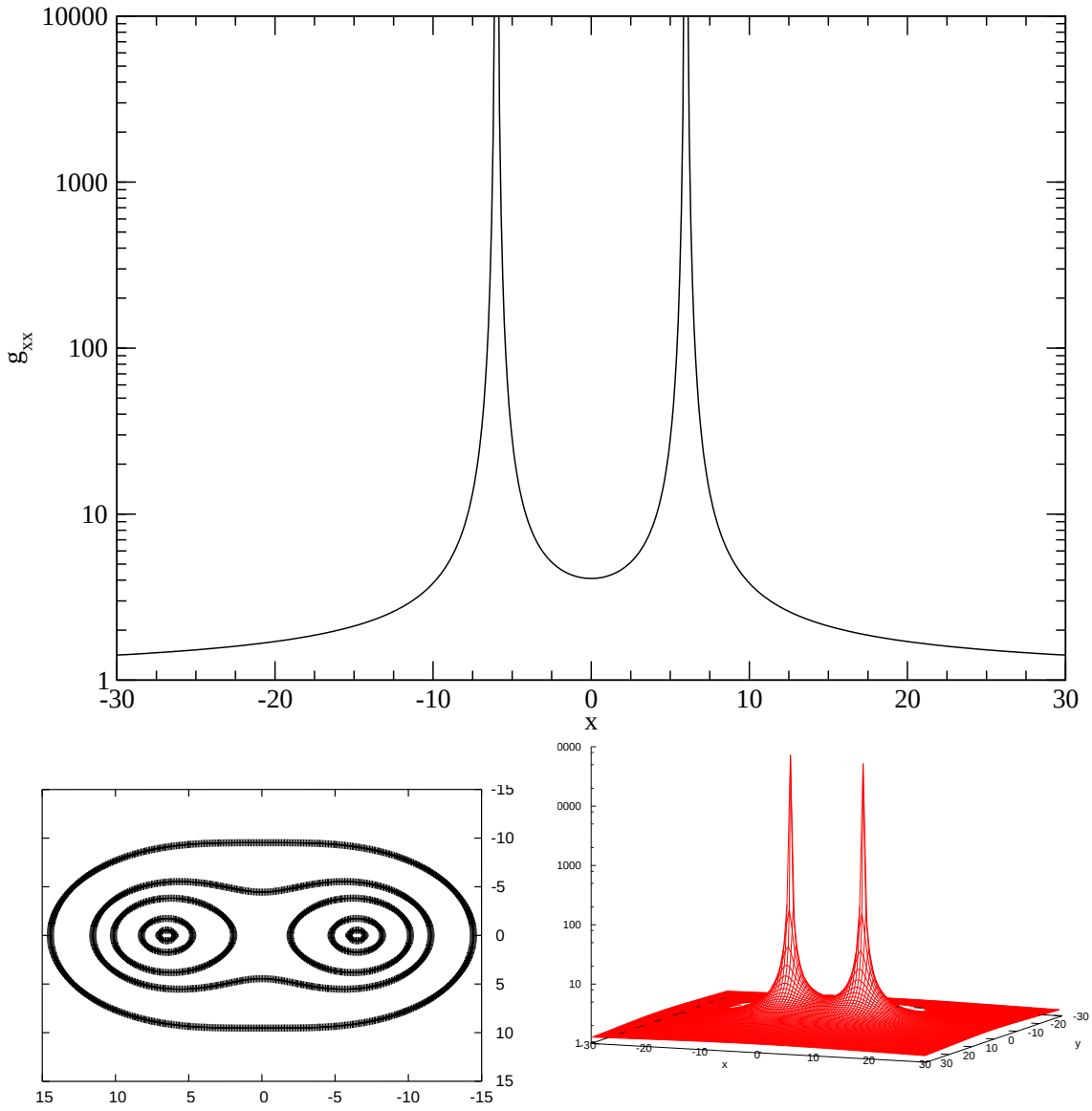


Figure 6.4: Metric of Meudon initial data (M12). Top: Logarithmic 1d plot along the x-axis. As comparison function $f_1$ and $f_2$ are added to show the falloff. The inset shows that close to the singularities the metric falls off faster than $r^{-2}$ but slower than $r^{-3}$. Lower left: contour plot on the xy-plane. (The contour lines are plotted for 2.2, 3, 4, 10, and 100.) Lower right: logarithmic height field over the xy-plane

cure code crashes.

The contour plot shows that the first continuous contour line is at $g_{xx} \simeq 2.5$ and at the outer boundary the metric is still 2.2, more than double the value it is assumed to have at the boundary, and it does not have a circular (Schwarzschild-like) form, assumed in the extraction procedure for gravitational waves.

The initial extrinsic curvature of the Meudon data is shown in Fig. (6.5). One can clearly see the spikes inside the horizons. These spikes are introduced by the shift vector (compare Eq. (6.5)) and are a result of the rigid co-rotation which leads to large components of the shift at the outer boundary that get mapped via the isometry into the interior (the infinity of the lower sheet of Fig. (6.2)).

Again the interior part set up through the isometry is blue in the 1d plot which again is a cut along the x-axis whereas the lower left plot of Fig. (6.5) is a contour plot on the xy-plane and the lower right plot of Fig. (6.5) is a height field plot of the values on the xy-plane. The inset is a zoom to show the deviation from zero outside the black holes. Though visible, it is quite small, less $10^{-3}$ from the peak inside the holes.

As can be seen in the contour plot the extrinsic curvature has a 180 degrees rotation-symmetry. Since the extrinsic curvature is a generalized time derivative of the metric, this hints at the rotation state of the system.

One of the supposed advantages of the Meudon data is that they provide an initial gauge choice that preserves the killing symmetry. The lapse function consistent with the helical killing vector is plotted in Fig. (6.6). The lapse crosses zero at the horizons and goes to negative one at the singularities. Outside the black holes, it smoothly goes to one towards the outer boundary.

The evolution equations themselves are equally valid with a negative lapse, and there is some empirical evidence with Schwarzschild that using a negative lapse can result in stable evolutions [20]. This may, however, depend on details of the excision

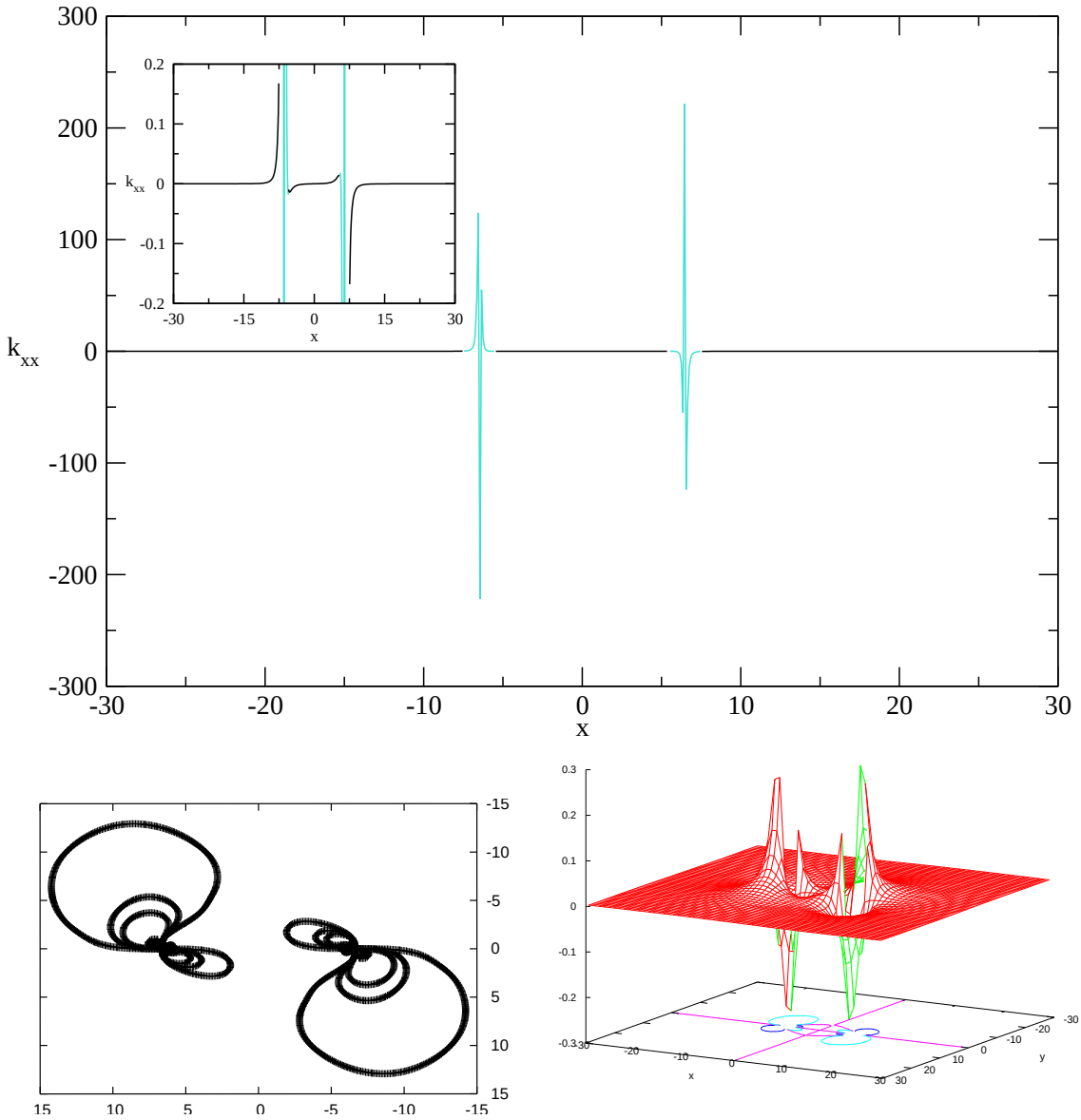


Figure 6.5: Extrinsic curvature component $A_{xx}$ of Meudon initial data (M12). 1d plot along the x-axis. The sharp spikes in the horizon's interior result from the isometry transformation on the co-rotation shift. Lower left: contour plot on the xy-plane. (The contour lines are plotted for 0.01, 0.05, 0.1, and 1.) Lower right: height field over the xy-plane

techniques employed. Note that the points inside (with negative lapse) would evolve backwards in time whereas the points in the exterior spacetime would evolve forward. Errors inside the black hole(for instance caused by the excision boundary condition) will move inwards with time, so with reversed time they will move outwards thus could pile up at the horizon.

The contour plot shows that the first continuous contour is at $\alpha \simeq 0.5$ and the lapse is still below 0.7 at the outer boundary.

The shift function plays a very important role in these data. As explained earlier, the coordinates are set up to rotate with the black holes. This is done solely by the shift. As can be seen in Fig. (6.7), there is a clear rotation in the initial data. This figure also points to a potential problem. Due to the rigid co-rotation the outer boundary will move faster than light if put far enough out. This may lead to errors.

Note that there is no outward (radial) component in the initial profile. The left plot is again a 1d cut through the x-component of the vector along the x-axis. It shows large spikes in the interior of the horizons. These spikes stem from the co-rotation profile of the shift and lead to similar spikes in the extrinsic curvature. The x-component of the shift grows along the y-axis towards the outer boundary. Via the isometry this growths is mapped into the horizon producing the large spikes.

Since the shift evolution equations ($\Gamma$-drivers Eqs. (2.39) and (2.38)) have the tendency to counterbalance the infall of the grid-points into the black hole, they mainly act on the radial component of the shift. Therefore the initial profile is changed dramatically close to the black holes during the evolution (compare Fig. (6.11) and description in next section). Nevertheless, further away it keeps more or less the unchanged co-rotation profile (see right plot in Fig. (6.7)).

One of the most important features of Meudon data is that they assume a helical killing vector. If this assumption was true there would be no evolution of the grid variables. So an analysis of the time derivative of these functions seems appropriate.

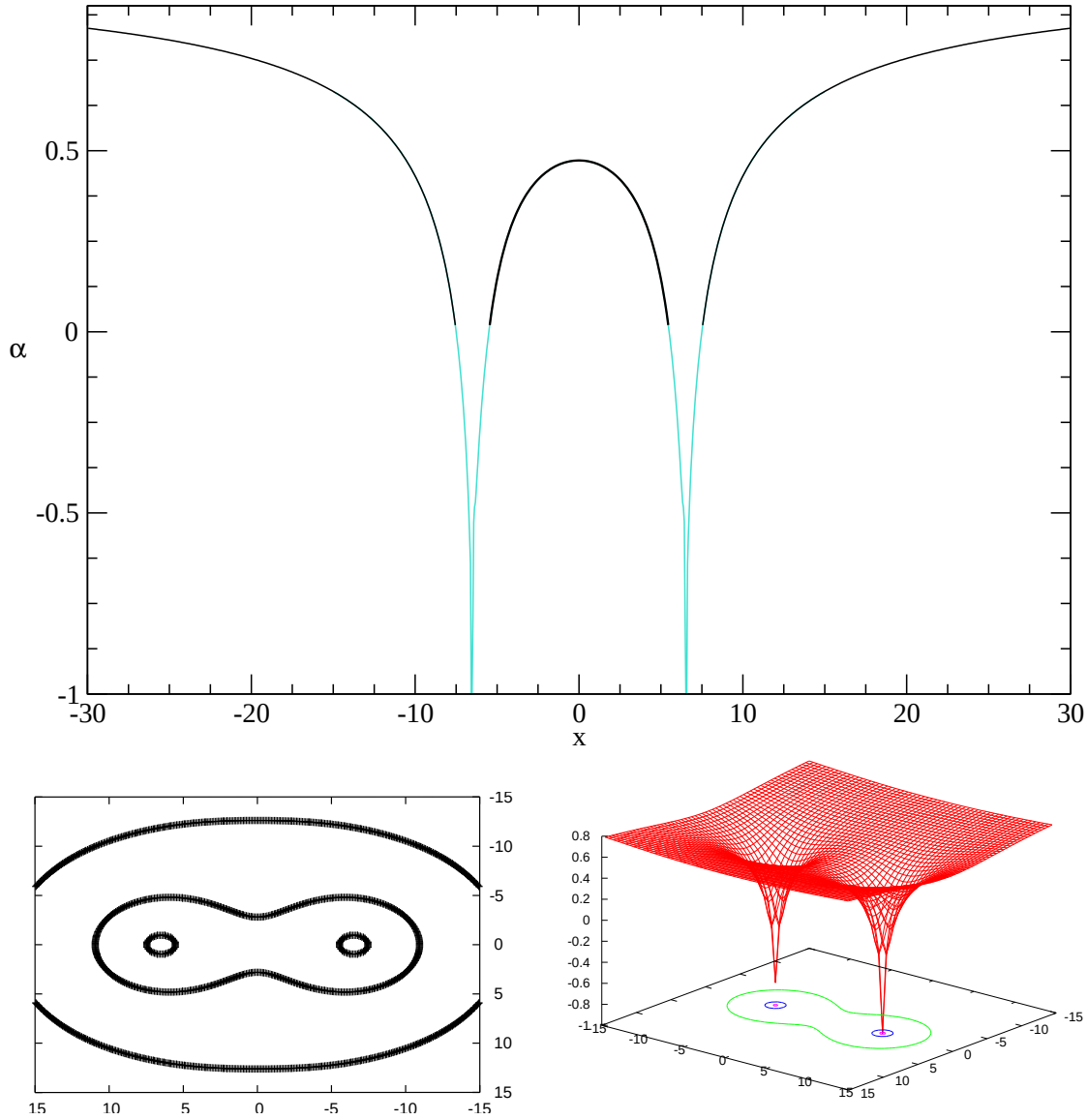


Figure 6.6: Initial lapse profile of Meudon data (M12). 1d plot along the x-axis. The lapse crosses zero at the horizons and goes to negative one at the singularities. Lower left: contour plot on the xy-plane. (The contour lines are plotted for 0.0 (the horizon) , 0.5, and 0.7.) Lower right: height field over xy-plane.

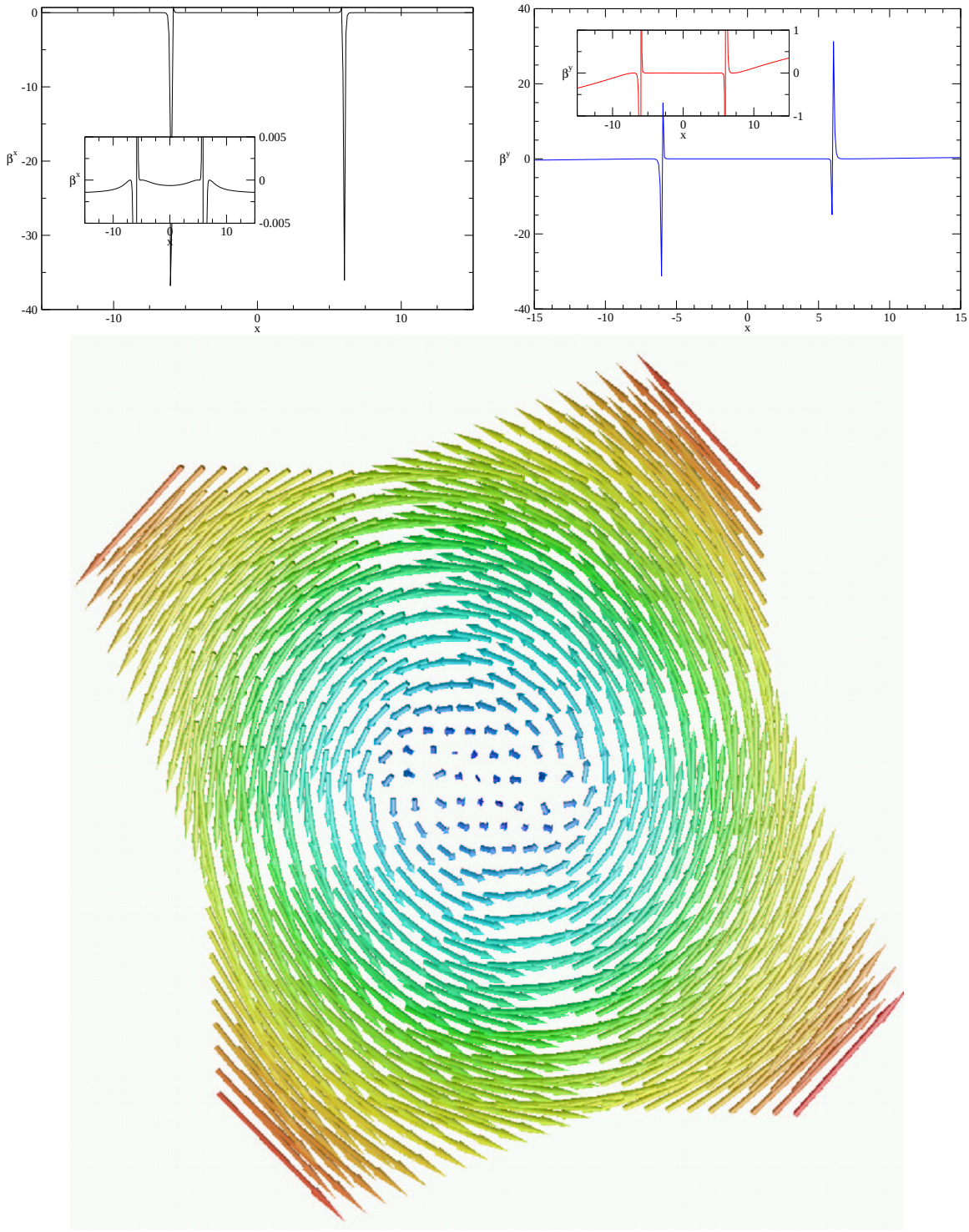


Figure 6.7: Initial shift profile of Meudon initial data (M12). Upper left: cut of the x component of the vector along the x-axis. Upper right: Cut of the y component of the vector along the x-axis. The insets zoom in to emphasize the small values outside the horizon. The y-component shows the rotational profile. Lower: Arrow plot of the shift vector on the xy-plane. The very large spikes in the interior are cut to visualize the rotation state.

The initial time derivative of the metric function $g_{xx}$ is shown in Fig. (6.8) whereas Fig. (6.9) shows the time derivative of the xx-component of the (traceless) extrinsic curvature $A_{xx}$.

As one can see, the metric is very much static and (except for the interpolated interior) the time derivative is very small. The zoom-in on the right side shows that its maximum is $5 \times 10^{-5}$ outside the horizons.

The extrinsic curvature at first sight looks very similar: only at the horizon is there noticeable deviation from zero. However, here the deviation happens already outside the horizon (the left plot clearly shows a dip to $-0.05$ just outside the horizon).

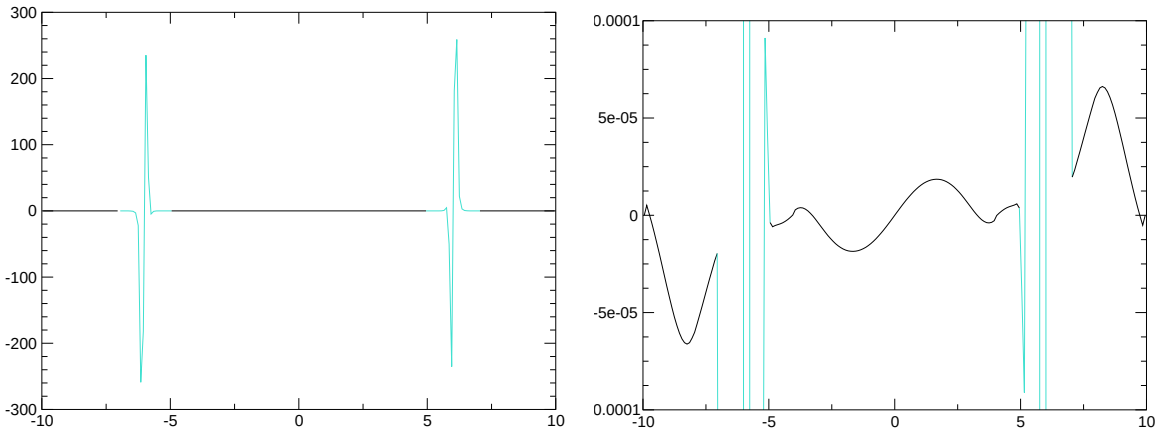


Figure 6.8: Initial time derivative of the metric function $g_{xx}$ of Meudon initial data (M12). Left: full scale plot to visualize spikes. Right: zoom-in on y-axis to visualize interior deviation from zero. This deviation outside the is outside the horizon less then $7 \times 10^{-5}$.

Additionally, even away from the horizons the time derivative of the extrinsic curvature is $10^{-3}$ and therefore 100 times as big as the time derivative of the metric. So one can state: The helical killing vector approximation is fulfilled to a very high degree away from the black holes, limited by the extrinsic curvature, which evolves on a shorter timescale. This higher limit could come from the fact that the determination of the time derivative uses the source (right hand sides) of the evolution Eqs.

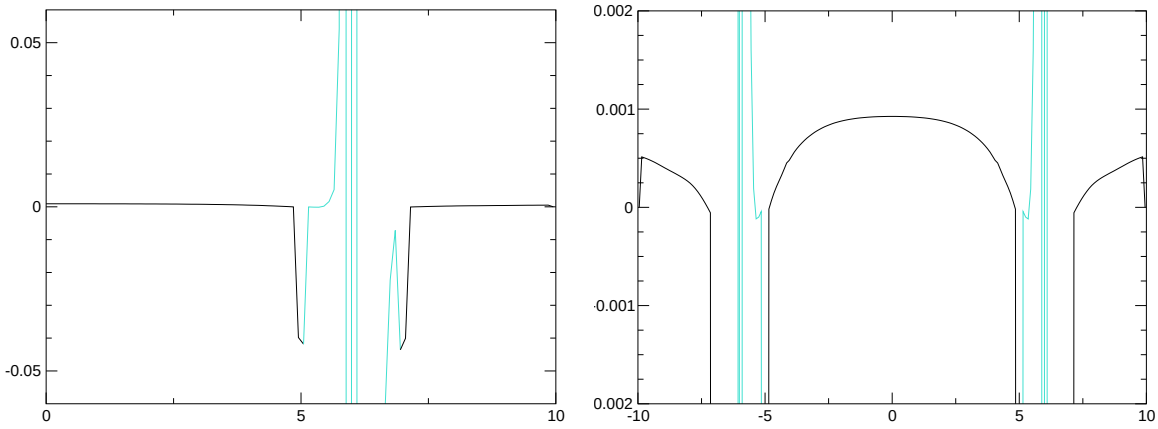


Figure 6.9: Initial time derivative of the (traceless) extrinsic curvature component $A_{xx}$ of Meudon initial data (M12). left: full scale plot to visualize spikes. right: zoom-in on y-axis to visualize interior deviation from zero. The deviation from zero outside the horizons is about $10^{-3}$.

(2.12) and (2.13). The source of the extrinsic curvature includes a second derivative of the lapse. This derivative is computed using finite difference methods, and therefore includes an error that could account for at least part of the deviation from zero, especially since there are large gradients near the horizons which increase the finite differencing errors. Thus one sees an indication that very high resolution finite differencing is needed.

However, another reason for the deviation is probably the regularization. Recall that since the lapse goes to zero at the horizon, the spatial derivatives of the shift had to be set to zero as well. As explained earlier the shift itself was also set to zero at this boundary leading to an inconsistency. This inconsistency results in an (small) error in the shift that gets transported to an error in the extrinsic curvature.

### 6.4.2 Evolution

Since experiences with Puncture data have shown that the closer separations of black holes are much easier to evolve (which is of course natural since the holes will collide earlier and can then be treated differently, using excision of the merged black hole or

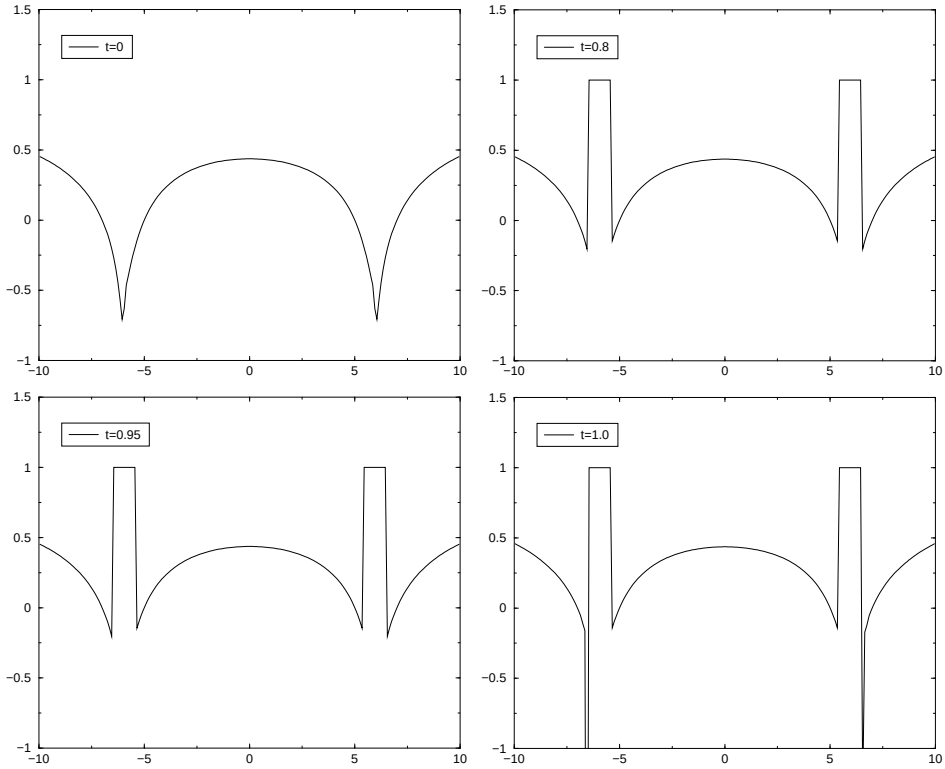


Figure 6.10: Evolution of the lapse function starting with original lapse profile (with the horizon's interior filled via the isometry transformation) of Meudon data set M12. Shown are specific times to demonstrate the special behavior.

even close limit techniques) and also due to limitations of computational resources demanded by the coordinate choice, the experiments were started with the data set of smallest separation, M12: the combination of 21 spectral co-location points and a coordinate separation of 12. (see Fig. (6.3)). Starting with the gauge given by the Meudon data and evolving the gauge using the live gauges ($\Gamma$-driver/1+log) introduced in chapter 2, this data set could be evolved for only around 1M.

In Fig. (6.10) snapshots of this evolution are shown. The first snapshot is taken at the initial time step. The second is taken at time 0.8M. Apart from the excision, which was applied already at the first time step the profile is essentially constant. It stays that way through time 0.95M. One can clearly see that shortly after that at 1.0M the negative part of the lapse develops a large negative spike, causing the

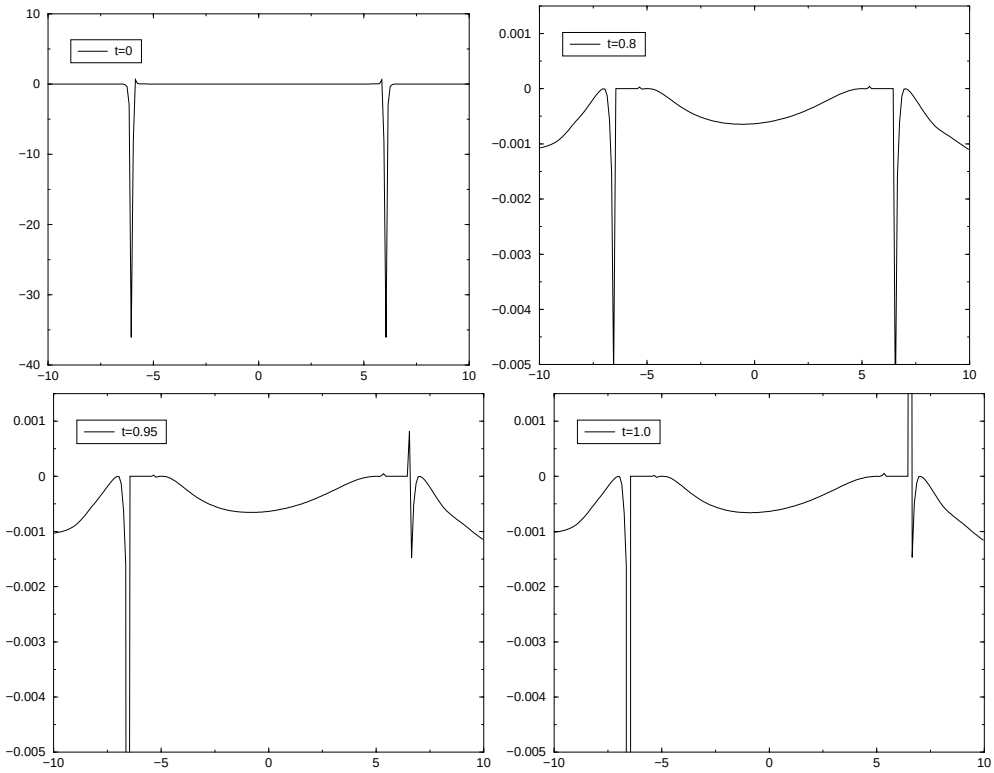


Figure 6.11: Evolution of the shift function starting with the original profile (and the horizon's interior filled via the isometry transformation). It stays unchanged (except for excision) until 0.8 at which point a spike begins to develop. Note the different scale in the first plot.

evolution to crash.

As shown in Fig. (6.11), the shift has a similar behavior. After the initial time step where excision is done (cutting away part of the interior spike), the profile stays the same through to time 0.8M (note the change of scale on the y-axis). At 0.95M one can already see some asymmetries that grow to large spikes at 1.0M, where the code crashes. However, these changes in the shift are fairly small compared to the co-rotation profile which is kept stable over the entire evolution.

This behavior can be validated looking at the L2 norm of the Hamiltonian constraint shown in Fig. (6.14). The Hamiltonian violation stays very small until at time 0.8M it starts to grow rapidly until the code crashes at 1.0M.

### 6.4.3 Gauge Experiments

The gauge choice included in the Meudon data is not mandatory. It is the one, that is consistent with the assumption of a helical killing vector. Nevertheless, it seems that this choice is not suited for numerical evolutions. The regions of negative lapse close to the excision boundary are causing numerical instabilities to grow. Because of the vanishing of lapse and shift at the horizon any error occurring there will stay there, accumulate, and eventually grow too large for the code to handle.

Therefore it seemed natural to modify the lapse and set it to zero everywhere inside the horizon. Recall that these are gauge quantities and as such can be changed freely. In these regions the only evolution is due to the shift. However, it minimizes evolution and it reduces instabilities that were created through the negative lapse.

Setting the lapse to zero at the horizons introduces a kink there (the function is only $C^0$), since the radial derivative of the lapse is not zero on the outside. Looking at the evolution equation for the extrinsic curvature, Eq. (2.13), one notices that this kink will propagate through to the time derivative of $K_{ab}$ and may introduce additional errors, which could be even worse than the original negative lapse. Therefore this had to be tested numerically.

A third idea was to ignore the suggested lapse profile, in the knowledge that this will break the (approximate) helical symmetry. Experience with puncture data evolutions suggest that an initial evolution phase allows the system to settle faster into a stable configuration. So another alternative is to set the initial $\alpha = 1$ everywhere.

Fig. (6.12) summarizes the modifications to the lapse suggested here. Plotted are the $\alpha = 1$ profile, the original quasi-killing-vector lapse profile, and this same profile with the interior lapse set to zero (called "frozen" lapse). Since the deviations from each other are not very large, the right hand plot zooms into one of the black holes.

In Fig. (6.13) the time derivative of the extrinsic curvature is plotted, indicating a violation of the killing symmetry, and thus an initial evolution kick.

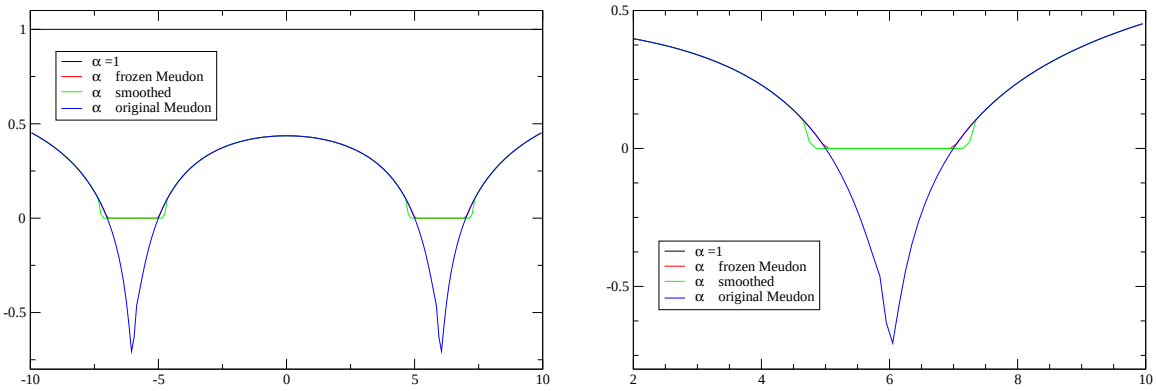


Figure 6.12: Different initial lapse profiles. The original Meudon profile (with applied isometry) becomes negative inside the horizons. The "frozen" profile is set to zero inside the horizon, the "smoothed" is set to zero slowly (already outside the horizon) and $\alpha = 1$ is the gauge usually used for puncture data evolutions. The plot on the right is a zoom in to visualize the differences between the profiles.

It is easy to see what was expected: the original quasi-killing-vector gauge profile had the smallest time derivative of $K_{ab}$ while completely ignoring the helical gauge led to the largest time derivative. The changed quasi-killing-vector profile (zeroing the lapse inside the horizon) is (of course) as good as the original profile outside and zero inside the horizon, but showed bad spikes at the horizon.

This suggests the idea to smooth out the transition from the original profile to zero. The (frozen) lapse profile was additionally multiplied by the following function $f(r_i)$, $r_i$ being the (coordinate-)distance from black hole $i$:

$$f(r) = \begin{cases} 0 & \text{if } r < a \\ \exp(-\frac{(r-(a+0.4))^2}{0.01}) & \text{if } a < r < a + 0.4 \\ 1 & \text{if } r > a + 0.4, \end{cases} \tag{6.43}$$

which over approximately 5 grid-points (depending on resolution) creates a smoother transition from the original lapse profile to zero. In Figs. (6.13) and (6.12) this profile is called "smoothed". This smoothed profile creates the expected behavior: Now at the horizon the time derivative of the extrinsic curvature is very small, but outside the horizon it is worse. Unfortunately the drawbacks outside the horizon seem to be stronger than the improvements at the horizon, and this is echoed in the evolution

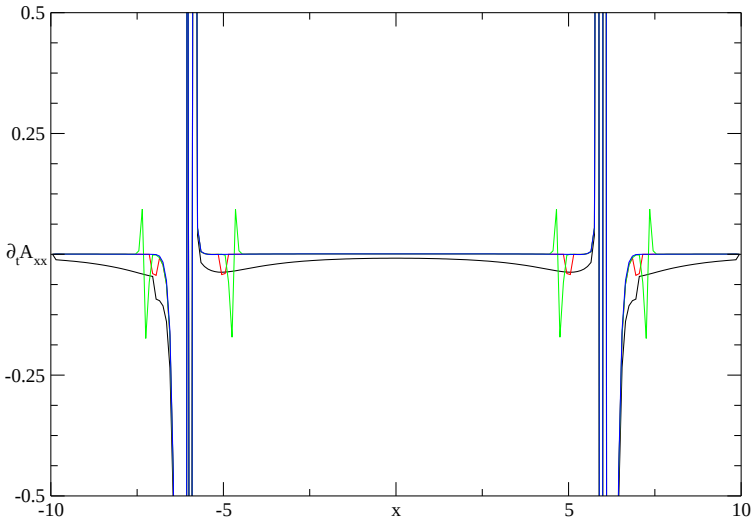


Figure 6.13: Time derivative of the extrinsic (trace-free) curvature for different initial lapse profiles. As expected the $\alpha = 1$ profile produces the largest time derivative, the frozen and the smoothed profiles agree except for spikes close to the horizons and the original Meudon profile clearly gives the smallest time derivative of the extrinsic curvature. Note that $\alpha = 1$ has the largest profile but is smooth everywhere.

results.

Recall that the Hamiltonian constraint is zero for solutions of Einstein's equations. Derivations from zero is a good indication for inaccuracy. In Fig. (6.14) the L2 norms of the Hamiltonian constraints of the first few M of evolution beginning with the different lapse profiles is shown. One clearly sees that the $\alpha = 1$ choice creates larger initial errors: the Hamiltonian grows quickly. However, very quickly the Hamiltonian levels off and even shrinks again such that after time 3 it is smaller than the Hamiltonian of the original Meudon profile.

The method of smoothing, at least in this form, has proven not helpful. The Hamiltonian constraint grows so fast, that already at time 0.1M, the code crashes.

The Hamiltonian of the $\alpha = 1$ profile is quite small, until it suddenly blows up and the code crashes. As in the evolutions of the original Meudon profile (Figs. (6.10) and (6.11)) the gauge quantities develop sharp spikes shortly before. Thus the coordinates

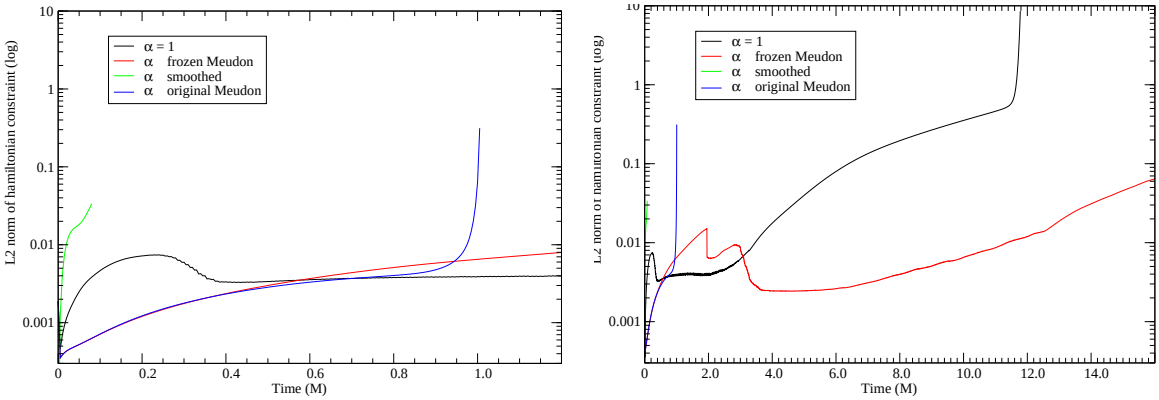


Figure 6.14: Evolution of the L2 norm of Hamiltonian for Meudon data with different initial lapse profiles (left: zoom into early time). The $\alpha = 1$ profile has an initially quickly growing Hamiltonian, but it levels down and behaves very well. The frozen Meudon profile run behaves best and the Hamiltonian stays below 0.01. The smoothed lapse profile and the original Meudon profile runs die very early. The two evolution runs that do not crash early are the ones beginning with $\alpha = 1$ or the frozen Meudon lapse profile. After 10 M the $\alpha = 1$ run died as well.

become too twisted for the code to handle and it crashes.

*As a result it seems that the original Meudon lapse profile with the abrupt setting to zero inside the horizon is the most stable choice.*

### 6.4.4 Long Term Evolutions of M12

Using the best lapse profile (frozen Meudon) of the previous chapter,large scale simulations were started. The runs used $400 \times 400$ grid-points with a resolution of 0.1 which set the boundaries to $\pm 20$. These evolutions could actually be held stable enough to lead it to merger.

In Fig. (6.15) the result for a successfully merged run is shown. As the plot shows, the individual horizon masses could be held constant with an drift below 2%. The masses actually increase which is consistent with radiation falling into the holes, and not necessarily numerical error. At time 18M a common horizon appeared.

This plot also shows a quantitative measurement: the two black holes of an initial

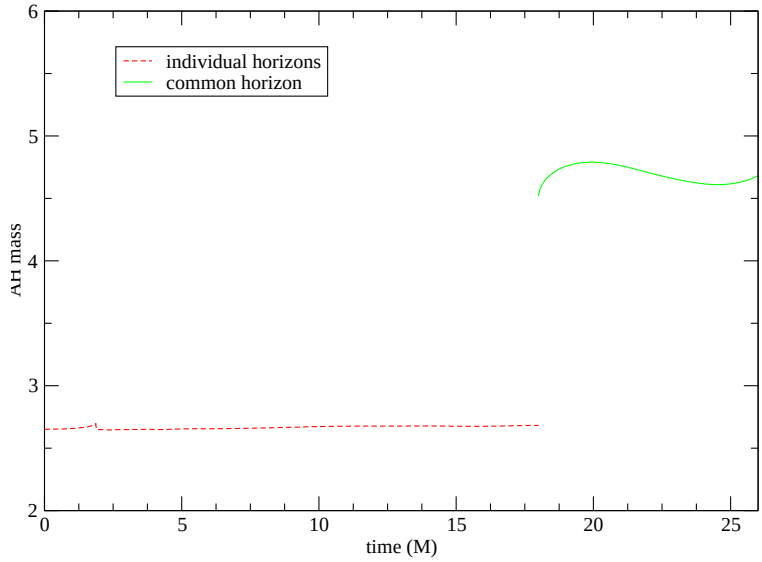


Figure 6.15: Horizon masses of an evolution of M12. It reached a common horizon after 18M. The horizons could be found consistently always when searched. The individual horizon masses ($2 \times 2.65$) merge to a black hole with a total horizon mass of 4.51.

irreducible mass of 2.65 merge to a black hole of mass 4.51 initially. But this mass is quickly growing to be 4.68 at which point it starts to decrease again and oscillates about 4.6.

A more technically interesting quantity of an horizon is its radius. This radius is a coordinate depended quantity and can therefore say nothing about the physics. However, it is crucial for excision, since this can only be done inside this radius. Looking at Fig. (6.16) one sees that that the system is very symmetric. The two individual horizon radii are indistinguishable from each other. However, what is plotted here is the minimal radius of the horizons. This does not imply symmetry on the shape. The radii grow quickly initially but the growth slows down later. This growth is wanted. As mentioned in section 2.4.2 it can be controlled by the $\eta$ parameter of the $\Gamma$-driver shift condition Eq. (2.39), and allows the excision region to grow accordingly and so swallow the regions of largest constraint violation inside

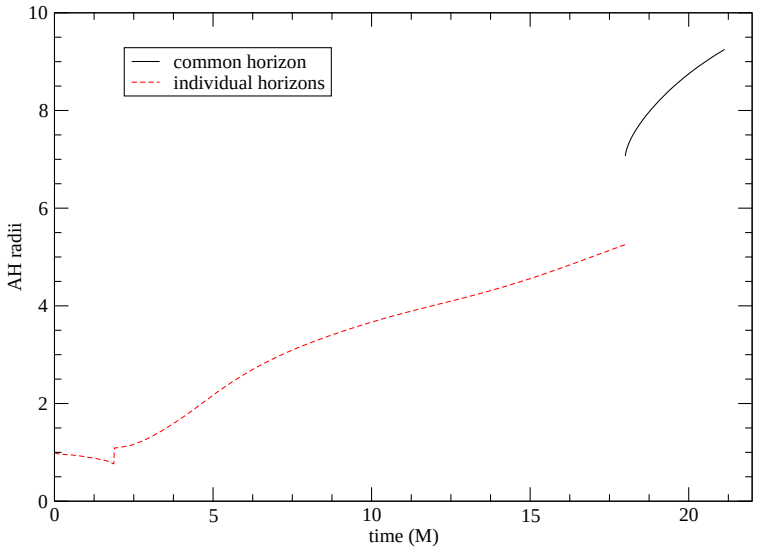


Figure 6.16: Horizon radii of an evolution of M12. The radii grow from initially 1.0 to 5.25 controlled using the $\eta$ parameter of the shift evolution equation (in this simulation was $\eta = 3.2$).

the horizon. Therefore a fine tuning of the $\eta$ parameter was crucial for a successful run.

After 1.5M there is a jump in the radius. This jump appeared in all evolutions of Meudon data and shows in most of the horizon quantities. This could indicate that initially the horizon finder is tracking an inner horizon. The radius decreases until the horizon finder looses it and searches again with the old initial guess, finding it again at radius 1.

To test the symmetry of the initial setting better, the different circumferences mentioned in Eqs. (4.31), (4.32), and (4.33) were computed. In coordinate space they are spheres by construction. With an error of less than half a percent the three circumferences agree. However, Fig: (6.17) shows that the minimal initial difference is growing. This is understandable since the black holes are coming closer to each other and tidal forces should start to deform them. The deformation could also (at least partly) come from the gauge. As will be seen in Fig. (7.3), some gauge choices can

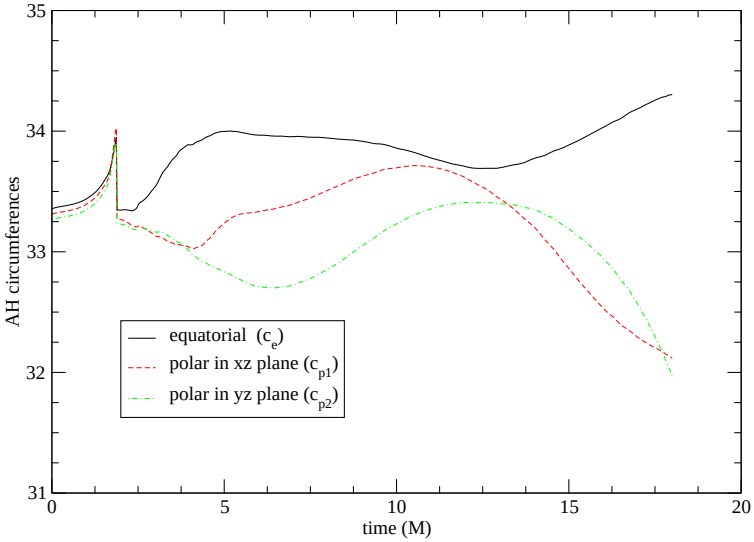


Figure 6.17: Horizon circumferences of an evolution of M12. The initially small deformation grows with time.

lead to deformations of the horizons.

There is some peculiarity about the circumferences though: Initially $c_{p1}$ (the circumference in the plane of both black holes) is larger, after 12M however, $c_{p2}$ (the circumference in yz-plane, perpendicular to the $c_{p1}$) is the larger one. This is indicating strong shearing forces that tear the holes along the line of motion. The equatorial circumference stays the largest of the three over the entire evolution. In all three circumferences one can see the before mentioned jump after 1.5M. Note that the total change of the circumferences is far less than 10% of the circumferences themselves.

The common horizon surface itself is strongly deformed when it appears. As can be seen in Fig. (6.18) it contains both of the individual horizons but is itself very concave. This strong deformation gives an explanation why it was not possible to use the ratio of the polar circumferences versus the equatorial one (see section 4.5.2) to estimate the quasi-normal ringing. The circumferences are measured along the $\phi = 0$ or $\phi = \pi$ axis (xz-plane or yz-plane). This need not to be the major axes of the spheroid. Therefore such a deformed (rotating) horizon wouldn't allow for a reliable

number. Another important fact can be seen from the picture: the common horizon takes up almost all the grid. Therefore boundary effects will almost immediately influence the horizon, which destroys any chance of doing reliable physics.

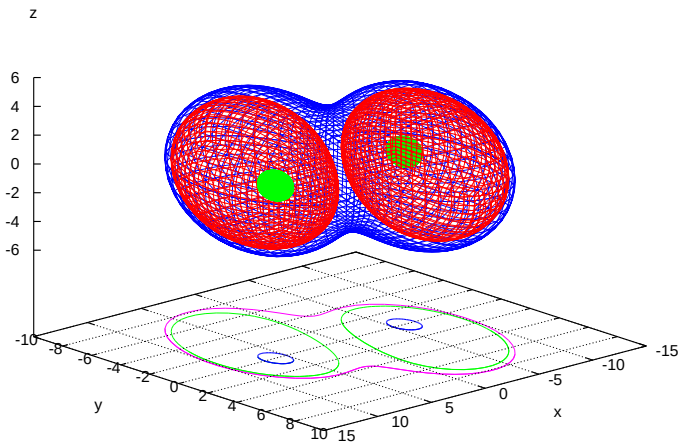


Figure 6.18: Visualization of AH surfaces. The individual horizons are contained in the common one, which is very deformed. The contour at the bottom shows the location of the horizons at the $z = 0$ plane: the two small initial horizons, the much larger individual horizons at the time of merger, and the common horizon, closely circumscribing the two individual ones.

Looking at the gauge functions one sees the before mentioned behavior. Fig. (6.19) shows snapshots of the lapse evolution. Clearly can be seen that at least up to 1M the evolution is fairly static. Apart from the growth of the excision region, the profile doesn't change. A later snapshot at 2M shows that the profile starts to collapse. Between 2M and 4M the lapse seems to flatten across the grid, then starts evolving back to the familiar profile of a maximal slicing which is reached around 6M. This profile stabilizes and stays more or less unchanged until time 20M. At this point the lapse between the black holes starts do decrease rapidly. When it is as smaller than approximately 0.3 a common horizon appears and excision can cut away the interior.

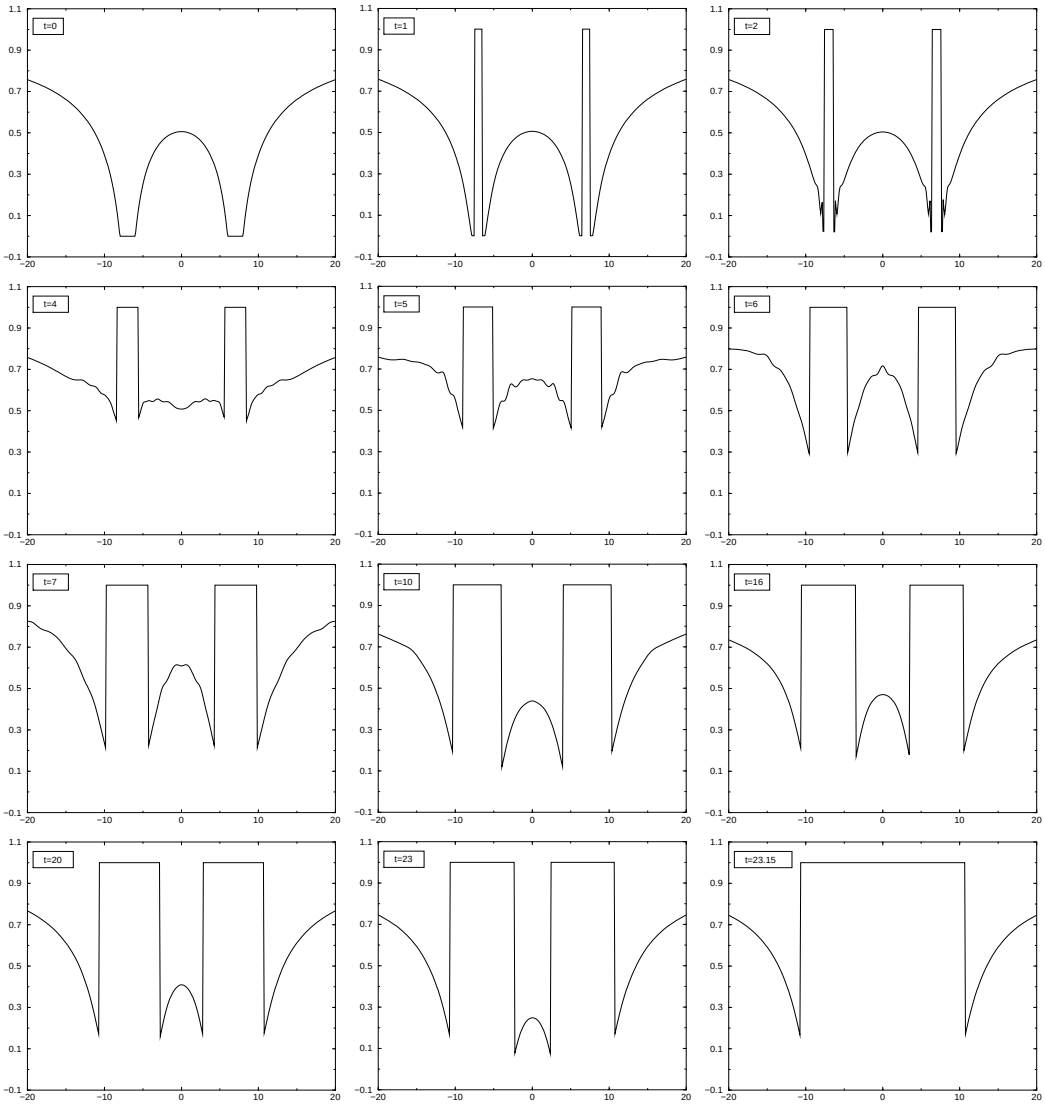


Figure 6.19: Lapse evolution of long term Meudon data run (M13). The lapse stays basically unchanged (except for excision) for 2M, undergoes violent changes until 6M and stays again unchanged until merger at 23M.

If one takes the constancy of the gauge profile as an argument for the validity of the helical killing vector assumption, then one has to claim that after a time of 2 M this assumption breaks down. This is the point where the profile starts to change rapidly.

Snapshots of the shift evolution are shown in Fig. (6.20). Here a similar behavior can be seen. Starting with the Meudon profile the shift stays unchanged until 2M. At that point spikes start to grow at the excision boundary. These spikes grow until they reach approximately 0.5. In between the two holes these spikes form a profile commonly seen in evolutions of puncture initial data. Again at about time 6M this profile is reached and stays unchanged until at 23M a common horizon is found, and excision cuts away the interior. Recall that a negative shift is pointing left and a positive one is pointing right in this cut. So the shift points outwards around each black hole, pulling in the horizon, which has the effect of slowing the growth of the horizons.

Thus the shift behavior seems to completely fulfill its purpose. It starts off with a rotating profile and is able to control the infall of the grid-points into the horizon, thereby regulating the horizon's radius in coordinate space.

When numerical runs are done a very important question to ask is about the accuracy and its reliability.

One indicator is the violation of the constraints, which are not enforced during the evolution. The Meudon data sets are computed using spectral coefficients. They are shown to converge exponentially with an increasing number of co-location points [78] (see Fig. (6.21)). These data had to be mapped onto the finite difference grid. What can be tested is the convergence of the imported data which should show second order.

Outside the horizons this tests only the convergence of the constraint computation within *Cactus*. The Hamiltonian constraints for three different runs with the resolution doubled (multiplied by four) are shown in Fig. (6.22). As can be seen they line

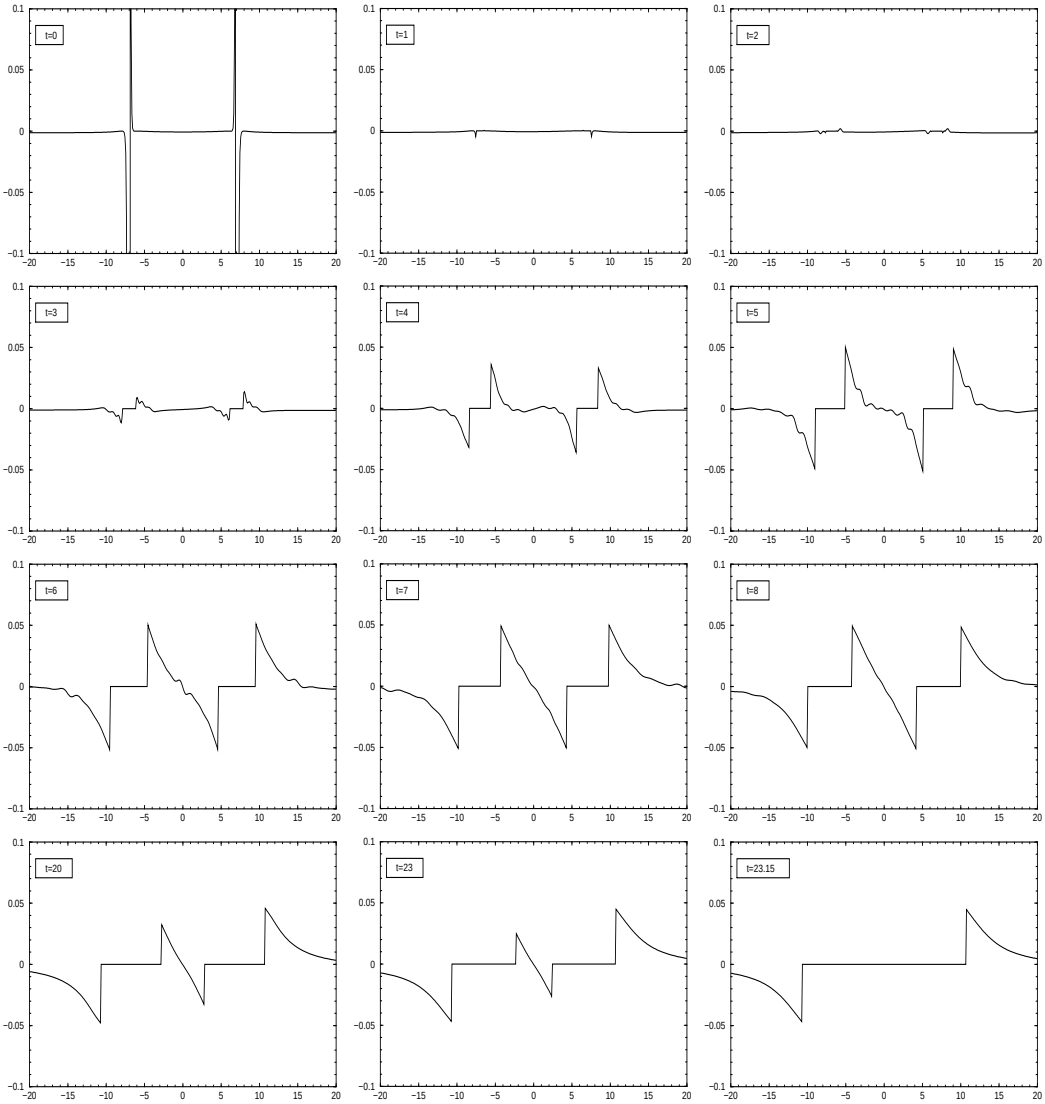


Figure 6.20: Shift evolution of long term Meudon data run. Plotted is the x component of the shift vector. The shift stays unchanged (except for excision) until 3M, goes through violent changes until at about 6M it has transformed to the profile known from Puncture data evolutions.

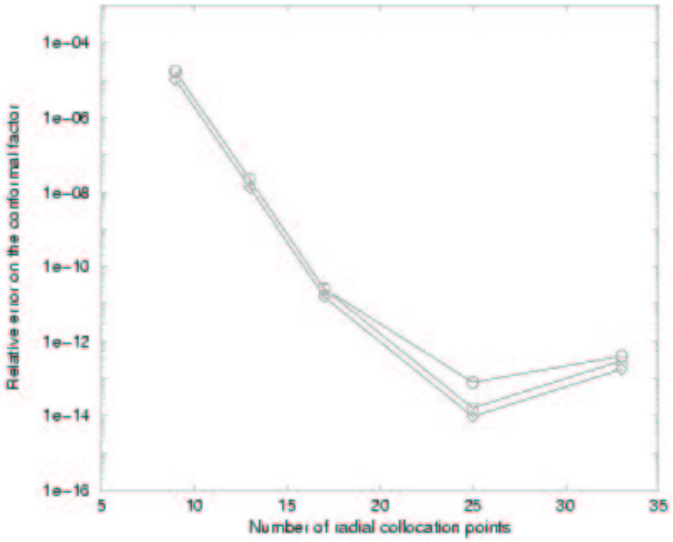


Figure 6.21: Convergence of the Meudon Data. The data show exponential convergence with increasing number of co-location points. Once the error is down to $10^{-14}$ numerical errors (adding up with the number of co-location points) is more important, leading to a growth of the error. (with permission from [78])

up in the region beyond $x = 14$ (they have already converged so well that they are indistinguishable). In the region $7 < x < 14$ the lines are deviating more and more getting closer to the horizon. Here higher resolution is needed. However, they are not converging to zero but to a line with the signature of a Chebychev polynomial. This is the numerical error that Meudon data have (the construction of which was using Chebychev polynomials). Inside the horizon even higher resolution is needed. As shown in Fig. (6.23) which is a zoom using still higher resolution the Hamiltonian constraint converges here as well. Towards the singularity it becomes worse. Due to the high gradients a higher resolution is needed the closer one gets to the singularity. In this plot one can also distinguish a non-smoothness at the horizon, which stems from the boundary error mentioned in section 6.2.2. However, as can be seen in Figs. (6.22) and (6.23), the Hamiltonian violation is not larger than $10^{-5}$ outside the horizons and can be brought down to that number inside the horizon using very

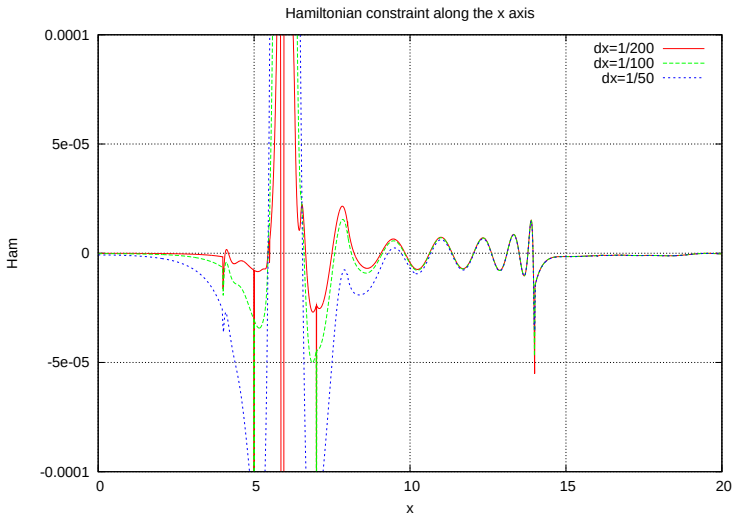


Figure 6.22: Convergence of Hamiltonian of Meudon initial data (M12). The Hamiltonian constraint for three different resolution is plotted. It has converged nicely in the region $x > 14$, can be seen to converge in the region $7 < x < 14$, and shows the need for much higher resolution inside the horizon. It does not converge to zero but to the numerical error of the Meudon data. (The horizon is indicated by vertical lines.)

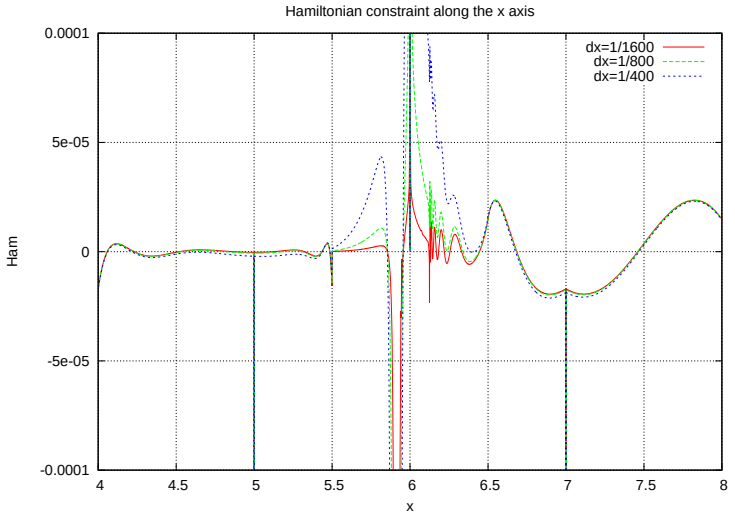


Figure 6.23: Convergence of Hamiltonian of Meudon initial data (M12). The Hamiltonian for three different resolutions is plotted (doubling the resolutions of Fig. (6.22). The lines line up outside the horizon and deviate from each other getting closer to the singularity. (The horizon is indicated by vertical lines.)

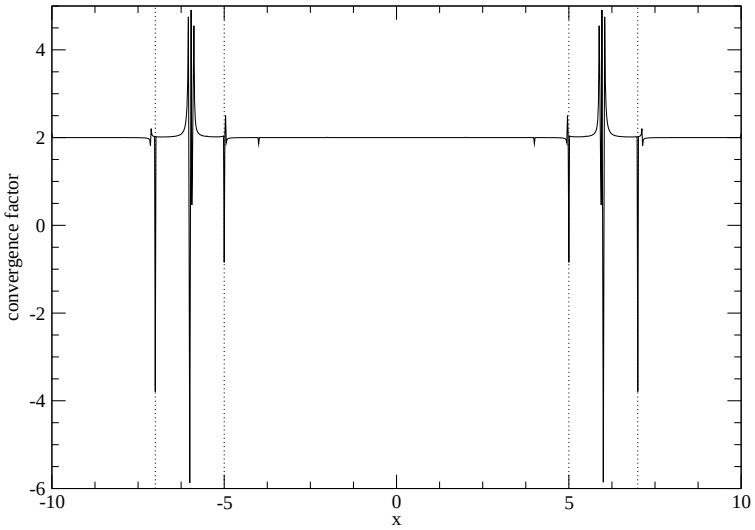


Figure 6.24: Convergence factor of Hamiltonian of Meudon initial data (M12). The factor stays 2 almost over the entire domain. Close to the horizons the Hamiltonians of different resolutions cross over (their differences become zero) leading to sharp spikes in the convergence factor (compare Eq. (4.11)).

high resolution. However, for practical purposes this resolution is much too high.

### 6.4.5 Comparison of Different Meudon data sets

As mentioned above there are 10 different sets of publicly available Meudon data. Six sets contained spectral coefficients with 21 co-location points and four sets contained those with 33 co-location points. So the first comparison was done between the "low" resolution and the high resolution data sets. M12 was given in both configurations. So these two were compared. The difference is shown in Fig. (6.25). As can be seen, the higher resolution data have a smaller Hamiltonian constraint. However, it is smaller by a factor of 3 approximately, and the 21 co-location point data have a very small Hamiltonian constraint already. So for these runs it was not necessary to use the larger (and slower) high resolution data sets in the evolutions.

The data sets M12, M13, and M14 (using 21 co-location points) were evolved until merger. The behavior of the apparent horizon masses can be seen in Fig. (6.26).

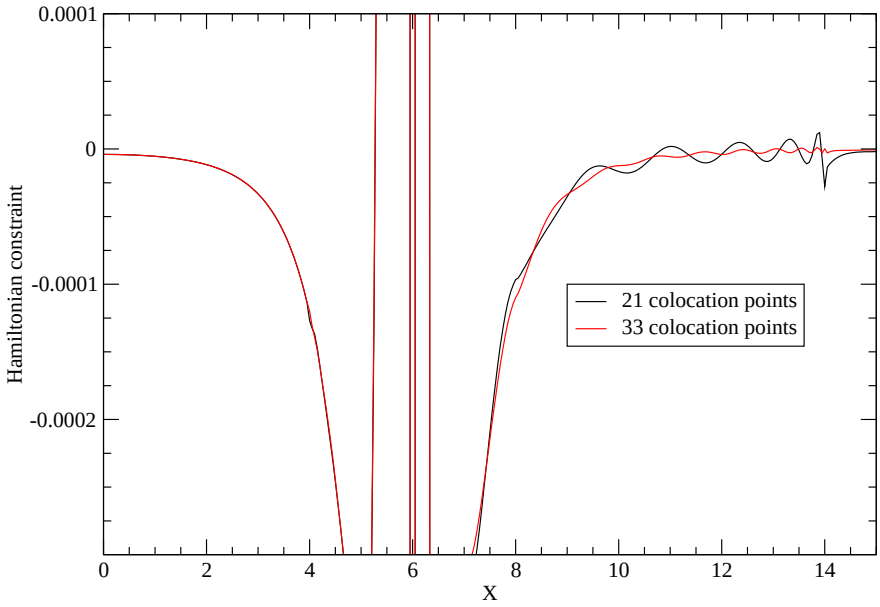


Figure 6.25: Hamiltonian constraints of M12 data sets with 21 or 33 co-location points. The 33 co-location points clearly produce a smaller Hamiltonian constraint. However, the Hamiltonian constraint of the 21 co-location points data is small enough.

They are all kept very constant until they are lost when a common horizon was found and the interior excised away.

Again a look on the horizon radii tells something about technical details. In Fig. (6.27) one can see that the radii all grow controlled using the live shift. These growing radii allow for a growing excision region which helps keeping the constraint violation down.

The Meudon data set M16 was thoroughly tried to merge as well. (M15 arrived too late to undergo the same investigation.) A plot of the fine-tuning of the $\eta$-parameter of the shift evolution equation Eq. (2.39) is shown in Fig. (6.28). The resulting L2 norms of the Hamiltonian constraint is shown in Fig. (6.29) . As can be seen the effect of the $\eta$-parameter is not very large and comes into play only at late times but the effect for the Hamiltonian constraint is crucial. It will blow up earlier if the horizon grows too low but crash if it growth too fast. For M16 it could not be hold

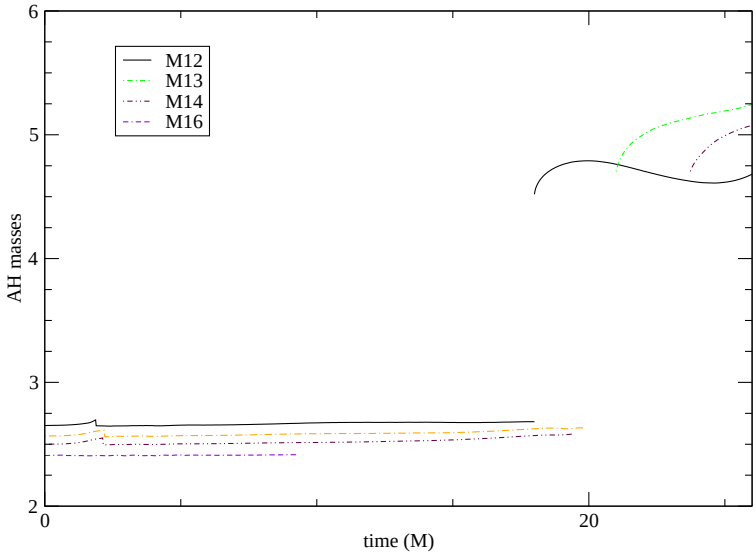


Figure 6.26: Horizon masses for evolutions of various Meudon data sets. For the sets M12, M13, and M14 a common horizon was found. For sets M13, M14, and M16 the individual horizons were lost some time before the common horizon was found. In the M16 case the common horizon did not appear before the run died.

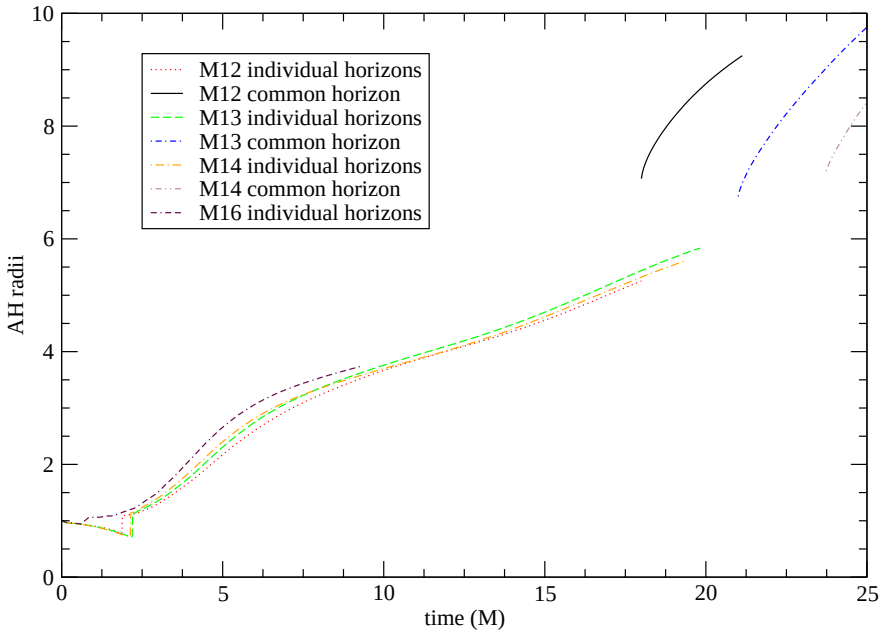


Figure 6.27: Horizon radii for evolutions of various Meudon data sets. for the sets M12, M13, and M14 a common horizon was found.

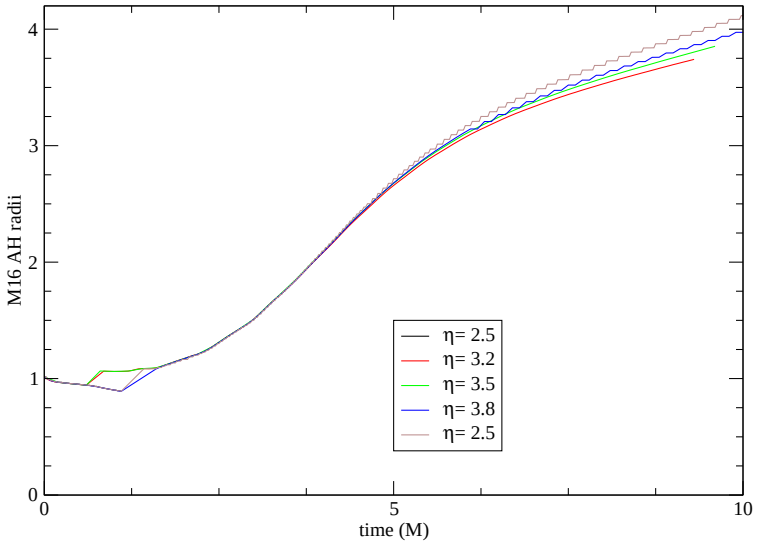


Figure 6.28: Growth of horizon radii for evolutions of M16 using different $\eta$-parameters. With growing $\eta$ the AH radius grows faster allowing for faster growth of the excision region. However, choosing $\eta$ too large or too low the run will crash.

down long enough for a common horizon to form.

### 6.4.6 Comparison of Meudon Data and Puncture data

As explained in chapter 3 it is very difficult to get information about the physical relevance of initial data. Therefore much hope was put into comparison of different sets. This was hoped to deliver at least some of the missing information. But comparing different initial data sets is quite tricky. Starting with different decompositions or different choices of the free data one will get different equations for the physical quantities. This or a different choice of the boundary conditions will naturally give different results. Now it could well be that different equations with different choices lead to the same physical results, especially since all these systems try to do the same: simulate two black holes in orbit about each other. But using a different metric and extrinsic curvature means using a different slicing. That means that the three dimensional manifold is a different one. Even if one gets similar results for instance for the

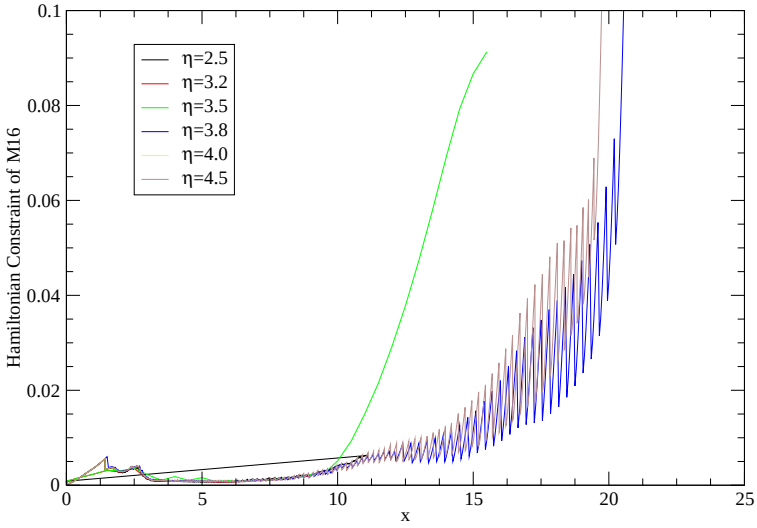


Figure 6.29: L2 norm of Hamiltonian constraint for evolutions of M16 with varying $\eta$ parameter. The different growth rates of the horizon radii allow for a larger excision region, cutting away the numerical errors within the horizon and reducing the overall norm. However, choosing $\eta$ too large or too low the run will crash.

distance of the two black holes (with the same mass, angular momentum etc.) this does not mean they are on similar places in the four dimensional spacetime. This is already a problem when using the same decomposition but different momenta, because the momenta (as can be seen for example in Eq. (3.29)) will change the extrinsic curvature and therefore the slicing. So comparing different initial data sets has to be done very carefully. The following sections intend to do a comparison of puncture and Thin Sandwich (Meudon) data.

### Distances

As explained in section 4.5.3 the distance measurement used here differs from the usually used one in idea and outcome. To see the difference between the straight line measurement and the geodesic measurement the Fig. (6.30) contains both the straight line and the geodesic measurement. The plot shows the behavior of the separation of two black holes during a Meudon data evolution (M12). The initial

difference between the two ways is about 3 or 30% of the measured distance!

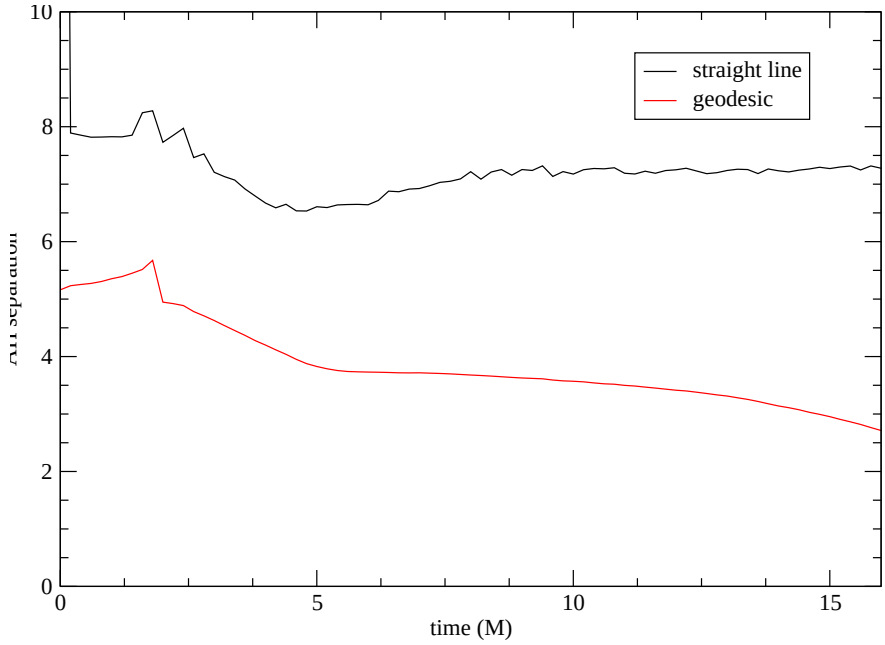


Figure 6.30: Distance measurement. The straight line measurement gives a value about 30% larger than the geodesic measurement.

The difference of the distance measurements shows another fact: using the straight line measurement also the change of distance can be misleading. In the figure it is clearly going up whereas it goes down for the geodesic measurement.

Note that after some initial turbulence of about 5M the distance it levels off more or less. The leveling could be used to determine whether a data set is in circular orbit. In Fig. (6.31) the (geodesic) distance of several Puncture data runs are plotted. The initial linear momentum parameter P was varied between 0.1 and 0.7. The value Cook determined (0.333191749) for this data set is included as well. At first one can notice that the initial separations are not equal. As mentioned above the P parameter is not only changing the linear momentum but also the mass of the black hole, and thus its area and radius.

As expected one can see also that (after an initial turbulence that seems to be

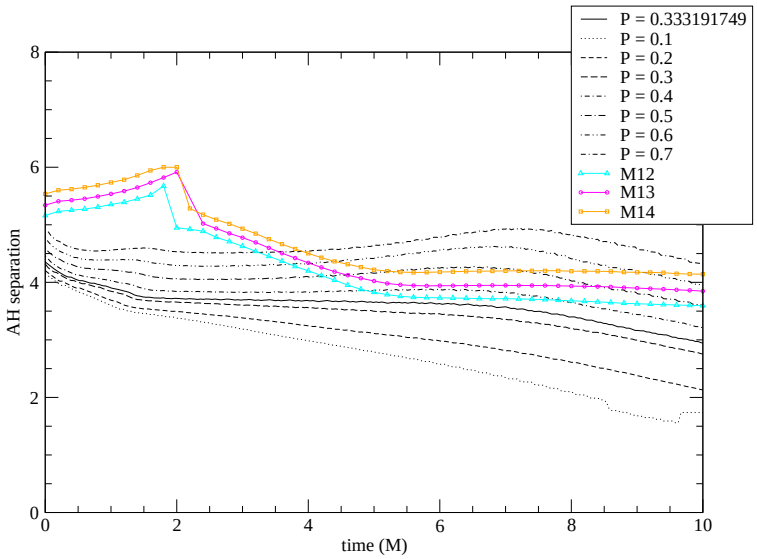


Figure 6.31: Distance measurement of puncture data with varying P parameter and Meudon Data. The initial distance drops for Puncture data and grows for Meudon data because the individual horizons grow (or shrink). The run with the most constant separation has the linear momentum determined by Cook. The Meudon data runs flatten later but stay flat much longer.

needed for all data sets to settle) the separations of the black holes increase or decrease depending on their linear momentum. (Recall that in this configuration the linear momentum was set to point perpendicular to the line connecting the two black holes.) The runs that had the "most horizontal" plateau (and therefore the most circular orbit) was the one determined by Cook. The Meudon data show a similar behavior: After the initial transient is gone (which takes longer for the Meudon data) they level off and stay leveled for much longer than the Puncture data indicating that they are in a more stable circular orbit.

One of the techniques to keep an evolution stable is to reduce the dynamics in the evolution variables as far possible. This is achieved by choosing a suitable gauge. But apart from the gauge the initial time derivative is of crucial importance. Recall that in Fig. (6.13) the initial time derivative of the (traceless) extrinsic curvature was indicating already what the evolutions confirmed later, namely which of the (non

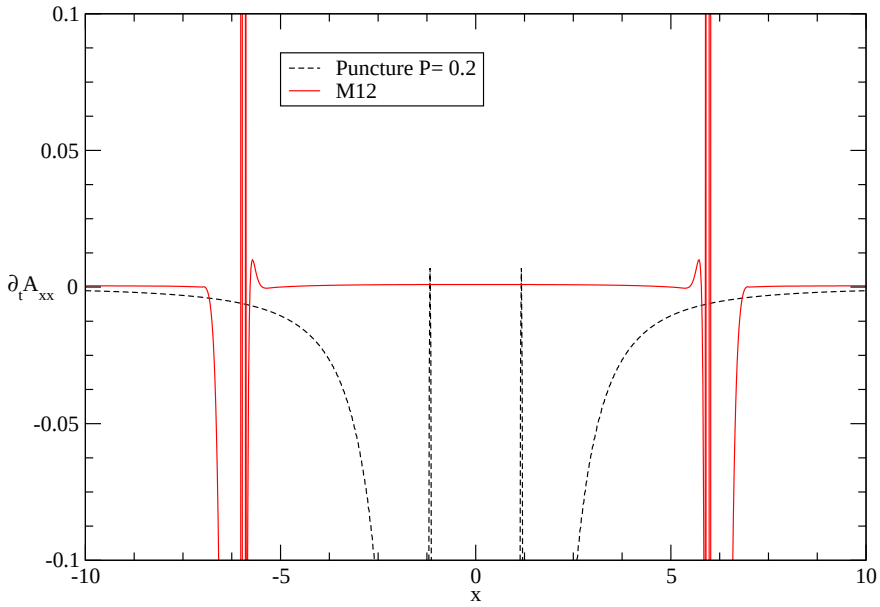


Figure 6.32: Time derivative of the extrinsic (trace-free) curvature for Meudon Data and Puncture data with varying P parameter.

negative) lapse profiles was best in evolving the data. Therefore comparing initial time derivatives can show in which data set the initial evolution was reduced most. In Fig. (6.32) such a comparison is shown. plotted is the initial time derivative of the extrinsic curvature component $A_{xx}$ for puncture data and for Meudon data. The resolution in both cases is 0.2M. It can be seen clearly that - except inside the horizons - the time derivative of the Meudon Data is much smaller. This is expected since one of the principles of the construction of the Meudon data is the assumption of a helical killing vector.

### Merger Times

As explained in chapter 5 at the AEI research was done on what data sets of the Cook sequence take how long to build a common horizon. This can of course be done for the Meudon data as well. For the three sets that created common horizons during their evolution, the times are plotted in Fig. (6.33).

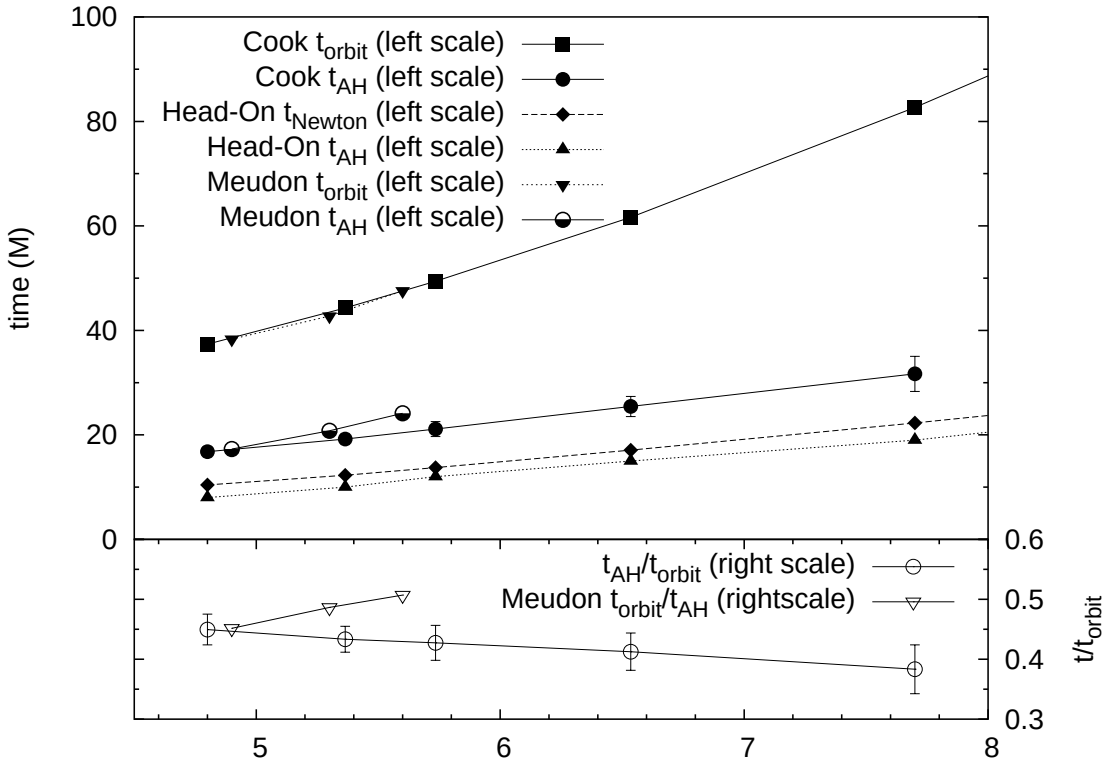


Figure 6.33: Merger Times for several sets of initial data. Puncture data follow the line of free fall data whereas the Meudon data merger times follow a somewhat steeper curve indicating that their setting is closer to a circular orbit. Lower: The fraction of the orbital period the data evolve before they merge is shrinking for Puncture data but growing for Meudon data (with increasing separation).

This plot suggests that for the Meudon data the common horizons are found at times that behave more as expected. The line is steeper than the puncture data merger time line. One could draw the conclusion, that this indicates a better circularity of the data's initial orbit. However, a much more thorough investigation is needed to say something as strong a that. Neither the influence of the boundary could be tested nor the resolution or gauge dependency.

## 6.5 Summary

This chapter introduced a new type of initial data (as done by [77, 78]), reported on evolutions of these data that led to a merger of the black holes, showed differences between different sets of these data and between the Meudon data and Puncture data.

It was shown that the initial data import technique converges to second order to the spectral solution. There is a jump at the horizon location that could be resolved with the finite differenced data. Using a very high resolution one can resolve the numerical error of the spectral coefficients (Fig. (6.23)).

It was also shown that the gauges suggested by the Meudon group could be used for numerical evolutions. But to do so the negative lapse within the horizon had to be set to zero. Otherwise the suggested profiles were taken as the initial data for the gauge quantities (using the isometry mapping to fill the interior of the holes). The $\Gamma$-driver evolution equation (Eq. (2.39)) used for these runs does not seem to be compatible with the Meudon shift. The shift undergoes a rapid change and after approximately 6M settled onto a different profile, familiar to that of Puncture evolutions. This dynamical settling phase is seen in all gauge and the horizon quantities. It seems to be needed to radiate the transient away.

The evolutions could track the individual horizons very well, even though it seems that for the first 1.5M an inner horizon is tracked. It was shown that the horizon masses can be held essentially constant over the entire evolution, to below 2% of drift

as shown in Fig. (6.15). This accuracy is achieved even though there is a great deal of noise in the constraints in the neighborhood of the horizons indicating that the evolution is not entirely clean.

A comparison of the higher resolution data sets with the lower one showed that the resolution of the data sets with only 21 co-location points is already high enough for the use in finite difference codes at resolutions used nowadays. The individual sets show only little difference in their evolutionary behavior. For all of them the apparent horizon radii grow (after an initial decrease) allowing excision to keep the constraint violation down. The common horizons are found at times 18M for M12, at 21M for M13 and at 23.7M for M14. However, it could not be tested how much these times depend on resolution, boundary effects or gauge. The set M16 could not be evolved to merger because the constraint violation was growing too fast so that after a certain time -depending on the gauge chosen- the metric functions and the gauges were distorted too much for the code to handle.

A comparison of these data with Puncture data has shown considerable differences. The time derivative of the evolution variables at initial time is much smaller for the Meudon data leading to a much more stable evolution (see Fig. (6.32)). The distance measurement gave a constant distance for a longer period of time for the Meudon data indicating that the circularity is preserved better than in the Puncture data evolutions.

This results in a sequence of merger times for the Meudon data which follows a more expected trend. Contrary to the Puncture data, the Meudon data evolve for a longer fraction of an orbit and with a faster growing fraction as one moves out in the initial separation sequence. Even though only data sets inside the ISCO could be evolved to merger, the trend could become even stronger once data sets outside the ISCO (proper separation of 6.6M) can be led to merger. Assuming a linear growth of the merger time one can estimate the fraction of an orbital period at the ISCO to

be roughly 60%. This would agree with Post-Newtonian estimates which also suggest that the plunge phase should last for 60% of an orbit [51]. One should note that the linear assumption probably underestimates the actual trend which one would expect to grow faster when moving to a weaker field.

# Chapter 7

# Conclusions

## 7.1 Summary

This aim of this thesis was to contribute to the solution of the problem of finding astrophysically relevant initial data for numerical binary black hole evolutions. The main idea was to compare different initial data construction procedures in terms of their evolutionary behavior. Puncture (Brandt-Brügmann) data [46] and Thin Sandwich data in form of the data developed by the group in Meudon [77, 78] were taken as the initial data, evolved to merger and physical quantities extracted.

To use the Meudon data in finite difference evolutions the interior of the black holes (not given in the original Meudon data sets) was filled using an isometry condition. The complete data spread onto the finite difference grid was shown to converge to second order to the spectral solution (see Fig. (6.24)).

For the Meudon data it could be shown that the gauge suggested by the construction and extended via an isometry transformation is not suited for numerical evolutions. However, of several different initial gauge profiles one could be isolated as leading to stable longterm evolutions: the gauge profile suggested by the construction used outside the black holes and a constant zero lapse profile inside. For the shift the initial profile extended by the isometry transformation could be used, though it is not entirely compatible with the $\Gamma$-driver conditions which are commonly employed,

and this results in a strongly dynamical phase at the beginning.

Using these initial gauge conditions and evolving them with the live gauges Γ-driver (Eq. (2.39)) for the shift and 1+log (Eqs. (2.30) and (2.31)) for the lapse (see chapter 2) several of the Meudon data could be evolved to merger (M12, M13, and M14). The horizon mass could be held constant with an error below 2% during all of these evolutions.

The Meudon data sets that formed a common horizon did so within a time different from comparable Puncture data sets (see Fig. (6.33)). With a growing initial separation the Meudon data evolved for a longer time before forming a common horizon. Moreover, the fraction of the orbital period is increasing with the initial separation. (see table 7.1). This is contrary to the Puncture data where this fraction actually seems to decrease with the initial separation of the black holes for the employed gauges. However, only three of the Meudon data sets could be lead to merger. Due to lack of recourses a convergence test could not be done. The dependency on boundary effects and different gauge parameters has to be quantified before any strict statement about the circularity of these orbits can be made, though the demonstrated trend is in better agreement with intuition.

The method of drift-correction was introduced and successfully used in Puncture data runs. Comparing the locations of the individual apparent horizons it could be shown that the Meudon data could profit from the drift-correct method as well.

A new way to measure the separation of two horizons was introduced. This method uses - contrary to the straight line measure employed until now - a geodesic to compute the proper distance. It could be shown that the difference between these measurements is non-trivial and grows for systems with larger angular momentum. This amounts to about 1% for a Puncture data set (QC0) with the linear momentum parameter $P$ raised to 0.5 and about 30% for the Meudon data (M12).

In addition to the evolutions described here, in chapter 3.5 a new initial data set was

| Name | proper distance | merger time | fraction of orbit |
|---|---|---|---|
| QC0 | 4.99 | 16.8 | 0.450 |
| QC1 | 5.49 | 19.2 | 0.433 |
| QC2 | 5.86 | 21.1 | 0.427 |
| QC3 | 6.67 | 25.4 | 0.413 |
| M12 | 4.95863 | 17.30 | 0.452 |
| M13 | 5.30006 | 20.79 | 0.486 |
| M14 | 5.63471 | 24.13 | 0.507 |

Table 7.1: Merger times of Puncture and Meudon data. With increasing initial separation the merger times increase but the fraction of an orbital period decreases for both of the initial data types.

developed that is not relying on a conformal decomposition of the variables. Instead it uses a Kerr-Schild-like ansatz (Eq. (3.51)). The treatment of the inner boundary allows this data set in principle to use a trivial topology (all of the other initial data mentioned here have a nontrivial one as for example the two-sheeted one shown in Fig. (3.3)) and therefore a possible candidate for a astrophysically realistic data set. The new data could be shown to converge for a single perturbed non-rotating black hole. The solution agrees with a solution of the linearized problem. The method allows for a more general setting as for instance two black holes in head-on collision, and will be extended to solve this system as well.

## 7.2 Outlook

As mentioned throughout this thesis there is much room for improvements on all sides of the task. Many have been tried already, some of them with great success, some with less. Here a few ideas will be presented on how to proceed. It is by far not clear which things will help most (otherwise the community would have done most of them despite their possible complexness).

### 7.2.1 Mesh Refinement

Probably one of the most promising new techniques is mesh refinement. All over this thesis remarks have been made that higher resolution could improve results and that problems with the outer boundary could be reduced immensely if they were put further out. To get the merger times un-effected by boundary errors they should at least be put at a distance such that they cannot causally influence the black holes before they merge. Additionally this would also improve extraction of physical quantities because many of them are defined at infinity and converge only slowly to the infinity value with increasing radius. As simple computation could show the needs:

A Meudon data run needs at least a resolution of 0.1 at the black holes. The smallest data set (M12) merges at coordinate time 90 (recall that the ADM mass is roughly 5 for these data sets). So the boundaries should at least $90/5 = 18M$ far away from the black hole, which is located at $\pm 6$. This means that the boundary has to be 980 grid-points away from the origin. This leads to a bitant grid size of $980 \times 980 \times 590$. Doing a computation similar to the one in section 6.3 (using 120 grid-functions and double precision) this amounts in 5.9 TByte, a requirement none of todays supercomputers can fulfill.

A solution would be to use mesh refinement. The idea is simple: where there is higher resolution needed one uses it. But where it is not needed one does not use it. Especially in systems with compact objects as neutron stars or black holes there are regions where high resolution is needed but the boundaries have to be put far into the wave zone, a region where a much coarser resolution is sufficient. So mesh refinement will enable the runs to use much higher resolution with a much lower requirement on memory and runtime. Such a technique was implemented into *Cactus* [102] under the name "Carpet". For now it uses only fixed mesh refinement (the high resolution patches cannot move or change during the evolution with changed requirements).

But first runs are done and have been very successful. The initial data set M12 (see chapter 6) was set up using seven layers of refinement. The resulting metric is shown in Fig. (7.1).

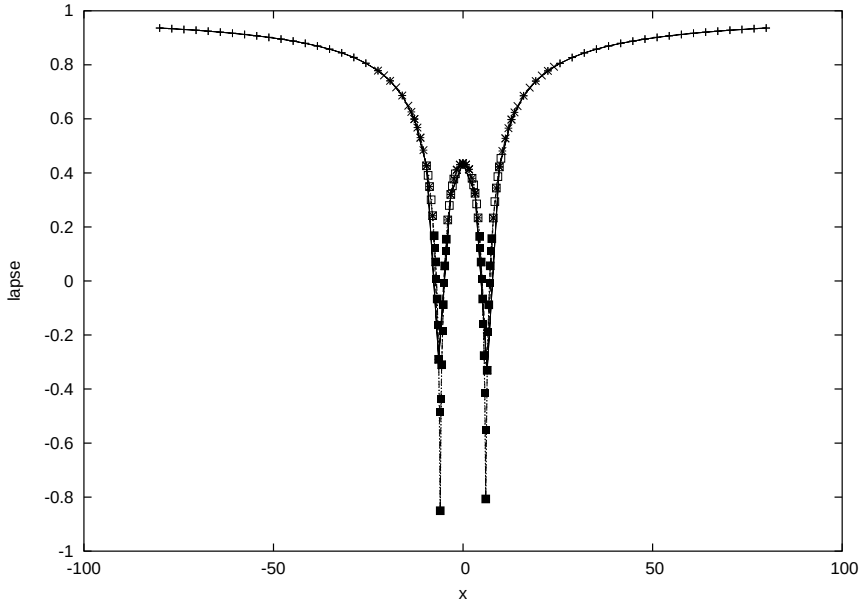


Figure 7.1: Lapse function of Meudon initial data set M12 set up on "Carpet" using five levels of refinement. The interior resolution is put to 0.02 but nevertheless the boundary could be placed at ±80M.

This technique will further improve the runs and make runs possible that tare very important, as for instance convergence tests on merger times of Meudon data with the boundaries put far enough out to causally disconnect them from the merger.

### 7.2.2 Gauge Parameters

One of the immediate things to improve one can think of is the gauges. Using the newly developed gauges the AEI group described in sections 2.4.1 and 2.4.2 had tremendous success evolving binary black holes. This method could be used to further improve the quality of the runs. This could be done either by fine tuning the parameters or by improving the equations governing the evolution of the gauges. With

the help of a faster elliptic solver it could become possible to use the original elliptic equations for a maximal slicing lapse and a minimal distortion shift. Brügmann et al. [50] have shown that it is possible to find a gauge for puncture data that will co-rotate with the data and lead to a stable evolution for more than 100 M even for binary black holes. This will be tried in the near future. Another idea is referring to the tests done with the Meudon data lapse profile to improve its behavior during numerical evolutions (compare section 6.4.3). A similar method could be used to change the shift. As can be seen in Fig. (6.7) the initial Meudon shift profile does not have an outward pointing component. This may be a reason for problems that could be cured by a suitable change of the shift.

### 7.2.3 Drift-correction

The co-rotation mechanism introduced in section 2.4.3 depends on the apparent horizons. One of the ideas to improve the code is to use an iso-surface of some other function. A possible candidate is the lapse because experience shows that if an black hole appears the lapse has a value close to 0.3. So using an iso-surface of 0.3 could improve at least the speed of the code. But it could also be used in a slightly different way: instead of tracking only a point (the centroid of the horizons or iso-surfaces) and adjusting the shift to get a rigid co-rotation, this technique could be used to adjust all components of the shift to minimize the distortion or the evolution of other functions. Of course the three components of the shift are not enough to freeze the evolution of all the six metric components, but a certain minimization could be achieved.

The only part that may not be good enough in the shift treatment is the (increasing) rotation speed. During the evolution the black holes will approach each other increasing the rotation speed. Some of the angular momentum will be radiated away, so it cannot be taken to be constant, but the radiation will not suffice to keep the angular frequency constant. Looking at Fig. (7.3) (left) one sees that the centroids

of the numerically found horizons rotate through the grid over the evolution time. This may be responsible for some of the trouble found when evolving this system. Sooner or later the horizon will hit the excision region (which is, by construction, not moving) and soon after, the run crashes. To avoid this, the "drift-correct" method mentioned in section 2.4.3 can be used: the centroids are tracked (exactly as one sees for Meudon data in Fig. (7.2)) and the shift is given a kick to rotate with the centroids. The result will be a picture like Fig. (7.3)(left). This technique was up to now only applied to puncture data evolutions. It could lead to a considerable improvement for the stability of the Meudon data runs as well since (as can be seen in Fig. (7.2) the centroids as well as the common horizon have rotated for almost a quarter of an orbit.

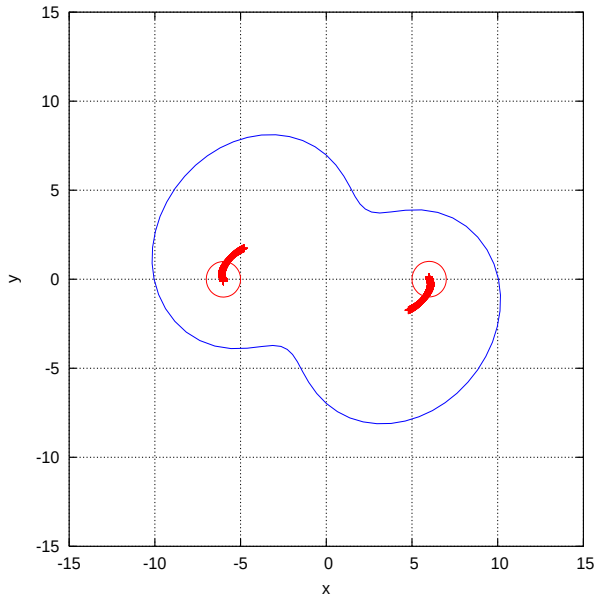


Figure 7.2: Movement of centroids of horizons for Meudon data evolution without drift correction. The initial horizons and the common horizon at the time it appears are drawn as well. The horizons rotate for almost a quarter of an orbit.

Another idea is to use drift-correction also in the radial direction. The shift vector could not only be adjusted to keep the grid rotating with the system, but also to

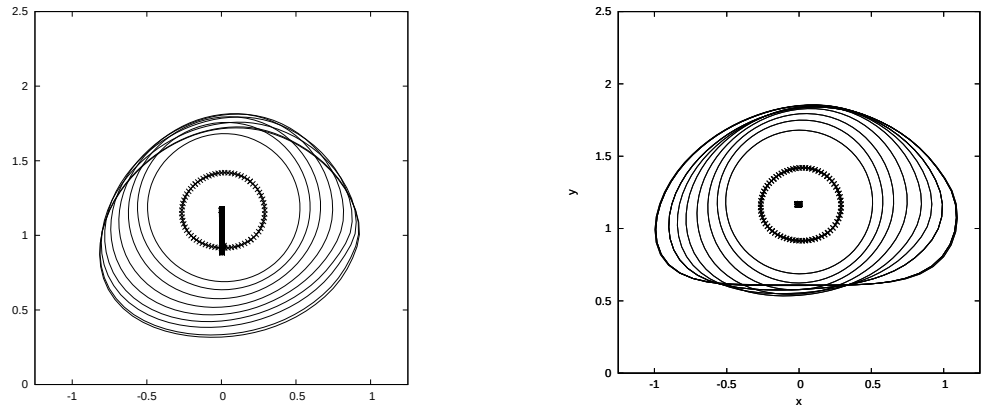


Figure 7.3: Horizon locations of Puncture data run using an angular drift-correction (left) and an additional angular one (right). The initial horizon is drawn with a crossed line and the final one with a thick line. The horizon centroid is plotted as well, but does not move much during the evolution. As can be seen the horizons stay put but become deformed after a certain time. This could lead to problems finding it.

regulate the horizon location directly (other than to do it via an evolution equation). First results using this technique were obtained already and look very promising [50, 67]. Comparing the left plot of Fig. (7.3) with the right plot one can clearly see the possible improvements. The horizons can be kept in place much more accurate making much longer evolutions possible. However, using this shift condition the horizon shapes became deformed. This could lead to problems finding it numerically.

### 7.2.4 Formulations

All runs for this paper have been done using the BSSN formulation (compare chapter 2.3.2). This method has been shown to work much better than the original ADM formulation but it is still quite unclear why. To have a better handle on the mathematics involved and on the numerical behavior of the evolution scheme many suggestions of different schemes were made. Currently quite some effort is done in the AEI group to create a first order version of BSSN, for instance. To come up with a definite answer to what is the best possible evolution system a series of test was developed [9]. They

start with relatively easy evolutions of gauge waves (flat space in a wave coordinate system) and go on to evolutions of Brill waves, axisymmetric gravitational waves, a physical system that proved to be very difficult to handle numerically. These test were agreed on by a large part of the community. Still there is no definite answer but currently codes are tested using them. When an answer is found this evolution system will certainly be tried and there is justified hope that this will improve the runs largely.

### 7.2.5 Excision

One of the most compelling ideas on how to deal with singularities still is excision described in detail in 4.4. However, putting an excision boundary into a region with large values of all physical quantities raises the question of the boundary conditions. The simple copying of the values across the boundary that is used until now has shown tremendous success but is certainly not the best choice possible. But it is quite hard to find a better one. All theoretical treatments of the boundary problem rely on the smallness of the fields, an assumption certainly not true inside of black holes. The errors made in current evolutions are usually swallowed by a growing excision region (points falling into the black hole will make its radius grow in coordinate space, thereby increasing the region of possible excision). This is helping a lot but it is not a good solution because this way sooner or later the entire grid is excised.

Another, a much cleaner and more appropriate solution would be to use the causal structure of the spacetime. Inside a black hole the light cone is tilted inwards (by definition, because otherwise light could leave the horizon and it would not be a black hole). If the numerical method was aware of that, no boundary was needed because to update a point at the boundary only information further out was used. This idea is called "causal differencing" [22]. It was used in easier settings (especially in lower dimensions) but is not anymore due to the complicate handling. But very recently

the AEI group started working on that issue and hopefully the will be some tests soon.

Other groups are using grid patches of spherical coordinates around the black hole which makes it much easier to implement a better boundary condition. Further away from the boundary the values are then interpolated back onto the Cartesian grid used in Cactus. This method has been shown to work and is now in the testing phase. Within the AEI a similar work was started, collaboration has begun and soon this technique will be tried in regular evolutions using Cactus.

### 7.2.6 Boundaries

At the outer boundaries the problems are different. The fields are supposedly small and the causal structure is that of flat space. This means that causal differencing will not help. The outer boundary is a time-like surface in spacetime. So any space-like hypersurface (any of the slices used here) will cut it. This problem is treated extensively in the literature. But usually these treatments simplify the problem to scalar waves. For those scalar waves and specified angles several solutions have been found and there is extensive research underway to test these boundary conditions in generic runs, where there are nonlinear waves at several different incidence angles. Expectations are high that one or the other of theses suggested techniques will lead to substantially better results.

# Appendix A

# Cauchy Split

Assuming that it is possible to express the 4 dimensional manifold as $R^3 \otimes R$, we are able to slice it into 3 dimensional subspaces labeled by a real number called time. Once this split is done, it is useful to define a unit vector $n^\alpha$ normal to the slice and use it to construct a projection tensor:

$$h^{\alpha\beta} = g^{\alpha\beta} + n^{\alpha\beta}. \tag{A.1}$$

Applying this to the 4-metric on gets the 3 dimensional metric intrinsic to the slice is defined (it turns out to be just the spatial part of the 4 dimensional one):

$$\gamma^{ab} = h^a{}_\mu h^b{}_\nu g^{\mu\nu}. \tag{A.1}$$

Now one has to notice that the covariant derivative built with the 3 metric is just the projection of the one built with the 4 metric:

$$v^a{}_{|b} = h^a{}_\mu h^\nu{}_b v^\mu{}_{;\nu}, \tag{A.2}$$

where | is denoting the covariant derivative constructed with the 3 metric.

For the derivation of the 3+1 version of Einstein's equations it is necessary to use the Gauss-Codazzi equations. To derive them one has to look at the split of the covariant derivative of a vector $T^\alpha$ orthogonal to $n^\alpha$:

$$T_{\alpha;\beta} = h^\lambda{}_\alpha h^\gamma{}_\beta T_{\lambda;\gamma} + n_\beta \dot{T}_\gamma h^\gamma{}_\alpha + n_\alpha T^\gamma K_{\gamma\beta} - n_\alpha n_\beta T^\gamma \dot{n}_\gamma. \tag{A.2}$$

Applied to the projection tensor this gives:

$$h_{\alpha\beta;\gamma} = -(\dot{n}_\alpha n_\beta)n_\gamma + K_{\alpha\gamma}n_\beta + K_{\beta\gamma}n_\alpha. \tag{A.3}$$

To compute the Gauss-Codazzi equations one has to look at the definition of the curvature tensor using the normal vector $n^\alpha$ and project it to the slice:

$$\begin{aligned} R^\alpha{}_{\beta\gamma\delta}n_\alpha &= n_{\beta;\gamma\delta} - n_{\beta;\delta\gamma} \\ R^\alpha{}_{\beta\gamma\delta}n_\alpha h^\beta{}_\epsilon h^\gamma{}_\phi h^\delta{}_\lambda &= (n_{\beta;\gamma\delta} - n_{\beta;\delta\gamma})h^\beta{}_\epsilon h^\gamma{}_\phi h^\delta{}_\lambda. \end{aligned} \tag{A.4}$$

Now using eq.(A.3) one can write

$$\begin{aligned} R^\alpha{}_{\beta\gamma\delta}n_\alpha h^\beta{}_\epsilon h^\gamma{}_\phi h^\delta{}_\lambda &= \left((n_{\beta;\kappa}h^\kappa{}_\gamma)_{;\delta} - (n_{\beta;\kappa}h^\kappa{}_\delta)_{;\gamma})\right) h^\beta{}_\epsilon h^\gamma{}_\phi h^\delta{}_\lambda \\ &= \left(K_{\beta\delta;\gamma} - K_{\beta\gamma;\delta}\right) h^\beta{}_\epsilon h^\gamma{}_\phi h^\delta{}_\lambda \\ &= \left(K_{bd|g} - K_{bg|d}\right) h^b{}_\epsilon h^g{}_\phi h^d{}_\lambda, \end{aligned} \tag{A.5}$$

which leads to the Gauss-Codazzi equation:

$$R^\alpha{}_{bgd}n_\alpha = \left(K_{bd|g} - K_{bg|d}\right). \tag{A.6}$$

Similarly , projecting all four indices down to the slice, one gets:

$$R^\alpha{}_{bgd} = R_{abcd} + K_{ac}K_{bd} - K_{ad}Kbc. \tag{A.7}$$

Inserting these equations into Einstein's equations, one gets

$$R + K^2 + K_{ab}K^{ab} = 0 \qquad \text{and} \tag{A.8}$$

$$D_b(K^{ab} - \gamma^{ab}K) = 0. \tag{A.9}$$

# Appendix B

# Bianchi Identities

The Bianchi-identities answer the question whether a given tensor (with the correct symmetries) can be a Riemannian curvature tensor of a metric. To find a metric from a given curvature tensor one has to solve 20 differential equations (the defining equations for $R_{\alpha\beta\gamma\delta}$) for the 10 metric components. This usually gives a solution only if certain integrability conditions are obeyed:

$$R_{\alpha\beta<\gamma\delta;\epsilon>} \equiv R_{\alpha\beta\gamma\delta;\epsilon} + R_{\alpha\beta\delta\epsilon;\gamma} + R_{\alpha\beta\epsilon\gamma;\delta} = 0 \qquad (B.1)$$

multiplying by $g^{\alpha\delta}$ and $g^{\beta\epsilon}$ and using the symmetry properties of $R_{\alpha\beta\gamma\delta;\epsilon}$ gives:

$$g^{\alpha\epsilon}g^{\beta\delta}R_{\alpha\beta<\gamma\delta;\epsilon>} = R^{\epsilon}_{\gamma;\epsilon} - R_{;\gamma} + R^{\epsilon}{}_{\gamma;\epsilon} \qquad (B.2)$$

and therefore

$$\left(R^{\epsilon\gamma} - \frac{1}{2}g^{\epsilon\gamma}R\right)_{;\epsilon} = 0 \qquad (B.3)$$

This is a very important consequence for the entire theory: a mathematical property of the curvature tensor ensure the vanishing of the divergence of the Einstein tensor. This via Einstein's equations ensures the vanishing divergence of the matter tensor, which is the equation of motion. So a mathematical property of the spacetime fixes the equation of motion. Einstein's intent when creating the General Relativity Theory was the opposite. Following Mach's ideas the matter content of the universe should fix the spacetime. This problem haunted Einstein for quite a while. It could be

shown much later [43] that Einstein's idea of general covariance cannot be used when Mach's idea of matter fixing spacetime is used at the same time. Therefore research is underway, checking if either one of these ideas can be weakened to create a theory able to accommodate both of the ideas.

## their role in the constraints

The Bianchi-identities also have a very important consequence for the constraints: Writing them as

$$G^{\alpha}_{\beta;\alpha} = 0 \tag{B.4}$$

and using the projection tensor $h_{\mu\nu} = g_{\mu\nu} - n_\mu n_\nu$ will give

$G^{\alpha}_{\beta;\alpha} = 0$

$$\left(\left(h^{\alpha}_{\gamma} + n^{\alpha}n_{\gamma}\right)G^{\gamma}_{\beta}\right)_{;\alpha} = 0$$

$$\left(h^{\alpha}_{\gamma}G^{\gamma}_{\beta}\right)_{;\alpha} + \left(n_{\gamma}G^{\gamma}_{\beta}\right)_{;\alpha} n^{\alpha} + \left(n_{\gamma}G^{\gamma}_{\beta}\right) n^{\alpha}_{;\alpha} = 0$$

$$-\left(n_{\gamma}G^{\gamma}_{\beta}\right)_{;\alpha} n^{\alpha} = \left(h^{\alpha}_{\gamma}G^{\gamma}_{\beta}\right)_{;\alpha} + \left(n_{\gamma}G^{\gamma}_{\beta}\right) n^{\alpha}_{;\alpha}$$

So if the constraints $n_\gamma G^\gamma_\beta$ are solved initially and the evolution equations $h^\alpha_\gamma G^\gamma_\beta$ are solved everywhere in space one has $\left(n_\gamma G^\gamma_\beta\right)_{;\alpha} n^\alpha = 0$ . The covariant derivative of the constraints normal to the hypersurface vanishes and there are no higher derivatives. Therefore, if the constraints are fulfilled once, the evolution equations and the Bianchi identities will ensure they are fulfilled always. Sad enough numerical errors will make none of the terms really vanish. So it is an area of very active research how to diminish errors either by changing the equations (for instance adding terms consisting in multiples of the constraints, that are analytically zero but change the numerical behavior of the equations) or by using more accurate numerical methods.

# Appendix C

# Lie Derivatives

The Lie derivative is a very important tool for many quite different applications. It gives the change of a geometrical object that is moved along a vector $v^\mu$ (for the infinitesimal distance $\epsilon$) with respect to the coordinates system at the starting point. This is in fact a coordinate transformation:

$$x \Rightarrow x^{\mu\prime} = x^\mu - \epsilon v^\mu, \tag{C.1}$$

with the Jacobian

$$A^\mu{}_\nu = \delta^\mu{}_\nu - \epsilon v^\mu{}_{;\nu}. \tag{C.2}$$

Take as an example a vector $T^\nu$. At the new point it's components will be

$$T^\mu(P') = T^\mu(P) + \epsilon T^\mu{}_{;\nu}(P) v^\nu \tag{C.3}$$

In the coordinates from the starting point this is

$$T^\mu(P') = A^\mu{}_\nu (T^\nu(P) + \epsilon T^\nu{}_{;\alpha}(P) v^\alpha) \tag{C.4}$$

$$T^\mu(P') = (\delta^\mu{}_\nu - \epsilon v^\mu{}_{;\nu})(T^\nu(P) + \epsilon T^\nu{}_{;\alpha}(P) v^\alpha) \tag{C.5}$$

$$T^\mu(P') = T^\mu(P) + \epsilon T^\mu{}_{;\alpha}(P) v^\alpha - \epsilon T^\alpha(P) v^\mu{}_{;\alpha}, \tag{C.6}$$

where the last equation used terms up to linear order in $\epsilon$.

The Lie derivative now is defined to be

$$\mathcal{L}_v T^\nu := \lim_{\epsilon \to 0} \frac{1}{\epsilon} \left( T^\mu(P') - T^\mu(P) \right) \tag{C.7}$$

or because of C

$$\mathcal{L}_v T^\mu := T^\mu_{,\nu} v^\nu - T^\nu v^\mu{}_{,\nu}. \tag{C.8}$$

$$\mathcal{L}_v T_\mu := T_{\mu,\nu} v^\nu + T_\nu v^\nu{}_{,\mu}. \tag{C.9}$$

The same reasoning leads to the expressions for covariant components of vectors and for higher rank tensors (as for example the metric):

$$\mathcal{L}_v g_{\mu\nu} := g_{\mu\nu,\alpha} v^\alpha + g_{\alpha\nu} v^\alpha{}_{,\mu} + g_{\mu\alpha} v^\alpha{}_{,\nu}. \tag{C.10}$$

It is easy to show that this definition is independent of the derivative used. So for example using the covariant derivative, one gets:

$$\mathcal{L}_v g_{\mu\nu} = g_{\mu\nu,\alpha} v^\alpha + g_{\alpha\nu} v^\alpha{}_{,\mu} + g_{\mu\alpha} v^\alpha{}_{,\nu} \tag{C.11}$$

$$= (g_{\mu\nu;\alpha} + \Gamma^\sigma{}_{\mu\alpha} g_{\sigma\nu} + \Gamma^\sigma{}_{\nu\alpha} g_{\mu\sigma} v^\alpha) \tag{C.12}$$

$$+ g_{\alpha\nu}(v^\alpha{}_{\mu} - \Gamma^\alpha_{\sigma\mu} v^\sigma) + g_{\mu\alpha}(v^\alpha{}_{\nu} - \Gamma^\alpha{}_{\sigma\nu} v^\sigma) \tag{C.13}$$

$$= v^\alpha g_{\mu\nu;\alpha} + g_{\alpha\nu} v^\alpha{}_{;\mu} + g_{\mu\alpha} v^\alpha{}_{;\nu}, \tag{C.14}$$

which in the case of the metric reduces to

$$\mathcal{L}_v g_{\mu\nu} = g_{\alpha\nu} v^\alpha{}_{;\mu} + g_{\mu\alpha} v^\alpha{}_{;\nu} = v_{\nu;\mu} + v_{\mu;\nu} \tag{C.15}$$

since the covariant derivative of the metric vanishes.

There are some other useful properties of the Lie derivative:

- it follows the Leibniz rule
- it commutes with ... and partial derivative
- if partial derivatives vanish, Lie derivative and regular directional derivative are the same

If the Lie derivative of a metric with respect to a vector $v^\mu$ vanishes, this vector is generating a symmetry of the metric. It is therefore very important when one checks global properties of the metric. Such a vector is called killing vector. It has to obey killings equation:

$$\mathcal{L}_v g_{\mu\nu} := g_{\alpha\nu} v^\alpha{}_{;\mu} + g_{\mu\alpha} v^\alpha{}_{;\nu} = 0 \tag{C.16}$$

or in other words

$$v_{\mu;\nu} + v_{\nu;\mu} = 0. \tag{C.17}$$

# Bibliography


[1] A. Abrahams and R. Price. Black-hole collisions from Brill-Lindquist initial data: Predictions of perturbation theory. *Phys. Rev. D*, 53:1972–1976, 1996.

[2] M. Alcubierre. The appearance of coordinate shocks in hyperbolic formulations of general relativity. *Phys. Rev. D*, 55:5981–5991, 1997.

[3] M. Alcubierre, G. Allen, B. Brügmann, E. Seidel, and W.-M. Suen. Towards an understanding of the stability properties of the 3+1 evolution equations in general relativity. *Phys. Rev. D*, 62:124011, 2000.

[4] M. Alcubierre, W. Benger, B. Brügmann, G. Lanfermann, L. Nerger, E. Seidel, and R. Takahashi. 3D Grazing Collision of Two Black Holes. *Phys. Rev. Lett.*, 87:271103, 2001.

[5] M. Alcubierre, S. Brandt, B. Brügmann, C. Gundlach, J. Massó, E. Seidel, and P. Walker. Test-beds and applications for apparent horizon finders in numerical relativity. *Class. Quantum Grav.*, 17:2159–2190, 2000.

[6] M. Alcubierre and B. Brügmann. Simple excision of a black hole in 3+1 numerical relativity. *Phys. Rev. D*, 63:104006, 2001.

[7] M. Alcubierre, B. Brügmann, M. Miller, and W.-M. Suen. A conformal hyperbolic formulation of the Einstein equations. *Phys. Rev. D*, 60:064017, 1999.

[8] M. Alcubierre and J. Massó. Pathologies of hyperbolic gauges in general relativity and other field theories. *Phys. Rev. D*, 57(8):4511–4515, 1998.

[9] Miguel Alcubierre, Gabrielle Allen, Thomas W. Baumgarte, Carles Bona, David Fiske, Tom Goodale, Francisco Siddhartha Guzmán, Ian Hawke, Scott Hawley, Sascha Husa, Michael Koppitz, Christiane Lechner, Lee Lindblom, Denis Pollney, David Rideout, Marcelo Salgado, Erik Schnetter, Edward Seidel, Hisa aki Shinkai, Deirdre Shoemaker, Bela Szilágyi, Ryoji Takahashi, and Jeffrey Winicour. Towards standard testbeds for numerical relativity. *Class. Quantum Grav.*, 21(2):589–613, 2004.

[10] Miguel Alcubierre, Bernd Brügmann, Peter Diener, Francisco Siddhartha Guzmán, Ian Hawke, Scott Hawley, Frank Herrmann, Michael Koppitz, Denis Pollney, and Edward Seidel. Dynamical Evolution of Cook-Baumgarte ISCO Data. 2003. in preparation.

[11] Miguel Alcubierre, Bernd Brügmann, Peter Diener, Michael Koppitz, Denis Pollney, Edward Seidel, and Ryoji Takahashi. Gauge conditions for long-term numerical black hole evolutions without excision. *Phys. Rev. D*, 67:084023, 2003.

[12] Miguel Alcubierre, Bernd Brügmann, Denis Pollney, Edward Seidel, and Ryoji Takahashi. Black hole excision for dynamic black holes. *Phys. Rev. D*, 64:61501 (R), 2001.

[13] Miguel Alcubierre, Peter Diener, Francisco Siddhartha Guzmán, Scott Hawley, Michael Koppitz, Denis Pollney, and Edward Seidel. Shift Conditions for Orbiting Binaries in Numerical Relativity. 2003. in preparation.

[14] G. Allen, W. Benger, T. Goodale, H. Hege, G. Lanfermann, A. Merzky, T. Radke, E. Seidel, and J. Shalf. The cactus code: A problem solving environment for the grid. In *Proceedings of Ninth IEEE International Symposium*

*on High Performance Distributed Computing, HPDC-9, August 1-4 2000, Pittsburgh*, pages 253–260. IEEE Press, 2000.

[15] G. Allen, T. Dramlitsch, T. Goodale, G. Lanfermann, T. Radke, E. Seidel, T. Kielmann, K. Verstoep, Z. Balaton, P. Kacsuk, F. Szalai, J. Gehring, A. Keller, A. Streit, L. Matyska, M. Ruda, A. Krenek, H. Frese, H. Knipp, A. Merzky, A. Reinefeld, F. Schintke, B. Ludwiczak, J. Nabrzyski, J. Pukacki, H-P. Kersken, and M. Russell. Early experiences with the egrid testbed. In *IEEE International Symposium on Cluster Computing and the Grid, Brisbane, Australia, May 16-18 2001*, 2001. Available at `http://www.cactuscode.org/Papers/CCGrid_2001.pdf.gz`.

[16] G. Allen, T. Goodale, G. Lanfermann, T. Radke, and E. Seidel. The cactus code: A problem solving environment for the grid. In *Proceedings of First Egrid Meeting at ISTHMUS, Poznan, April 2000*, 2000. http://www.zib.de/visual/projects/TIKSL/Papers/EGrid2000-Cactus.ps.

[17] G. Allen, T. Goodale, J. Massó, and E. Seidel. The cactus computational toolkit and using distributed computing to collide neutron stars. In *Proceedings of Eighth IEEE International Symposium on High Performance Distributed Computing, HPDC-8, Redondo Beach, 1999*. IEEE Press, 1999.

[18] G. Allen, T. Goodale, and E. Seidel. The cactus computational collaboratory: Enabling technologies for relativistic astrophysics, and a toolkit for solving pdes by communities in science and engineering. In *7th Symposium on the Frontiers of Massively Parallel Computation-Frontiers 99*, New York, 1999. IEEE.

[19] P. Anninos, D. Bernstein, S. Brandt, Hobill, E. Seidel, and L. Smarr. Dynamics of black hole apparent horizons. *Phys. Rev. D*, 50:3801–3815, 1994.

[20] P. Anninos, K. Camarda, J. Massó, E. Seidel, W.-M. Suen, and J. Towns. Three-dimensional numerical relativity: The evolution of black holes. *Phys. Rev. D*, 52(4):2059–2082, 1995.

[21] P. Anninos, Karen Camarda, Joseph Libson, J. Massó E. Seidel, and W.-M. Suen. Finding apparent horizons in dynamic 3D numerical spacetimes. *Phys. Rev. D*, 58:24003, 1998.

[22] P. Anninos, G. Daues, J. Massó, E. Seidel, and W.-M. Suen. Horizon boundary conditions for black hole spacetimes. *Phys. Rev. D*, 51(10):5562–5578, 1995.

[23] P. Anninos, D. Hobill, E. Seidel, L. Smarr, and W.-M. Suen. Collision of two black holes. *Phys. Rev. Lett.*, 71(18):2851–2854, 1993.

[24] A. Arbona, C. Bona, J. Massó, and J. Stela. Robust evolution system for numerical relativity. *Phys. Rev. D*, 60:104014, 1999. gr-qc/9902053.

[25] R. Arnowitt, S. Deser, and C. W. Misner. The dynamics of general relativity. In L. Witten, editor, *Gravitation: An Introduction to Current Research*, pages 227–265. John Wiley, New York, 1962.

[26] A. Ashtekar and A. Magnon-Ashtekar. On conserved quantities in general relativity. *J. Math. Phys.*, 20(5):793–800, 1979.

[27] J. Baker, B. Brügmann, Manuela Campanelli, C. O. Lousto, and R. Takahashi. Plunge waveforms from inspiralling binary black holes. *Phys. Rev. Lett.*, 87:121103, 2001.

[28] J. Baker and M. Campanelli. Making use of geometrical invariants in black hole collisions. *Phys. Rev. D*, 62:127501, 2000.

[29] J. Baker, M. Campanelli, C. O. Lousto, and R. Takahashi. Modeling gravitational radiation from coalescing binary black holes. *Phys. Rev.*, D65:124012, 2002.

[30] John Baker, Bernd Brügmann, Manuela Campanelli, and Carlos O. Lousto. Gravitational waves from black hole collisions by eclectic computation. *Class. Quantum Grav.*, 17:L149, 2000.

[31] John Baker, Manuela Campanelli, and Carlos O. Lousto. The Lazarus project: A pragmatic approach to binary black hole evolutions. *Phys. Rev.*, D65:044001, 2002.

[32] J. Balakrishna, G. Daues, E. Seidel, W.-M. Suen, M. Tobias, and E. Wang. Coordinate conditions in three-dimensional numerical relativity. *Class. Quantum Grav.*, 13:L135–L142, 1996.

[33] T. W. Baumgarte. Innermost stable circular orbit of binary black holes. *Phys. Rev. D*, 62:024018, 2000.

[34] T. W. Baumgarte and S. L. Shapiro. Numerical integration of Einstein's field equations. *Physical Review D*, 59:024007, 1999.

[35] R. Beig and P. Chrusciel. Killing initial data. *Class. Quantum Grav.*, 14:A83–A92, 1997.

[36] Reimann Bernd. private communication.

[37] N. Bishop, R. Isaacson, M. Maharaj, and J. Winicour. *Phys. Rev. D*, 57:6113, 1998.

[38] L. Blanchet, G. Faye, and B. Ponsot. Gravitational field and equations of motion of compact binaries to 5/2 post-Newtonian order. *Phys. Rev.*, D58:124002, 1998.

[39] Luc Blanchet, Bala R. Iyer, Clifford M. Will, and Alan G. Wiseman. Gravitational wave forms from inspiralling compact binaries to second-post-Newtonian order. *Class. Quantum Grav.*, 13:575–584, 1996.

[40] C. Bona, J. Massó, E. Seidel, and J. Stela. New Formalism for Numerical Relativity. *Phys. Rev. Lett.*, 75:600–603, 1995.

[41] S. Bonazzola, E. Gourgoulhon, and J.-A. Marck. Numerical approach for high precision 3-d relativistic star models. *Phys. Rev. D.*, 58:104020, 1998.

[42] S. Bonazzola, E. Gourgoulhon, and J.-A. Marck. Numerical models of irrotational binary neutron stars in general relativity. *Phys.Rev.Lett.*, 82:892, 1999.

[43] Treder H.-J. Borzeszkowski H. H. Mach-einstein doctrine and general relativity. *Found. of Phys.*, 26, 1996. .

[44] J. Bowen and J. W. York. Time-asymmetric initial data for black holes and black-hole collisions. *Phys. Rev. D*, 21:2047–2056, 1980.

[45] J. M. Bowen. Inversion symmetric initial data for n chared black holes. *Ann. Phys.*, 165:17–37, 1985.

[46] S. Brandt and B. Brügmann. A simple construction of initial data for multiple black holes. *Phys. Rev. Lett.*, 78(19):3606–3609, 1997.

[47] D. Brill and R. Lindquist. Interaction energy in geometrostatics. *Phys. Rev.*, 131:471–476, 1963.

[48] B. Brügmann. Bifunctional adaptive mesh (bam) for 3d numerical relativity. In J. Frieman A. Olinto and D. Schramm, editors, *Proceedings of The 18th Texas Symposium on Relativistic Astrophysics*, Singapore, 1998. World Scientific.

[49] B. Brügmann. Binary black hole mergers in 3D numerical relativity. *Int. J. Mod. Phys. D*, 8:85, 1999.

[50] Bernd Brügmann, Wolfgang Tichy, and Nina Jansen. Numerical simulation of orbiting black holes. 2003. gr-qc/0312112.

[51] Alessandra Buonanno and Thibault Damour. Transition from inspiral to plunge in binary black hole coalescences. *Phys. Rev.*, D62:064015, 2000.

[52] K. Camarda. *A Numerical Study of 3D Black Hole Spacetimes*. PhD thesis, University of Illinois at Urbana-Champaign, Urbana, Illinois, 1998.

[53] D. Christodoulou. Reversible and irreversible transformations in black-hole physics. *Phys. Rev. Lett.*, 25(22):1596–1597, 1970.

[54] G. Cook. *Initial Data for the Two-Body Problem of General Relativity*. PhD thesis, University of North Carolina at Chapel Hill, Chapel Hill, North Carolina, 1990.

[55] G. Cook and J. W. York. Apparent horizons for boosted or spinning black holes. *Phys. Rev. D*, 41(4):1077–1085, 1990.

[56] G. B. Cook. Initial data for axisymmetric black-hole collisions. *Phys. Rev. D*, 44:2983–3000, 1991.

[57] G. B. Cook. Three-dimensional initial data for the collision of two black holes II: Quasi-circular orbits for equal-mass black holes. *Phys. Rev. D*, 50(8):5025–5032, 1994.

[58] G. B. Cook, M. W. Choptuik, M. R. Dubal, S. Klasky, R. A. Matzner, and S. R. Olivera. Three-dimensional initial data for the collision of two black holes. *Phys. Rev. D*, 47:1471, 1993.

[59] Gregory B. Cook. Initial data for numerical relativity. *Living Reviews in Relativity*, 2000:5, 2000.

[60] Gregory B. Cook. Corotating and irrotational binary black holes in quasi-circular orbits. *Phys. Rev.*, D65:084003, 2002.

[61] Sergio Dain, Carlos O. Lousto, and Ryoji Takahashi. New conformally flat initial data for spinning black holes. *Phys. Rev. D*, 65:104038, 2002.

[62] Thibault Damour, Piotr Jaranowski, and Gerhard Schäfer. Equivalence between the ADM-Hamiltonian and the harmonic- coordinates approaches to the third post-Newtonian dynamics of compact binaries. *Phys. Rev.*, D63:044021, 2001.

[63] S. Detweiler. Evolution of the constraint equations in general relativity. *Phys. Rev. D*, 35:1095, 1987.

[64] P. Diener. A new general purpose event horizon finder for 3D numerical spacetimes. *Class. Quantum Grav.*, 20(22):4901–4917, 2003. gr-qc/0305039.

[65] P. Diener, N. Jansen, A. Khokhlov, and I. Novikov. Adaptive mesh refinement approach to construction of initial data for black hole collisions. *Class. Quantum Grav.*, 17:435–451, 2000. gr-qc/9905079.

[66] D. Eardley and L. Smarr. Time functions in numerical relativity: Marginally bound dust collapse. *Phys. Rev. D*, 19:2239, 1979.

[67] Herrmann Frank. private communication.

[68] H. Friedrich. *Proc. Roy. Soc. London*, A 375:169–184, 1981.

[69] H. Friedrich. The asymptotic characteristic initial value problem for einstein's vacuum field equations as an initial valur problem for a first order quasi-linear symmetric hyperbolic system. *Proc. Roy. Soc. London*, A 378:401–421, 1981.

[70] H. Friedrich. On the hyperbolicity of Einstein's and other gauge field equations. *Comm. Math. Phys.*, 100:525–543, 1985.

[71] H. Friedrich. Hyperbolic reductions for Einstein's equations. *Class. Quantum Grav.*, 13:1451–1469, 1996.

[72] H. Friedrich and G. Nagy. The initial boundary value problem for Einstein's vacuum field equations. *Commun. Math. Phys.*, 201:619–655, 1999.

[73] S. Frittelli and O. Reula. Well-posed forms of the 3+1 conformally-decomposed Einstein equations. *J. Math. Phys.*, 40:5143–5156, 1999. gr-qc/9904048.

[74] Alcides Garat and Richard H. Price. Nonexistence of conformally flat slices of the Kerr spacetime. *Phys. Rev.*, D61:124011, 2000.

[75] A. M. Ghez, M. Morris, E. E. Becklin, Kremenek T., and Tanner A. *Nature*, 407:349, 2000.

[76] E. Gourgoulhon and P. Grandclment. `http://www.eu-network.org/Projects/InitialData.html`.

[77] Eric Gourgoulhon, Philippe Grandclement, and Silvano Bonazzola. Binary black holes in circular orbits. I. A global spacetime approach. *Phys. Rev. D*, 65:044020, 2002.

[78] Philippe Grandclement, Eric Gourgoulhon, and Silvano Bonazzola. Binary black holes in circular orbits. II. Numerical methods and first results. *Phys. Rev. D*, 65:044021, 2002.

[79] C. Gundlach. Pseudo-spectral apparent horizon finders: An efficient new algorithm. *Phys. Rev. D*, 57:863–875, 1998. gr-qc/9707050.

[80] S. W. Hawking and G. F. R. Ellis. *The Large Scale Structure of Spacetime*. Cambridge University Press, Cambridge, England, 1973.

[81] S. W. Hawking and J.B Hartle. Energy and angular momentum flow in a black hole. *Commun. Math. Phys.*, 27:283–290, 1972.

[82] A. J. Kemball and N. T. Bishop. The numerical determination of apparent horizons. *Class. Quantum Grav.*, 8:1361–1367, 1991.

[83] A. Komar. Covariant conservation laws in general relativity. *Phys. Rev.*, 113:934–936, 1959.

[84] J. Libson, J. Massó, E. Seidel, and W.-M. Suen. A 3D apparent horizon finder. In R. T. Jantzen, G. M. Keiser, and R. Ruffini, editors, *The Seventh Marcel Grossmann Meeting: On Recent Developments in Theoretical and Experimental General Relativity, Gravitation, and Relativistic Field Theories*, page 631. World Scientific, Singapore, 1996.

[85] A. Lichnerowicz. L'intégration des équations de la gravitation relativiste et la problème des n corps. *J. Math Pures et Appl.*, 23:37, 1944.

[86] Carlos O. Lousto and Richard H. Price. Headon collisions of black holes: The particle limit. *Phys. Rev.*, D55:2124–2138, 1997.

[87] Richard A. Matzner, Mijan Huq, Alonso Botero, Dae Il Choi, Ullar Kask, Juan Lara, Steven Liebling, David Neilsen, Premana Premadi, and Deirdre Shoemaker. Analysis of "gauge modes" in linearized relativity. *Class. Quantum Grav.*, 14:L21, 1997.

[88] Mark Miller. On the circular orbit approximation for initial data in numerical relativity. 2003. submitted.

[89] C. Misner. Wormhole initial conditions. *Phys. Rev. D*, 118(4):1110–1111, 1960.

[90] C. Misner and J. Wheeler. Classical physics as geometry. *Ann. Phys. (N.Y.)*, 2:525–603, 1957.

[91] C. W. Misner, K. S. Thorne, and J. A. Wheeler. *Gravitation*. W. H. Freeman, San Francisco, 1973.

[92] Takashi Nakamura, Ken-ichi Oohara, and Y. Kojima. General relativistic collapse to black holes and gravitational waves from black holes. *Progress of Theoretical Physics Supplement*, 90:1–218, 1987.

[93] L. Nerger. Investigations of 3D binary black hole systems. Master's thesis, Universität Bremen, 2000.

[94] N. O'Murchadha and J. York. Gravitational energy. *Phys. Rev. D*, 10(8):2345–2357, 1974.

[95] Eisenhart L. P. Riemannian geometry. *Princton University Press*, 1926.

[96] R. Penrose. Naked singularities. *Ann. N.Y. Acad. Sci.*, 224:125, 1973.

[97] Harald P. Pfeiffer, Gregory B. Cook, and Saul A. Teukolsky. Comparing initial-data sets for binary black holes. *Phys. Rev.*, D66:024047, 2002.

[98] Harald P. Pfeiffer and York J.W. Comparing initial-data sets for binary black holes. *Phys. Rev.*, D66:024047, 2002.

[99] Harald P. Pfeiffer, Saul A. Teukolsky, and Gregory B. Cook. Quasi-circular orbits for spinning binary black holes. *Phys. Rev.*, D62:104018, 2000.

[100] R. H. Price and J. Pullin. Colliding black holes: The close limit. *Phys. Rev. Lett.*, 72:3297–3300, 1994.

[101] B. Reimann. Maximal slicing of Schwarzschild. Master's thesis, Universität Potsdam, 2003.

[102] Erik Schnetter, Scott H. Hawley, and Ian Hawke. Evolutions in 3d numerical relativity using fixed mesh refinement. 2003. gr-qc/0310042.

[103] B. Schutz. Gravitational wave astronomy. *Class. Quantum Grav.*, 16:A131–A156, 1999.

[104] E. Seidel and W.-M. Suen. Towards a singularity-proof scheme in numerical relativity. *Phys. Rev. Lett.*, 69(13):1845–1848, 1992.

[105] M. Shibata and Takashi Nakamura. Evolution of three-dimensional gravitational waves: Harmonic slicing case. *Phys. Rev. D*, 52:5428, 1995.

[106] H. Shinkai and G. Yoneda. Adjusted ADM systems and their expected stability properties: constraint propagation analysis in Schwarzschild spacetime. *Class. Quantum Grav.*, 19:1027–1049, 2002.

[107] H. Shinkai and G. Yoneda. Re-formulating the Einstein equations for stable numerical simulations: Formulation Problem in Numerical Relativity. 2002. To be published in *Progress in Astronomy and Astrophysics* (Nova Science Publ., New York, 2003).

[108] L. Smarr. *The Structure of General Relativity with a Numerical Illustration: The Collision of Two Black Holes.* PhD thesis, University of Texas, Austin, Austin, Texas, 1975.

[109] L. Smarr. Spacetimes generated by computers: Black holes with gravitational radiation. *Ann. N. Y. Acad. Sci.*, 302:569–604, 1977.

[110] L. Smarr and J. York. Kinematical conditions in the construction of spacetime. *Phys. Rev. D*, 17:2529, 1978.

[111] TATJacobi: `http://www.tat.physik.uni-tuebingen.de/tat-arrangement`.

[112] Jonathan Thornburg. A fast apparent-horizon finder for 3-dimensional Cartesian grids in numerical relativity. *Classical and Quantum Gravity*, 21(2):743–766, January 21 2004.

[113] K. Thorne. whatever the best, most current reference is.

[114] Wolfgang Tichy and Bernd Brügmann. Quasi-equilibrium binary black hole sequences for puncture data derived from helical Killing vector conditions. 2003. gr-qc/0307027.

[115] Wolfgang Tichy, Bernd Brügmann, Manuela Campanelli, and Peter Diener. Binary black hole initial data for numerical general relativity based on post-Newtonian data. *Phys. Rev. D*, 67:064008, 2003. gr-qc/0207011.

[116] R. Voss and T. M. Tauris. Galactic distribution of merging neutron stars and black holes - prospects for short gamma-ray burst progenitors and LIGO/VIRGO. *MNRAS*, 342:1169–1184, July 2003.

[117] York J. W. *Phys. Rev. Lett.*, 26:1656, 1971.

[118] P. Walker. *Horizons, Hyperbolic Systems, and Inner Boundary Conditions in Numerical Relativity.* PhD thesis, University of Illinois at Urbana-Champaign, Urbana, Illinois, 1998.

[119] J. Wheeler. Geometrodynamics and the issue of the final state. In C. DeWitt and B. DeWitt, editors, *Relativity, Groups, and Topology (Les Houches, France, 1964)*, pages 316–520. Gordon and Breach, New York, 1964.

[120] J. A. Wheeler. *Phys. Rev. D*, 97:511, 1955.

[121] J. York. The initial value problem and dynamics. In Nathalie Deruelle and Tsvi Piran, editors, *Gravitational Radiation*, pages 175–201. North-Holland, Amsterdam, 1983.

[122] J. York. Initial data for collisions of black holes and other gravitational miscellany. In C. Evans, L. Finn, and D. Hobill, editors, *Frontiers in Numerical Relativity*, pages 89–109. Cambridge University Press, Cambridge, England, 1989.

[123] J. W. York. Conformally invariant orthogonal decomposition of symmetric tensors on riemannian manifolds and the initial value problem of general relativity. *J. Math. Phys.*, 14:456, 1973.

[124] J. W. York. Conformal 'thin-sandwich' data for the initial-value problem of general relativity. *Phys. Rev. Lett.*, 82:1350–1353, 1999.

[125] James W. York, Jr. Kinematics and dynamics of general relativity. In Larry L. Smarr, editor, *Sources of Gravitational Radiation*, pages 83–126. Cambridge University Press, Cambridge, UK, 1979.

[126] S. Portegies Zwart and S.L.W. McMillan. Black hole mergers in the universe. *ApJ. Lett.*, 528:L17, 2000.

[127] S. Portegies Zwart and S.L.W. McMillan. Gravitational thermodynamics and black-hole mergers. *Int. J. of Mod. Physics A.*, 15(30):4871, 2000.